NAVAL POSTGRADUATE SCHOOL

MONTEREY, CALIFORNIA

THESIS

OBSERVATIONS OF HYDRAULIC ROUGHNESS AND FORM DRAG IN THE WAKE OF A DEEP ICE KEEL IN THE ARCTIC OCEAN

by

Brandon K. Schmidt

March 2012

Thesis Advisor:	Timothy Stanton
Second Reader:	William Shaw

Approved for public release; distribution is unlimited

THIS PAGE INTENTIONALLY LEFT BLANK

REPORT DOCUMENTATION PAGE			Form Approved OMB No. 0704–0188
Public reporting burden for this collection of information is estimated to average 1 hour per response, including the time for reviewing instruction, searching existing data sources, gathering and maintaining the data needed, and completing and reviewing the collection of information. Send comments regarding this burden estimate or any other aspect of this collection of information, including suggestions for reducing this burden, to Washington headquarters Services, Directorate for Information Operations and Reports, 1215 Jefferson Davis Highway, Suite 1204, Arlington, VA 22202–4302, and to the Office of Management and Budget, Paperwork Reduction Project (0704–0188) Washington DC 20503.			
1. AGENCY USE ONLY *(Leave blank)*	**2. REPORT DATE** March 2012	**3. REPORT TYPE AND DATES COVERED** Master's Thesis	
4. TITLE AND SUBTITLE Observations of Hydraulic Roughness and Form Drag in the Wake of a Deep Ice Keel in the Arctic Ocean		**5. FUNDING NUMBERS** **N/A**	
6. AUTHOR(S) Brandon K. Schmidt			
7. PERFORMING ORGANIZATION NAME(S) AND ADDRESS(ES) Naval Postgraduate School Monterey, CA 93943–5000		**8. PERFORMING ORGANIZATION REPORT NUMBER** **N/A**	
9. SPONSORING /MONITORING AGENCY NAME(S) AND ADDRESS(ES) N/A		**10. SPONSORING/MONITORING AGENCY REPORT NUMBER** **N/A**	
11. SUPPLEMENTARY NOTES The views expressed in this thesis are those of the author and do not reflect the official policy or position of the Department of Defense or the U.S. Government. IRB Protocol number _____N/A_____.			
12a. DISTRIBUTION / AVAILABILITY STATEMENT Approved for public release; distribution is unlimited		**12b. DISTRIBUTION CODE** A	

13. ABSTRACT (maximum 200 words)

Decrease in Arctic Ocean perennial sea-ice has been observed in recent decades. As sea-ice continues to decline, marine traffic will increase and the United States will require a more active military presence in the Arctic. Future Arctic conditions must be forecasted with increased accuracy to allow for proper planning with regard to the nation's changing role in the region. It is the goal of this thesis to contribute to the knowledge of turbulence and mixing associated with ice keels in the Arctic Ocean in order to improve the accuracy of predictive coupled ocean/ice/atmospheric models.

At Applied Physics Laboratory Ice Station 2011, a 3-dimensional (3-D) sonar was used to record high resolution morphological measurements of an ice keel approximately 33 m long by 29 m across and 10 m deep. Sensors were deployed in the water column approximately 10 m from the keel to record water properties of salinity, temperature, and 3-D velocity at selected depths in the upper water column. These observations were used to make calculations of turbulence within the mixed layer, in order to gain a greater understanding of how keels affect turbulent drag and heat fluxes in the upper ocean.

Results indicate that keels generate significant turbulence and mixing in the upper ocean, even during benign weather conditions in which there is little surface forcing. Keels increase the kinetic energy of the upper ocean through production of turbulent eddies during times of weak stratification and the generation of internal waves during times of strong stratification. Keel-induced turbulence and mixing may lead to entrainment of warmer water underlying the surface mixed layer that could be a contributor to ice melting.

Calculation of the quadratic drag coefficient C_w also indicated that C_w varies greatly with water column stratification and ice undersurface roughness. Values as high as 0.08 were seen in the wake of a 10 m ice keel during strong stratification, and as low as 0.002 when the current was not affected by the keel during weak stratification. Most numerical models utilize a constant value of 0.0055 for $|C_w|$. Varying $|C_w|$ based on ice roughness and water column structure could greatly improve model accuracy.

14. SUBJECT TERMS Arctic Ocean, Beaufort Sea, Ice Concentration, Ice Morphology, Ice Roughness, Sea Ice, Ice Keel, Mixed Layer, Turbulence, Ocean Heat Flux, Mixing Length, Dissipation Rate, Drag Coefficient			**15. NUMBER OF PAGES** 101
			16. PRICE CODE
17. SECURITY CLASSIFICATION OF REPORT Unclassified	**18. SECURITY CLASSIFICATION OF THIS PAGE** Unclassified	**19. SECURITY CLASSIFICATION OF ABSTRACT** Unclassified	**20. LIMITATION OF ABSTRACT** UU

NSN 7540–01–280–5500 Standard Form 298 (Rev. 2–89)
Prescribed by ANSI Std. 239–18

THIS PAGE INTENTIONALLY LEFT BLANK

Approved for public release; distribution is unlimited

OBSERVATIONS OF HYDRAULIC ROUGHNESS AND FORM DRAG IN THE WAKE OF A DEEP ICE KEEL IN THE ARCTIC OCEAN

Brandon K. Schmidt
Lieutenant, United States Navy
B.S., University of Idaho, 2006

Submitted in partial fulfillment of the
requirements for the degree of

MASTER OF SCIENCE IN PHYSICAL OCEANOGRAPHY

from the

NAVAL POSTGRADUATE SCHOOL
March 2012

Author: Brandon K. Schmidt

Approved by: Timothy Stanton
Thesis Advisor

William Shaw
Second Reader

Jeffrey D. Paduan
Chair, Department of Oceanography

THIS PAGE INTENTIONALLY LEFT BLANK

ABSTRACT

Decrease in Arctic Ocean perennial sea-ice has been observed in recent decades. As sea-ice continues to decline, marine traffic will increase and the United States will require a more active military presence in the Arctic. Future Arctic conditions must be forecasted with increased accuracy to allow for proper planning with regard to the nation's changing role in the region. It is the goal of this thesis to contribute to the knowledge of turbulence and mixing associated with ice keels in the Arctic Ocean in order to improve the accuracy of predictive coupled ocean/ice/atmospheric models.

At Applied Physics Laboratory Ice Station 2011, a 3-dimensional (3-D) sonar was used to record high resolution morphological measurements of an ice keel approximately 33 m long by 29 m across and 10 m deep. Sensors were deployed in the water column approximately 10 m from the keel to record water properties of salinity, temperature, and 3-D velocity at selected depths in the upper water column. These observations were used to make calculations of turbulence within the mixed layer, in order to gain a greater understanding of how keels affect turbulent drag and heat fluxes in the upper ocean.

Results indicate that keels generate significant turbulence and mixing in the upper ocean, even during benign weather conditions in which there is little surface forcing. Keels increase the kinetic energy of the upper ocean through production of turbulent eddies during times of weak stratification and the generation of internal waves during times of strong stratification. Keel-induced turbulence and mixing may lead to entrainment of warmer water underlying the surface mixed layer that could be a contributor to ice melting.

Calculation of the quadratic drag coefficient C_w also indicated that C_w varies greatly with water column stratification and ice undersurface roughness. Values as high as 0.08 were seen in the wake of a 10 m ice keel during strong stratification, and as low as 0.002 when the current was not affected by the keel during weak stratification. Most numerical models utilize a constant value of 0.0055 for $|C_w|$. Varying $|C_w|$ based on ice roughness and water column structure could greatly improve model accuracy.

THIS PAGE INTENTIONALLY LEFT BLANK

TABLE OF CONTENTS

LIST OF FIGURES

LIST OF ACRONYMS AND ABBREVIATIONS

ACM	Acoustic Current Meter
ADCP	Acoustic Doppler Current Profiler
AIDJEX	Arctic Ice Dynamics Joint Experiment
APLIS	Applied Physics Laboratory Ice Station
CTD	Conductivity Temperature Depth
GPS	Global Positioning System
Hz	Hertz
IMU	Inertial Motion Unit
IOBL	Ice Ocean Boundary Layer
IPPC AR4	Intergovernmental Panel on Climate Change Fourth Assessment Report
LES	Large-Eddy Simulation
m	meters
NPS	Naval Postgraduate School
OA	Objective Analysis
PSU	Practical Salinity Unit
RMS	Root Mean Square
SHEBA	Surface Heat Budget of the Arctic Ocean
TKE	Turbulent Kinetic Energy
YD	Yearday
3-D	3-dimensional

THIS PAGE INTENTIONALLY LEFT BLANK

ACKNOWLEDGMENTS

I would like to gratefully acknowledge the U.S. Navy Arctic Submarine Laboratory and the University of Washington Applied Physics Laboratory for their support during APLIS 2011. Their assistance was instrumental in the successful completion of data collection while at the ice camp.

I also thank the Naval Postgraduate School's Department of Oceanography, particularly Professor Tim Stanton, for offering me the opportunity to participate in this exciting experiment, and his guidance in processing the data and then understanding what it was we had learned.

Most importantly, I must thank my wife, Jaime. Without her unwavering love, support, and encouragement this thesis would have never been possible.

THIS PAGE INTENTIONALLY LEFT BLANK

I. INTRODUCTION

A. MOTIVATION

1. Arctic Changes

The Arctic environment has changed significantly in recent decades and a decrease in perennial sea-ice area and thickness has been widely observed. As perennial sea ice continues to decline, access to the Arctic by commercial and civilian vessels will undoubtedly increase due to significantly shortened transit routes that reduce shipping costs. In addition, the accessibility of the abundant natural resources in the Arctic will continue to rise, which will lead to increased economic interests in the Arctic region. In order to provide security and to protect the nation's interest in this changing region, the United States will require a more active military presence in the Arctic in the coming years.

It is imperative that future Arctic conditions are forecasted with increased accuracy in order to allow for proper planning with regard to the nation's changing role in the region. Current predictive models provide conservative estimates of sea-ice concentrations. However, inaccuracies arise due to the lack of observations and understanding of the physical processes that promote changes in sea ice. Improvements must be made in these two areas to allow more accurate predictions of Arctic sea ice conditions.

2. Arctic Modeling

All models utilized in the Intergovernmental Panel on Climate Change Fourth Assessment Report (IPCC AR4) show a decrease in Arctic ice cover from the period 1953–2006. However, observations collected during the same period show an Arctic sea ice extent decline below the IPCC modeled September average sea ice extent (Stroeve et al. 2007). Comparing the observed Arctic sea ice extent to 13 IPCC AR4 models (see

Figure 1), Stroeve et al. (2007) observed that between 1953 and 2006 there was a –7.8 ± 0.6 %/decade decrease in sea ice extent. This is three times larger than the multi-model mean trend of –2.5 ± 0.2%/decade, suggesting that as a group, these models do not forecast sea ice extent accurately.

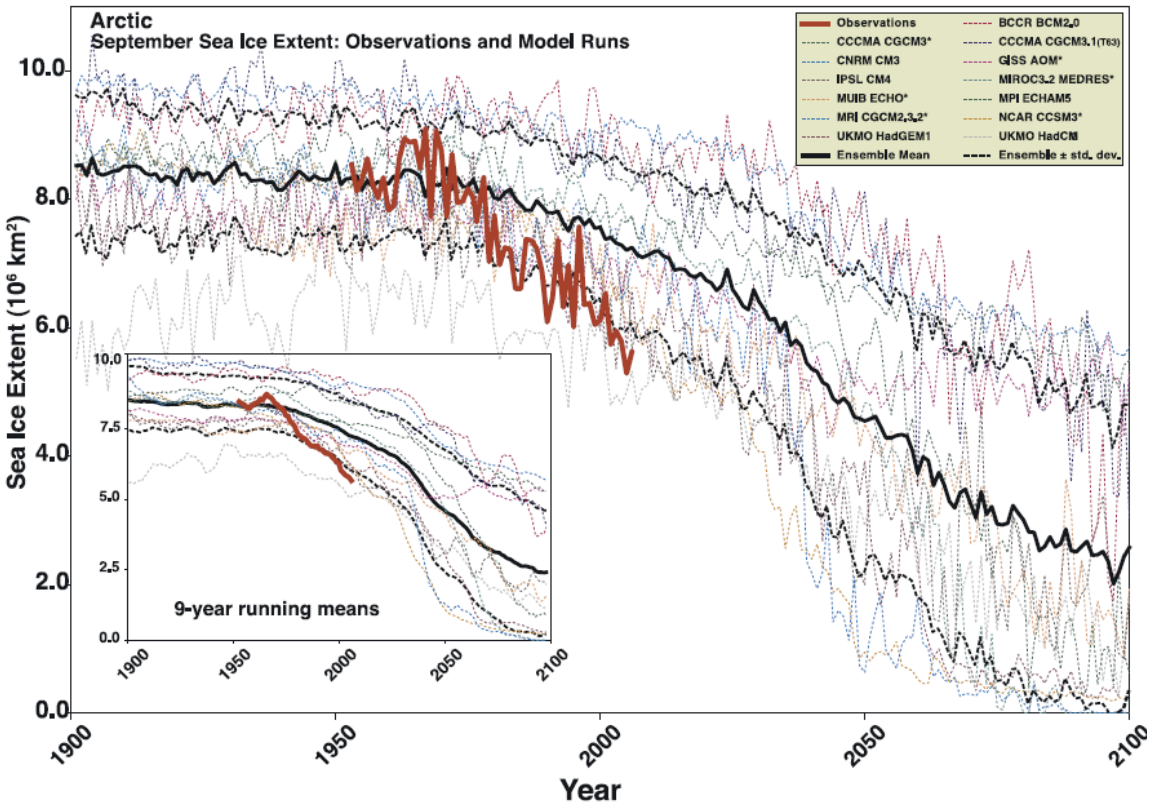

Figure 1. Arctic September sea ice extent (x 10^6 km^2) from observations (thick red line) and 13 IPCC AR4 climate models, together with the multi-model ensemble mean (solid black line) and standard deviation (dotted black lines). Models with more than one ensemble member are indicated with an asterisk. Inset shows nine year running means. (From Stroeve et al. 2007)

The Arctic's harsh and remote environment makes observations and in-situ measurements difficult to obtain. In large part existing information was recorded using satellite remote sensing. Therefore, observations and validations regarding the region, prior to the satellite age are sparse, which makes modeling the Arctic challenging. A

priority in attempting to model this sparsely sampled region is to understand the physical processes that occur in the atmosphere-ice-ocean system.

3. Physical Processes

Two physical processes that must be understood in order to accurately model the declining Arctic sea ice are the ocean-ice-albedo feedback and advection of heat below the Arctic Ocean mixed layer.

a. Albedo Feedback

Albedo is a surface's ability to reflect solar radiation. Snow covered sea ice has a high albedo thus reflects much of the incoming solar radiation, 80%–90%, while open water has a much lower albedo, only 10%, causing much of the incoming solar radiation to be absorbed into the ocean (Perovich et al. 2002). As ice extent decreases the ocean continues to become more exposed to incoming radiation thereby increasing the ocean's temperature. The increasing ocean temperature leads to a further decline in sea-ice which exposes more of the ocean to incoming radiation. This positive feedback loop, in which every iteration adds to the last, can have a dramatic effect on the state of the ice cover.

b. Heat Advection

A second potential heat source that affects sea ice extent, and the one of interest for this study, is vertical turbulent transport to the ice-ocean boundary layer (IOBL) from heat-carrying Atlantic or Pacific origin layers within the halocline (Shaw et al. 2009). Large scale advection of heat in the Arctic is dominated by the circulation of relatively warm, salty Atlantic Layer water. In some areas of the Arctic there is direct evidence that heat flux at the ocean-ice interface is supported by entrainment of heat transported from layers below the IOBL. For example, heat flux estimates obtained over the Yermak plateau show that large surface heat fluxes (22 W m^{-2}) were supported by entrainment of relatively warm Atlantic Layer water (McPhee et al. 2003).

Significant amounts of heat are also transported into the Arctic from the Pacific through the shallow Bering Straits. Pacific Water occupies the upper pycnocline of portions of the western Arctic, and it has been suggested that this heat source may play a role in the regional ice mass balance (Shimada et al. 2001; Steele et al. 2004). For example, Shimada et al. (2001) suggest that unusually warm Pacific origin water over the Northwind Ridge and Chukchi Plateau in the winter of 1997–1998 preconditioned the water column, which contributed to a large reduction in ice concentration in the that area the following summer.

B. STUDY OBJECTIVES

Hydrodynamic process associated with keels may be a mechanism that transports heat to the base of the ice, leading to increases in ice melt. This research uses high-resolution morphological measurements of an ice pressure ridge keel in the Arctic Ocean to study how such features affect turbulence and mixing in the upper ocean. Observations collected are aimed at providing a better insight into pressure ridge keels and their influence on the processes that occur in the Arctic Ocean mixed layer and to investigate whether these processes can be parameterized to improve predictive models.

Previous studies of ice bottom morphology, (Bourke and Mclaren 1992; Davis and Wadhams 1995) have been based on data obtained from upward-looking and side scan sonar systems, and have focused on statistical characterization of the basic geometrical features of ice ridge keels (draft, spacing, width, slope). To date, there have been no studies in which concurrent hydrodynamic and high-resolution morphological measurements have been used to relate measured drag with directly-observed, under-ice morphology.

Pressure ridge keels that frequently extend 15 m vertically from the ice bottom, and have been seen to extend as far as 47-meters (Davis and Wadhams 1995) may occupy a significant fraction of the IOBL. Using upward looking sonar system data from 12 submarine voyages, Bourke and McLaren (1992), calculated during the summer there are 1–3 keels with drafts greater than 9 m per kilometer, and during the winter the

frequency increases to 2–4 keels per kilometer. The frequency is even greater approaching the Alaskan and Canadian coasts where 6–10 keels per kilometer were seen. Near Greenland, Davis and Wadhams (1995) examined 749-keels using upward looking and side scan sonar data collected during a 1987 cruise of a British submarine and calculated that there are 4.26 keels with drafts greater than 5 m per kilometer. The relatively large size of the keels (compared to roughness elements in the atmospheric boundary layer and the ocean bottom boundary layer, for example) makes the ridge keel problem unique.

Turbulent processes in the vicinity of ridge keels, such as downstream wakes, may be a dominant source of drag and mixing in the IOBL. During the 1997–1998 Surface Heat Budget of the Arctic Ocean (SHEBA) experiment, McPhee (2004) observed that a pressure ridge keel approximately 110 m upstream from the data collection site had substantial impact on turbulence in the upper part of the boundary layer.

Using a large-eddy simulation (LES) model and turbulence measurements from the SHEBA experiment, Skyllingstad et.al (2003) examined the effects of ice keels on the upper ocean. Modeling two cases, one winter and one summer, found that during the winter a flow disruption by a 10 m deep keel causes enhanced vertical mixing and increased the heat flux from background values of approximately 5 W m^{-2}, to values averaging approximately 25 W m^{-2}. These elevated heat fluxes in the wake region are generated by increased entrainment of warmer water from beneath the mixed layer. The LES model also showed that the turbulent wake created by the keel extends hundreds of meters downstream from the keel. Simulations of the summer case showed that keels generate strong turbulence that is able to rapidly mix the fresh melt layer in the lee of a keel (Skyllingstad et al. 2003).

The goal of this research is to determine the role ice keels play in the mixing of the ocean mixed layer and entrainment from the pycnocline at the base of the mixed layer.

C. MEASURES OF TURBULENCE

In order to describe and parameterize the turbulence and mixing generated as the selected ice keel transited through the water, turbulent heat flux, mixing length, dissipation rates, and friction velocity are calculated.

1. Turbulent Heat Flux (Q)

Vertical motions, generated by ice motion relative to the ocean, actively generate upward and downward heat flux that extends through the upper ocean and is calculated using Equation (1).

$$Q = \rho_0 C_p \overline{w'T'} \qquad (1)$$

Where ρ and C_p are the density and specific heat of seawater, and w′ and T′ are turbulent fluctuations of the vertical velocity and temperature, over some finite averaging period.

The direct covariance method estimates heat flux by cross correlating simultaneous measurements of w′ and T′. The average correlation over this time period is then used as an estimate of the ensemble average covariance.

2. Power Spectra

Spectral analysis provides an important tool for studying the cascade of energy from large to small scales in turbulent flows (McPhee 2008). The wavenumber spectrum S(k), which represents turbulent kinetic energy as a function of the wavenumber, is calculated using MATLAB function pwelch, in which the power spectral density is estimated using Welch's method with a Hamming window and a 50% overlap of data segments. In this study, power spectra are typically presented as a function of the wavenumber. In order to calculate the spectra it is assumed that the relative current is moving past the sensors fast enough so that Taylor's frozen field hypothesis can be invoked. The recorded time series data is then transformed into a spacial series using the relation $k = 2\pi f/U$.

The theoretical inertial subrange (Equation 2) provides a model for the vertical velocity energy density spectra at k, where k = 2πf/U is the angular wave number calculated from frequency f and mean current speed U by Taylor's hypothesis, α_ε is the Kolmogorov constant, taken to be 0.51 (McPhee 1994), and ε is molecular scale dissipation. The 4/3 factor arises from theoretical considerations of homogeneous, isotropic turbulence where it is possible to relate the one-dimensional along-stream and cross-stream spectra to the total three-dimensional energy spectrum (Batchelor 1967).

$$Sww(k) = \frac{4}{3}\alpha_\varepsilon \varepsilon^{2/3} k^{-5/3} \qquad (2)$$

From the vertical velocity energy density spectra the dissipation rate ε and mixing length λ, described below, can be derived.

a. Dissipation Rate (ε)

Kinetic energy cascades down from large energy containing eddies to small eddies in a series of small steps. The small eddies then dissipate the turbulent kinetic energy (TKE) into heat. It is here where molecular viscosity plays a major role in natural turbulent flows and defines a smallest scale of turbulent motion. In order to calculate the dissipation rate Equation (2) is rearranged to give an Equation (3).

$$\varepsilon^{2/3} = \frac{3}{4\alpha_\varepsilon} Sww(k) k^{5/3} \qquad (3)$$

By simplifying the TKE equation to its simplest form of TKE production from shear equals TKE dissipation, an approximate balance not uncommon in natural flows (McPhee 2008), an estimate for turbulence production due to shear can be attained from the dissipation rates.

b. Mixing Length (λ)

Mixing length λ (Equation 4) is the scale of the energy-containing eddies.

$$\lambda = {c_\lambda}/{k_{\max}} \qquad (4)$$

Where c_λ is a proportionality constant = 0.85, and k_{max} is the peak wave number in the vertical velocity power spectrum.

3. Friction Velocity (u*)

Friction velocity u* characterizes the stress at the boundary, and can be measured by direct covariance (Equation 5).

$$u_* = \sqrt[4]{(\overline{u'w'}^2 + \overline{v'w'}^2)} = \sqrt{\frac{\tau_0}{\rho}} \qquad (5)$$

Friction velocity is related to the magnitude of the Reynolds stresses τ_0 by the relation shown in Equation (5).

II. DATA COLLECTION AND DATA PROCESSING

A. DATA COLLECTION

1. Experiment Site Layout

The ICEX2011 experiment was conducted at Applied Physics Laboratory Ice Station (APLIS) 2011, in the Beaufort Sea, from March 17–23, 2011. During the experiment, APLIS ice camp traveled approximately 10 kilometers (km), from 072.54° N, 146.39° W to 073.00° N, 146.42° W in response to low to moderate intensity wind events.

An 18-inch diameter hydrohole was melted through the 1.5 meter (m) thick ice floe, adjacent to an undersurface ice ridge feature identified during an ice thickness survey. An 8 x 8 x 8 foot instrument shed was then placed over the hydrohole. The instrument shed was insulated and contained a kerosene heater that maintained the temperature within the shed at approximately 25 ^{o}C.

Great care was used in selecting a site to deploy the turbulence mast. Historical wind and ice movement data were considered, in an attempt to place the mast in such a location as to maximize the time the ocean-deployed instruments would be in the wake of the pressure ridge keel for wind events typical of the area in the springtime.

Sensors deployed from the instrument shed were a global positioning system (GPS) logger, two turbulence flux packages developed by Research Professor Tim Stanton and his turbulence research group at Naval Postgraduate School (NPS), an RD Instruments 1.2 MHz Workhorse Monitor Acoustic Doppler Current Profiler (ADCP), and a BlueView BV5000 MB 1350–45 3D microbathymetry underwater imaging sonar. Approximately twice every day, conductivity, temperature, depth (CTD) profiles were measured up to 500 m using a Sea-Bird Electronics, SBE 19 CTD. Wind speed, wind direction, air temperature, and barometric pressure observations were electronically recorded every five minutes from a 10 m high mast deployed by the ice station staff, and shared with the group.

The layout of the ocean boundary layer experiment is shown in the plan view schematic in Figure 2. A local coordinate system was selected such that the +v current velocity component was aligned with a line starting at the turbulence mast extending through the center of the ice feature and the +u velocity component was 90-degrees clockwise of +v extending from the turbulence mast. All turbulence sensor observations were recorded in relation to the individual sensors coordinate system. Orientation of instrument readings to the local coordinate system is described in Section II.B.2.*b* below.

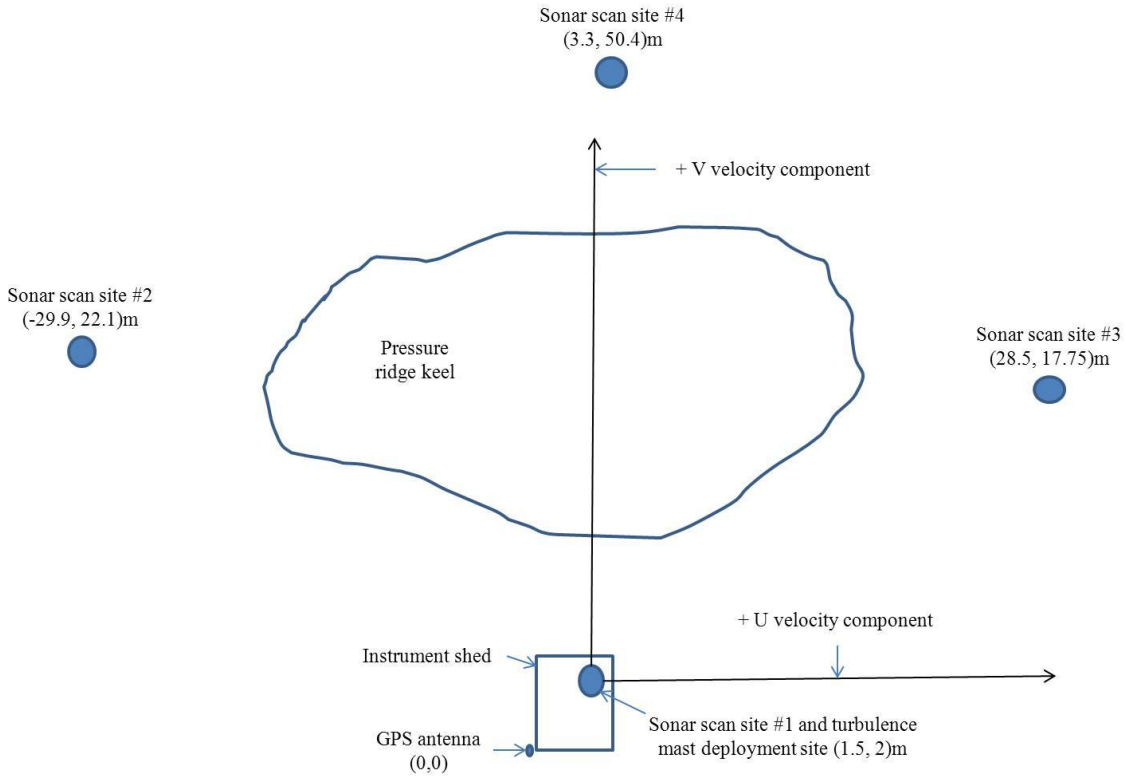

Figure 2. Sensor deployment sites for experiment during ICEX 2011. CTD and weather data was collected at APLIS command hut, which is not pictured in figure. Image not to scale, for reference only.

2. Turbulence Mast

The turbulence mast (Figure 3) was deployed from the instrument shed at (1.5, 2) meters in the pressure ridge coordinate system, a position approximately 15 m from the center of the ice keel. The mast supported two flux packages, one at the top of the mast and one at the bottom, separated by a 6 m torsionally rigid stainless steel tube assembly. Both flux packages were mounted on the upstream side of the mast which was steered into the current by a 1 m long by 0.5 m deep plastic vane attached to the down-stream side of the mast (Figure 3). The ADCP was mounted one meter below the top flux package, five meters above the bottom flux package, and was directed down into the water column. Between the ADCP and the bottom flux package were the stabilization vane and an electronic infrastructure assembly. The electronic infrastructure assembly provided power to, and received serial data from the two flux packages and the ADCP, then output the data streams via an underwater Ethernet cable to the data recording computer at the surface in the instrument shed. The ADCP, stabilization vane, and electronic infrastructure assembly were all mounted on downstream side of mast. An electric winch was mounted within the instrument shed to raise and lower mast in the water column.

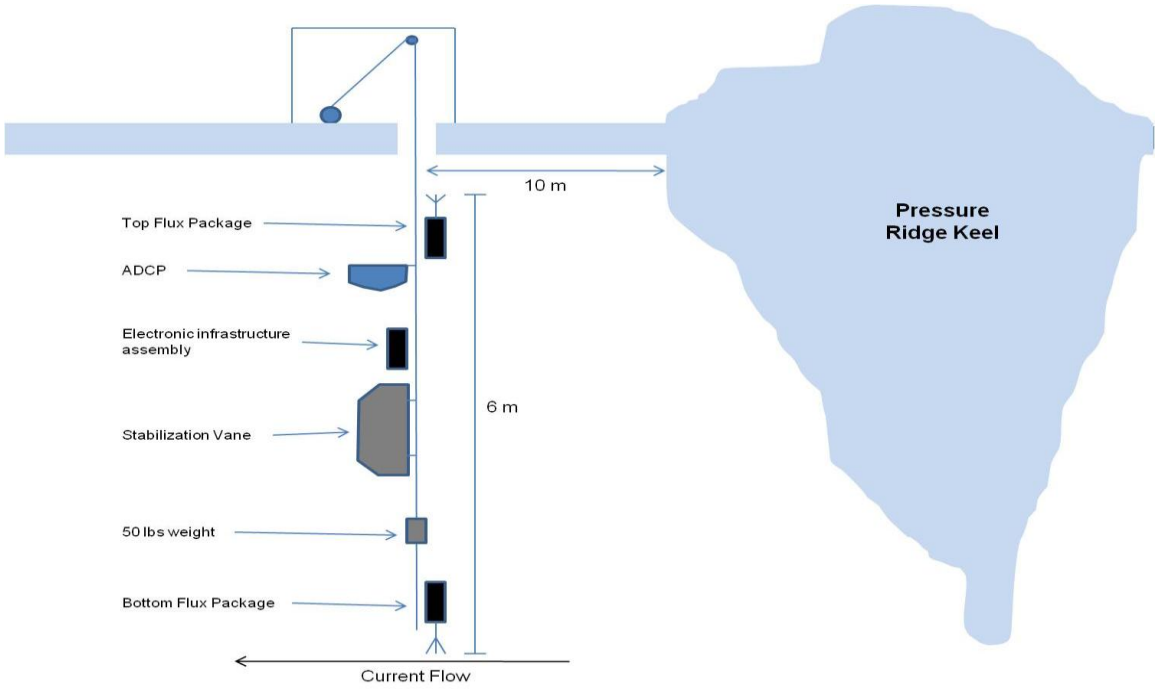

Figure 3. Schematic of turbulence mast set-up. Image not to scale, for reference only.

a. Turbulence Flux Packages

The turbulence flux packages sample high resolution time series measurements of ocean temperature, conductivity (and derived salinity and density), and three component velocity vector at sampling scales of 0.1 m cube. Designed and built at NPS, they were developed to measure turbulent fluxes of momentum, heat, and salt in the upper ocean. They collect temperature data accurate to 10^{-3} °C, conductivity accurate to 10^{-3} mS/cm, and path velocities between four sensors on an acoustic current meter (ACM) that are used to calculate u, v, and w water velocities accurate to 6 mm/s. Flux packages also contain a nano-mems inertial motion unit (IMU) so that heading and motion-corrected roll, pitch and yaw data of flux packages could be collected and used to correct for movement and tilt of the flux package, allowing earth-referenced u ,v and w velocity readings to be derived. All these data streams collected by flux packages are sampled at a rate of four Hertz (Hz).

b. ADCP

The ADCP was utilized to measure the water columns current structure across and beyond the turbulence mast frame. It was setup to collect data at 30, 0.5 m intervals in the water column, resulting in a maximum range of 15 m below the ADCP, with a sample rate of four samples per minute. ADCP also contained a magnetic compass in order to record the sensors heading.

The depth of the turbulence mast was determined from a pressure reading collected by the ADCP. The pressure was reported in decibars, which corresponds very closely to depth in meters for seawater.

c. Placement in the Water Column

Three depths were selected for placement of the instrumented mast in the water column. The first depth placed the top flux package 2 m below the bottom of the ice, with the lower flux package at 8 m below the ice. The second mast depth was chosen such that the top flux package was placed at the same depth as the deepest part of the ice keel, and the third depth was such that the top and bottom flux packages straddled the base of the mixed layer.

When moving the turbulence mast to the third depth, the base of the mixed layer was determined by carefully monitoring the water properties, conductivity and temperature, as reported by the bottom flux package. When a notable change in conductivity and temperature was seen, this indicated that the bottom flux package was moving out of the mixed layer. The mast was then lowered an additional three meters in order to straddle the two flux packages across the base of the mixed layer, with the top flux package remaining in the mixed layer and the bottom flux package in the pycnocline. Through this method it was determined that the base of the mixed layer was between 20 to 25 meters deep for the first four days of data collection. The last day the base of the mixed layer could not be determined since the pyconcline became diffuse and mixed layer depth poorly defined as seen in the last four CTD density profiles in Figure 29.

The turbulence mast was sequenced between these three sample depths for the duration of the experiment. Figure (4) displays the time series of turbulence mast placement depth. Each continuous time series of data at a given depth was partitioned into 40–60 minute intervals as described in Section II.B.2 below.

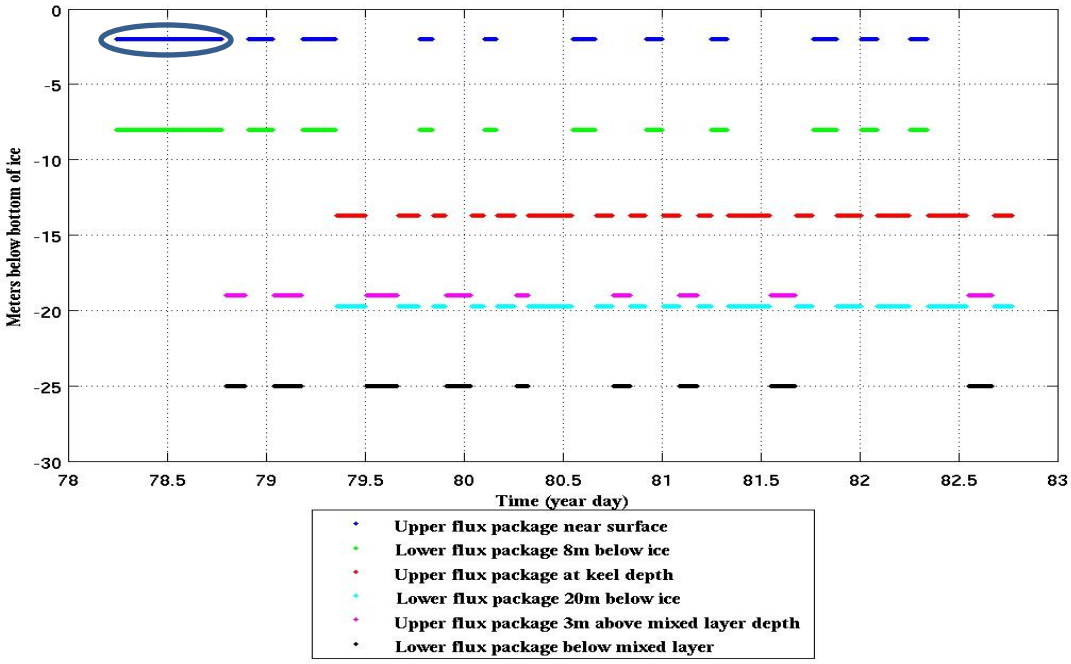

Figure 4. Approximate placement of flux packages in water column. Circled is a continuous data time series at a particular sample depth.

3. Sonar

Under ice morphology was measured using a BlueView BV5000 MB 1350–45 3D microbathymetry underwater imaging sonar that was deployed 3 m under the ice at four sites around the pressure ridge keel, as shown in Figure 2. This sonar uses a 16-element acoustic array to synthesize 256 vertical sonar beams to measure vertical slices of backscatter with a 1 degree beam-width. The sonar has a maximum range of 27 m and a vertical field of view of 45-degrees (BlueView 2010). The sonar was rotated in azimuth to radially map under ice morphology in a 27 m radius at each site. At each azimuth the backscatter returns had a threshold applied to detect the dominant scatter for each of the

256-beams (Figure 5). Azimuth angles were incremented by one degree then another vertical slice was captured resulting in 360-scans per deployment site. Four sites were occupied (Figure 2) resulting in 1440 total scans. These 1440-scans were then combined in order to create a 3-dimensional (3D) image of the keel using methods described in Section B.3 below.

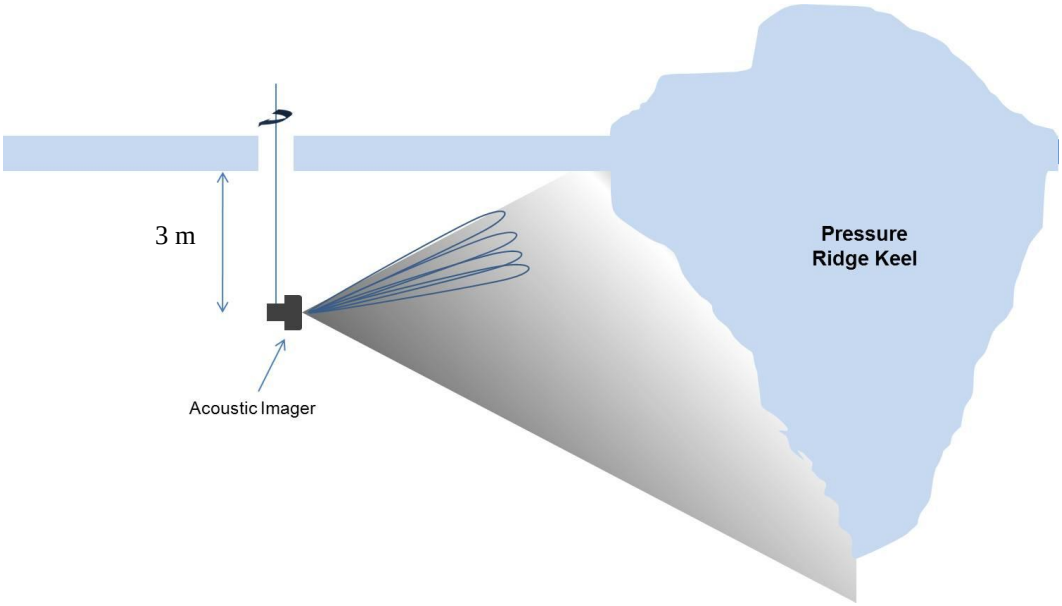

Figure 5. A schematic of 1 of 360 individual SONAR scans of the keel with four of the 256 synthesized vertical beams.

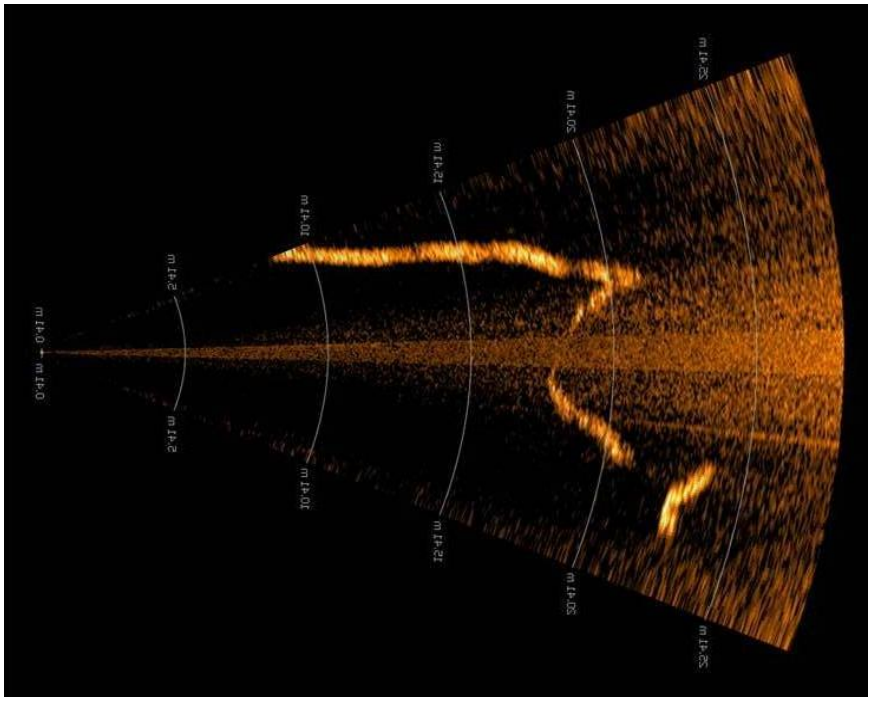

Figure 6. Image of sonar data at a single azimuth setting from left side of pressure ridge keel. Each Scan consists of an ensemble of approximately 3 seconds of 13 samples per second resulting in a 39-ping average. Each highlighted pixel represents the ice acoustic return which is output as a range and vertical angle for each synthesized beam.

4. GPS

Two sets of GPS data were collected during this experiment. The first data set was recorded at the corner of the NPS instrument shed, and it defined the local coordinate origin (0,0) in the ice floe drift reference frame for the experiment (as displayed on Figure 2). This data was continuously recorded at a rate of one Hz. The second data set was recorded by the ice camp staff at the camp command hut located approximately 30 m away, and was recorded at a rate of one sample every five minutes.

5. CTDs

A Sea-Bird, SBE 19 was used to make CTD profile observations at the site. One to three high resolution observations were recorded each day. In total, 17-profiles were collected during the course of the experiment. Most casts were to at least 200 m depth

and some to 500 m. The CTD observations were made in the APLIS command hut, positioned approximately 30 m southeast of the main hydrohole in which the turbulence mast was deployed.

6. Weather

Weather data was collected by the ice camp staff from the command hut. Readings of wind speed, wind direction, barometric pressure, and temperature were recorded every five minutes using sensors mounted 10 m above the ice.

B. DATA PROCESSING

1. GPS

The GPS data was used to determine the movement of the ice floe and to calculate the speed and direction of travel of the ice floe. Vector differencing of the two position time series measured at the instrument shed and command hut, allowed the ice floe rotation time series to be estimated.

Processing the GPS data required converting the latitudinal and longitudinal measurements to a local polar stereographic projection. The polar stereographic projection is based on the Hughes Ellipsoid and is true at 75^{o} N latitude. The coordinate system based on this projection has the origin at the pole, the +X axis along 90^{o} E longitude, +Y axis along 180^{o} longitude, and is measured in meters. Both GPS data time series had a mean longitudinal coordinate of 146.4^{o} W, therefore the data was rotated 146.4^{o} counterclockwise about the North Pole in order to position true north at 90^{o} in the local coordinate system.

Instrument shed GPS coordinates were then passed through a 2nd order lowpass filter with a 2.78 X 10^{-4} cutoff frequency, and differentiated in order to calculate the u and v component velocities and ice speed. Once u and v velocity components were calculated the ice floe movement direction could be calculated using the four-quadrant inverse tangent function, atan2 (Equation 6).

$$\text{atan2}(v,u)=\begin{cases}\tan^{-1}\left(\dfrac{v}{u}\right) & u>0\\ \tan^{-1}\left(\dfrac{v}{u}\right)+\pi & v\geq 0, u<0\\ \tan^{-1}\left(\dfrac{v}{u}\right)-\pi & v<0, u<0\\ +\dfrac{\pi}{2} & v>0, u=0\\ -\dfrac{\pi}{2} & v<0, u=0\\ undefined & v=0, u=0\end{cases} \quad (6)$$

Ice floe rotation was calculated by first computing five minute averages of the instrument shed GPS data, with the mean time for a particular five minute interval corresponding to a sample time of the command hut GPS data. Then vector differencing the two sets of converted polar stereographic GPS data after low pass filtering was done by substituting Equation 7 and 8 into Equation 6, with substituting y for v, and x for u.

$$y = \textit{instrument shed } y - \textit{command hut } y \quad (7)$$

$$x = \textit{instrument shed } x - \textit{command hut } x \quad (8)$$

Once the rotation time series was calculated it was then applied to the u and v component velocities from the ADCP and the two flux packages to align the sensors with the local coordinate system (Figure 2) as described in Section II.B.2.*b* below.

2. Turbulence Mast

Data collected by the turbulence mast sensors were partitioned into 40–60 minute time intervals for analysis of mean and turbulent properties. The length of time in yearday (YD) for a given continuous data time series (Figure 4), was divided by 0.0278, the fraction of YD equal to 40-minutes. The resulting number was rounded down to the nearest integer, which equaled the total number of intervals the continuous time series was to be broken into. The continuous time series was then divided equally into the

calculated number of intervals. The resulting 40–60 minute intervals are used in the subsequent processing, assuming that the current speed and direction were approximately steady so that the boundary layer properties were constant.

a. Heading

Due to weak magnetic disturbances associated with the turbulence mast sensors and structure, and the steep declination angle of the magnetic field at the site, error was introduced into the sensors heading readings. In order to reduce the effects of these heading errors, an *in situ* heading calibration was conducted.

Once the mast was deployed it was rotated in 20-degree increments, and the heading reading, along with the mast's actual heading were recorded. In comparing each sensor's recorded heading, to the actual heading, a fifth degree polynomial fit was calculated for each sensor (Figure 7). The polynomial calibration curve for each sensor was applied to all heading readings to calculate the corrected headings.

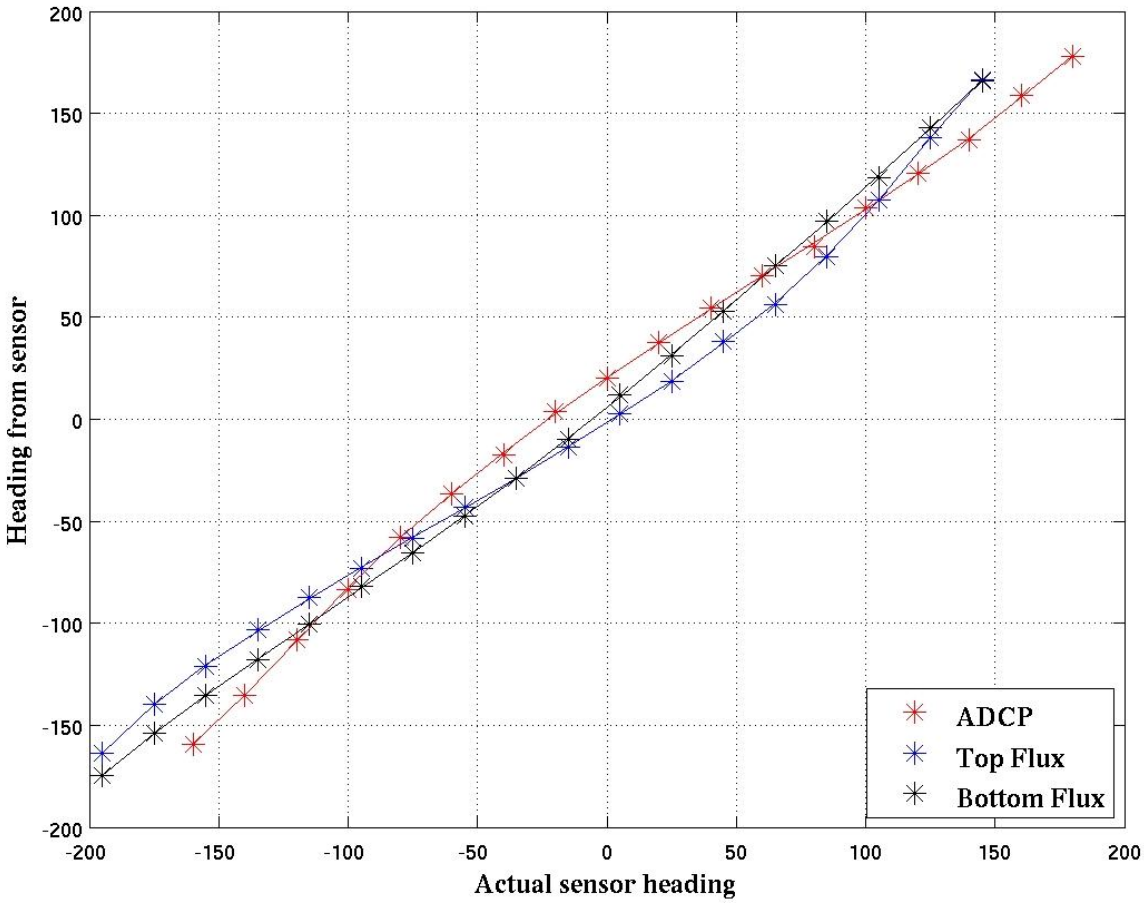

Figure 7. Sensor heading calibration curves. Stars indicates recorded heading from sensor for a given known heading. Solid lines indicate fifth degree polynomial calibration curve for sensor.

The corrected instrument headings were then used to orientate the component velocity readings from each sensor, recorded in the sensors coordinate system, to the local coordinate system (Figure 2), as described in Section II.B.2.*b* below.

b. Orientation to Local Coordinate System

Velocity data from each sensor was recorded in reference to each sensors instrument coordinate system. Orientation of the instrument readings to the local coordinate system (Figure 2) required several steps. First the corrected instrument heading, described in Section II.B.2.*a* above, was used to rotate the u and v component

velocities to the Earth's magnetic coordinates such that +v was aligned with magnetic north and +u positioned 90^{o} clockwise of magnetic north. During the local coordinate system designation +v aligned with 335^{o} magnetic, therefore each sensor's u and v component velocities were rotated counterclockwise 25^{o} to this coordinate system. Finally, the calculated ice floe rotation, described in Section II.B.1 above, was applied to the component velocities. This final rotation was done in order to account for the time variation of the ice floe rotation relative to the initial coordinate system designation.

c. ADCP

In order to measure current velocity profiles an ADCP transmits sound pulses along four narrow beams into the water column. This transmitted sound scatters off particles within the water column, and along beam velocity of these scatterers relative to the ADCP results in Doppler shifts of the returning sound energy to each ADCP transducer. From this Doppler shift current velocities are calculated. Unfortunately lack of acoustic scatterers in the very clear polar mixed layer resulted in low signal to noise ratios, which severely limited the range of ADCPs. The low backscatter levels resulted in useful ranges of only 3–5 m, severely limiting the ADCP's usefulness.

Confirmation that the ADCP's range was limited was done by examining the ADCP's echo intensity, which measures the received signal strength (Figure 8). When the echo intensity becomes a constant value for several bins, the "flattening out" of the backscatter profile indicates that the ADCP noise floor has been reached. It is at this point that the signal-to-noise ratio is very low and the ADCP cannot pick out the Doppler shifted signal (RD Instruments 1998). In the sample data shown in Figure 8, the echo intensity can be seen reaching a constant value at bin 12 for beam 2, while beams 1, 3, and 4 reach a constant value at bin 14.

The ADCP beam correlation values, a measure of data quality, were used to find the last good bin of data (RD Instruments 1998). By examining the ADCP current velocity data and echo intensity it was determined that ADCP data became invalid after

the beam correlation dropped below 50. As seem in Figure 8, for all four beams the correlation drops below this threshold at bin 10, 5 m below ADCP, for this sample.

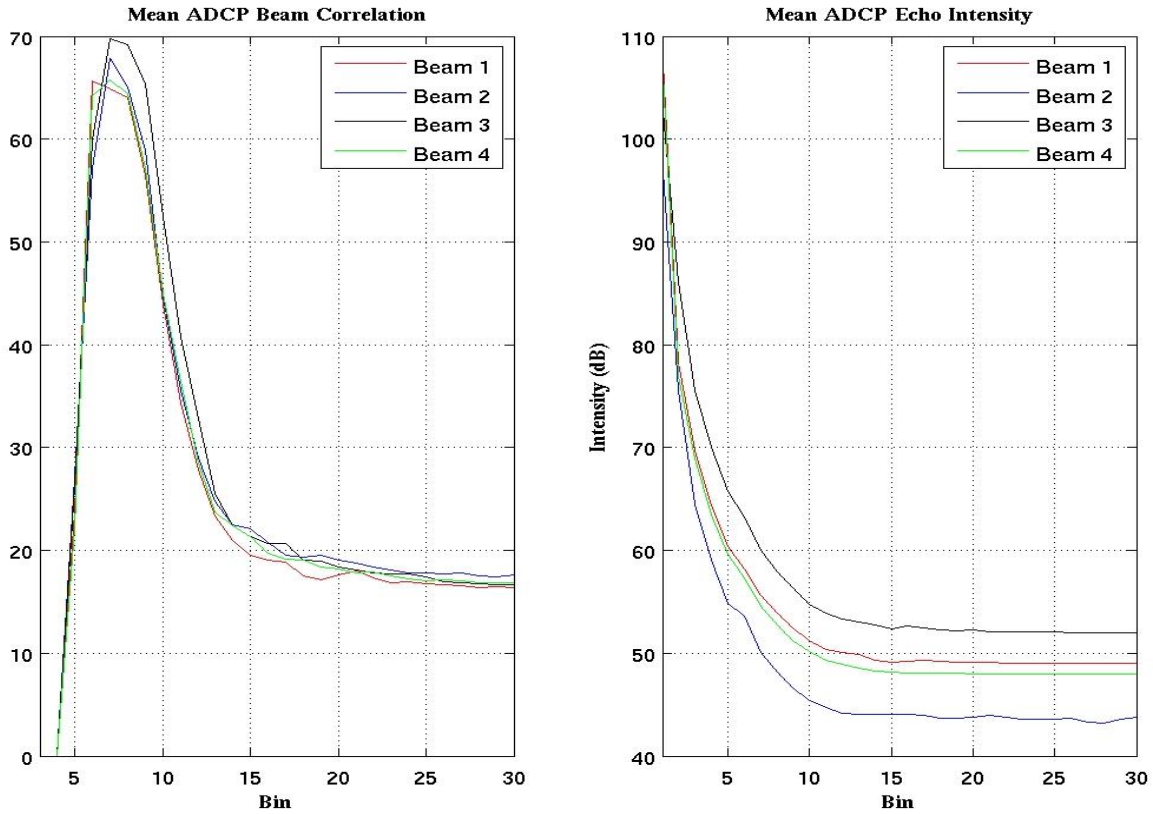

Figure 8. Mean ADCP beam correlation and echo intensity plots from data taken at YD 79.79 at the level of sampling closest to the ice undersurface. On correlation plot a value of 256 would indicate perfect correlation.

d. Turbulence Flux Packages

Each flux package ACM has arbitrary offsets on each of its four velocity sensor paths. ADCP measurements do not contain any zero bias offsets, therefore they can be utilized in determining the flux package zero offsets. In order to correct for these offsets, the mean of the ADCP data collected in bins six, seven, and eight was utilized in

determining a time of very low current (< 0.005 m/s). Using the ACM data recorded during that time, ACM path offsets were calculated and applied to the current velocity calculations.

Movement and tilts of the flux packages were determined from the IMU sensors in each instrument, and subtracted from the current u and v component velocities. This step eliminates the velocities sensed by the ACM that were actually caused by the sensor package movement within the water, rather than the water flow relative to the ice. There was virtually zero vertical flux package movement; therefore it was unnecessary to make this correction in the w velocity component.

Now that temperature, current velocities, and salinity, calculated using temperature, conductivity and depth (estimated to be pressure in decibars), have been determined, calculations regarding turbulence in the water column were made. These calculations include turbulent vertical heat flux Q (Equation 1), TKE dissipation rate ε (Equation 3), mixing length λ (Equation 4), and friction velocity u* (Equation 5) form Section I.C above.

3. Sonar

Sonar data collected was processed using ProScan 3.3 software. This software, developed by BlueView Technologies, Inc., converted the ranges for each synthesized beam (Figure 5) into XYZ points in 3D space. In order to accurately convert the raw data into XYZ coordinates, sound speed for the water must be accurately known. The sound speed was calculated from the CTD casts conducted on the same day the sonar scans were conducted with a mean mixed layer sound speed of approximately 1432 m s^{-1} within the fairly uniform ocean mixed layer (Figure 9).

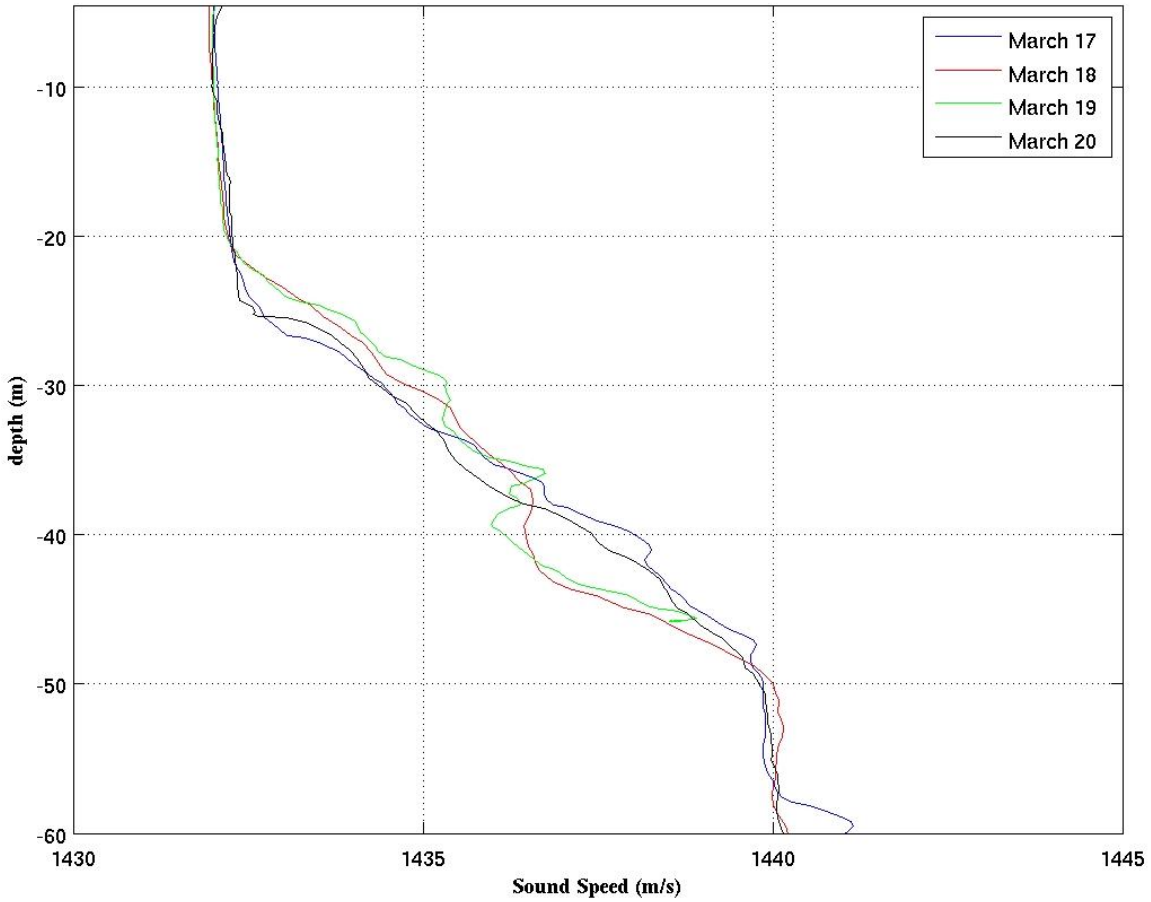

Figure 9. Sound speed profiles collected from CTD casts.

ProScan processing has a backscatter threshold level that controls the value at which a target will be detected (BlueView 2010). Each sonar beam return is assigned a range and backscatter intensity. Experimentation with the backscatter threshold value resulted in a choice of 125 in order to minimize side-lobe scattering noise in the processed data. XYZ processed data was compared in Figure 10 using amplitude thresholds of 100, the lowest possible setting, threshold of 125, and a threshold of 150. The elimination of near-surface clutter on the top half of the image can be seen in Figure 10, when using the range threshold of 125. Also shown is a decrease in actual returns when the threshold is increased to 150, which outweighs the benefit of increased scatter noise reduction. For these reasons a threshold of 125 was selected for data processing.

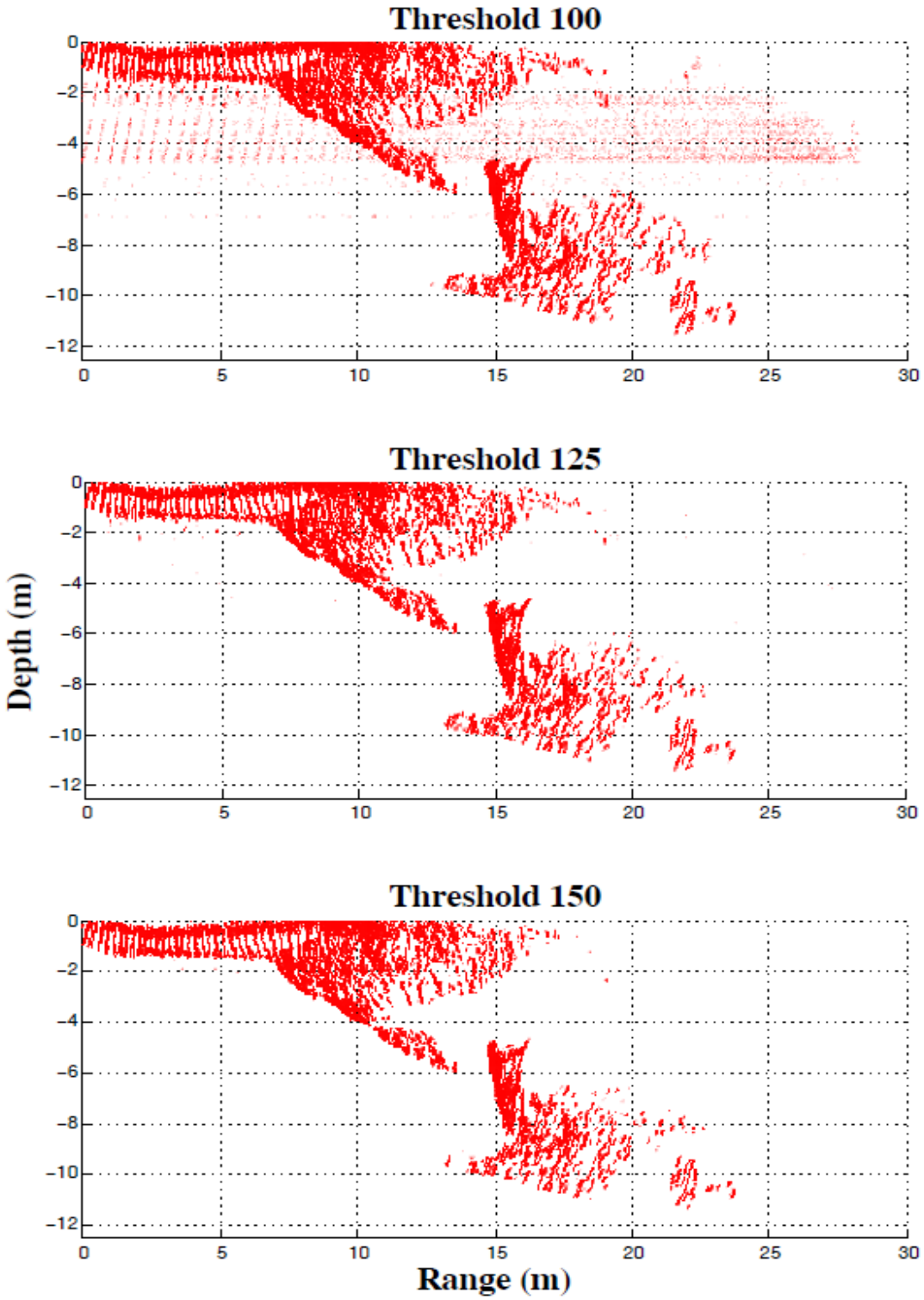

Figure 10. Plot of a 90-degree section of sonar data collected from scan site 4 (see Figure 2).

After processing all 1440 individual sonar scans and applying the appropriate XYZ offsets for each deployment site, the data cloud from each scan site were concatenated together with all scans positioned in reference to the grid origin, (0,0), (the back left corner of the instrument shed).

Due to the poor reflective properties of the smooth old ice, the sonar was only able to resolve returns up to approximately 20 m. The 15 m diameter holes around each sonar deployment site, seen in Figure 11, arise from the sonar being deployed 3 m below the ice and the 22.5 degree angle from horizontal of the top most beam. The first return will be at 3/sin (22.5), resulting in a blank range out to this radius.

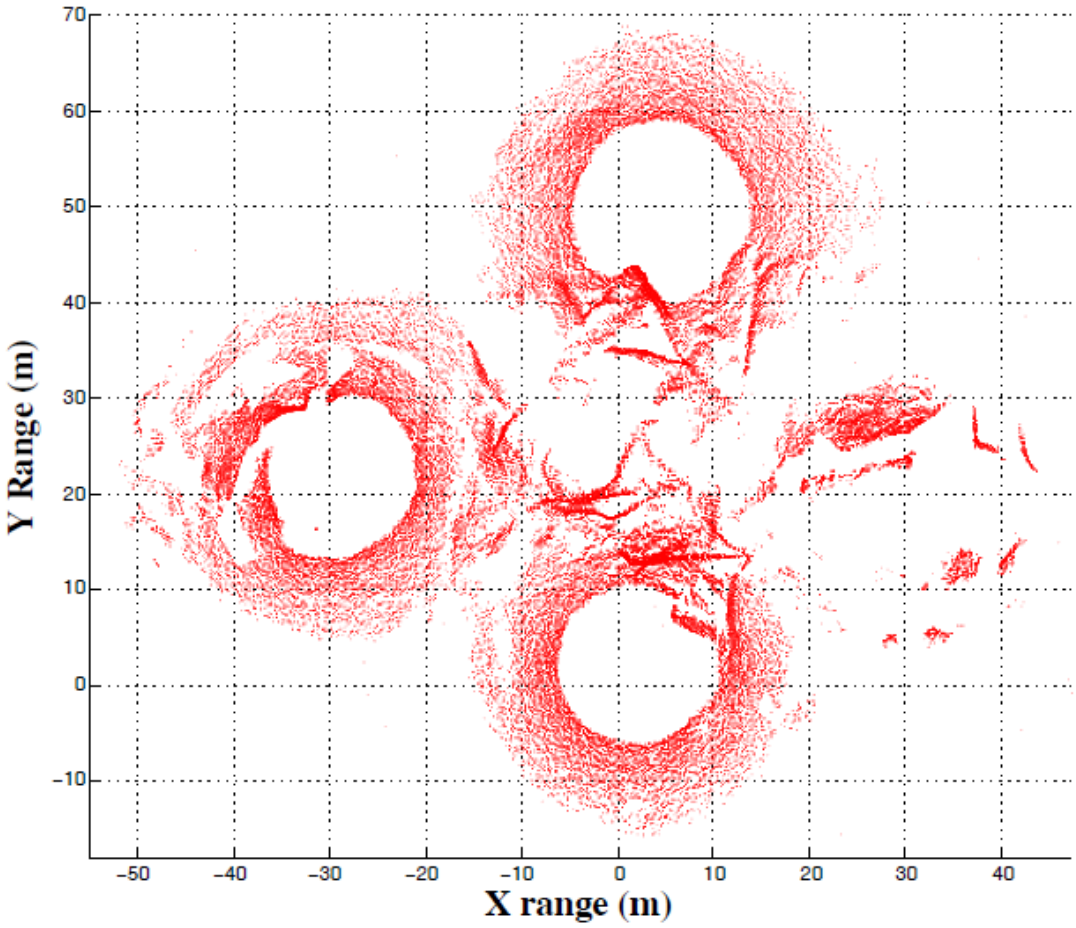

Figure 11. Overhead isotropic plan view of the sonar data point sampling pattern.

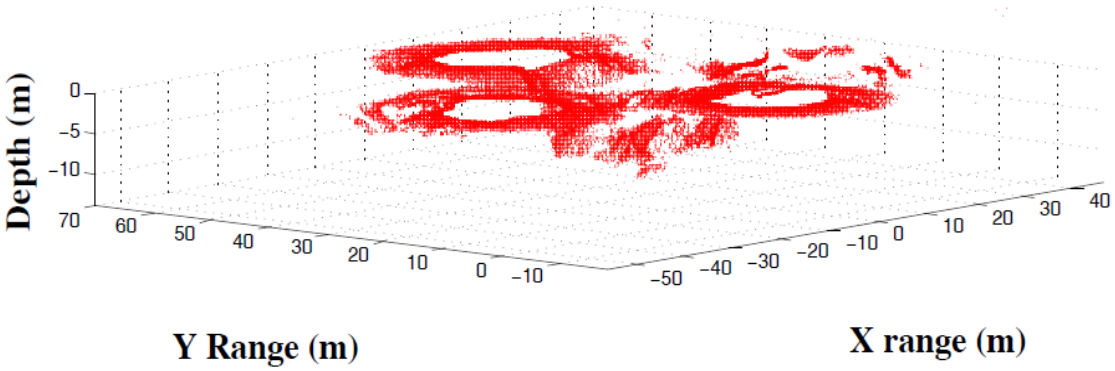

Figure 12. Top left isotropic view of sonar 3D point plot.

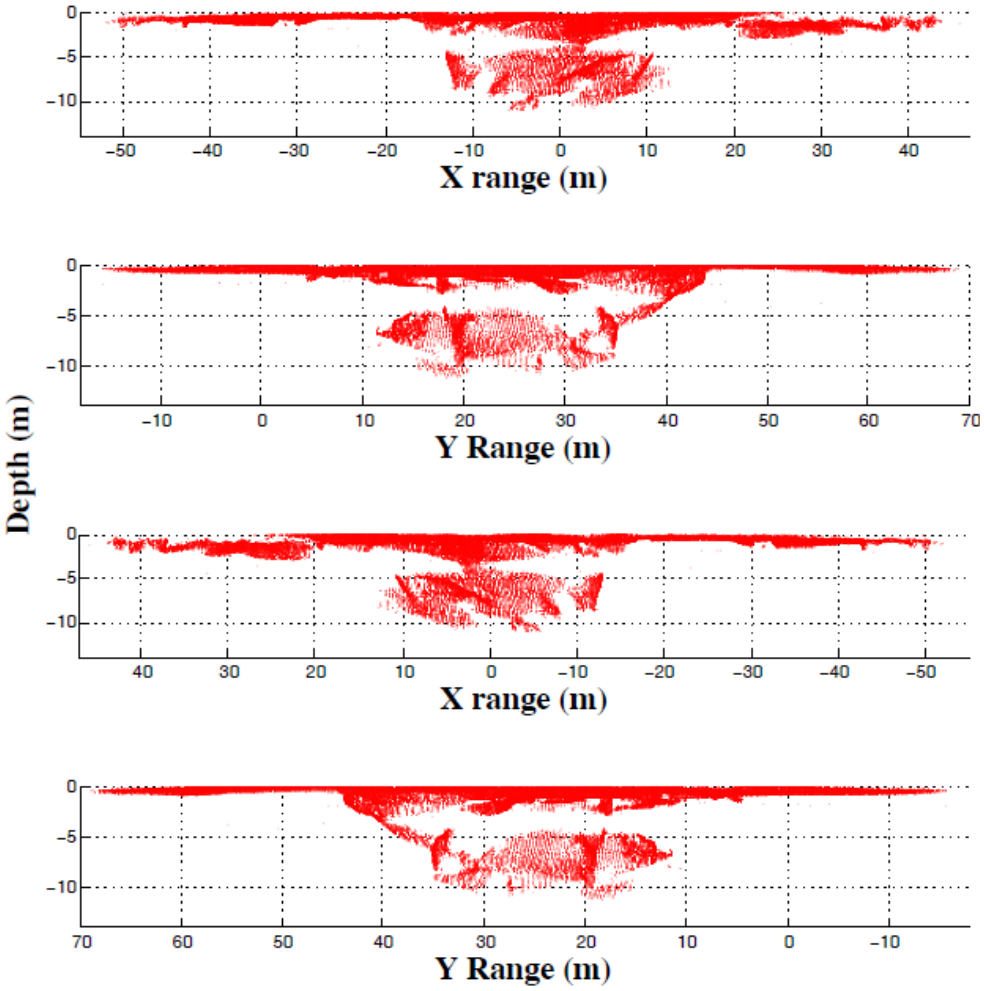

Figure 13. Side isotropic views of sonar 3D point plot. From top to bottom. View from downstream of keel, right of keel, upstream of keel, left of keel.

The XYZ sonar data was then consolidated using an objective analysis (OA) program which used an optimal interpolation scheme to generate a smoothed, uniformly sampled grid of depths from the ensemble of individual depth samples at given (x,y) locations. Initially a 100 x 100 meter, 0.25 m scale grid was developed. At every point on the 400 x 400 point grid, the full data set was searched for points lying within a correlation radius, chosen at 2 m for this analysis. These selected input data were then weighted by a circular Gaussian weighting function with a 2 m diameter, and a least-squares estimate of the mean value was calculated along with an error estimate which accounts for the self-consistency of the points contributing to the mean value. Two meters was selected for the sampling radius to ensure an adequate number of points were used to satisfy the central limit theorem.

4. Weather

Wind data recorded the direction in which the wind was coming from in degrees magnetic. Therefore, it was rotated into the local coordinate system and then 180^{o} was added to it in order to calculate the direction in which the wind was going for comparisons with water column currents measured relative to the ice floe.

III. DATA ANALYSIS AND RESULTS

A. UNDERWATER BATHYMETRY

Central to this study is the roughness of the ice undersurface and how large scale roughness elements interact with the surrounding water column as the ocean moves relative to the ice. The instruments in this study were placed so that the turbulent structure in the water column could be compared between flow arriving across multi-year ice, with small scale roughness features, and the extreme roughness and form drag arising from a large ice keel extending down from the ice floe well into the ocean mixed layer. For this reason the ice undersurface and ice keel was accurately mapped and characterized. The roughness of the ice surrounding the keel must be evaluated in order to compare the turbulence generated as the water flows past those relatively smooth surfaces as compared to turbulences generated when the current is flowing over the keel.

1. High Definition Video of Ice

Prior to collecting sonar data, high definition video was recorded from each morphology data collection site. While not part of the original experiment plan, collection of these images proved to be useful in studying the roughness features of the ice and in attaining details of the ice that could not be seen in the sonar data.

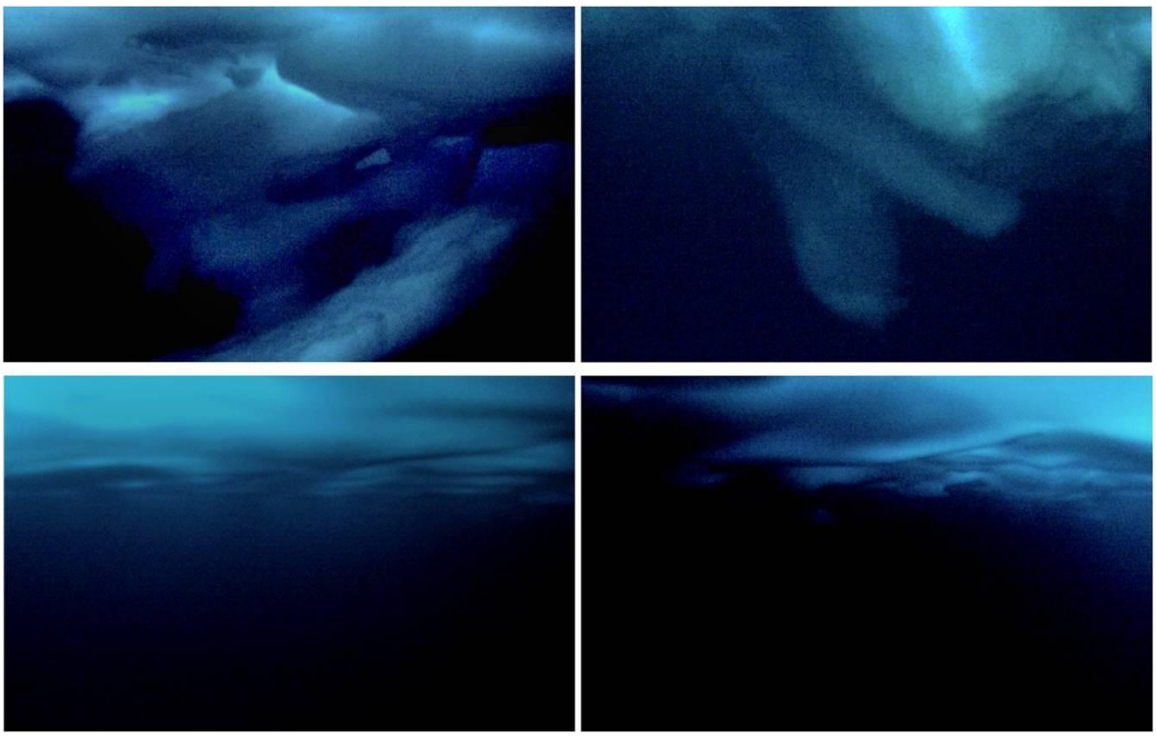

Figure 14. Images of pressure ridge keel taken with a high definition video camera. Image of keel from main hydrohole (upper left). Image of keel from upstream hydrohole (upper right). Image of left side of keel as seen from main hydrohole (bottom left). Image of right side of keel as seen from main hydrohole (bottom right).

Still images from the video (Figure 14), indicate that when two ice sheets collided together, the far ice sheet, in relation to the turbulence mast, subducted under the near ice sheet, causing it to be pushed down in the water column (Figure 15). This is the reason for the smooth leading edge and the rough trailing edge.

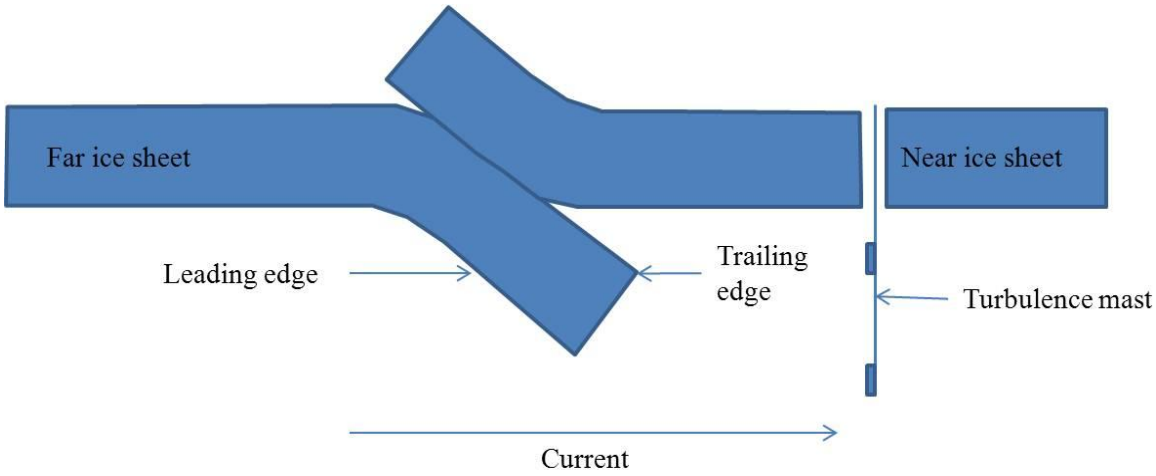

Figure 15. Schematic of ice keel formation.

The images also show that the ice to the left of the keel, as looking from the turbulence mast, is relatively smooth, and that the ice to the right of the mast is slightly rougher in comparing it to the left. This point is significant as it provides an opportunity to evaluate the turbulence created as the current flows past three different degrees of under ice roughness.

2. Sonar

Plots of the underwater ice structure using the sonar data following OA, as described in sections II.B.3 above, are shown in Figures 16–18. The overhead view (Figure 16) indicates that when the current approaches the keel between 54^{o} and 124^{o} (indicated by the blue lines), in the local coordinate system, that the turbulence mast was in the wake of the keel. When the current direction was less than 54^{o} it was approaching from the right side of the keel and greater than 124^{o} it was approaching from the left.

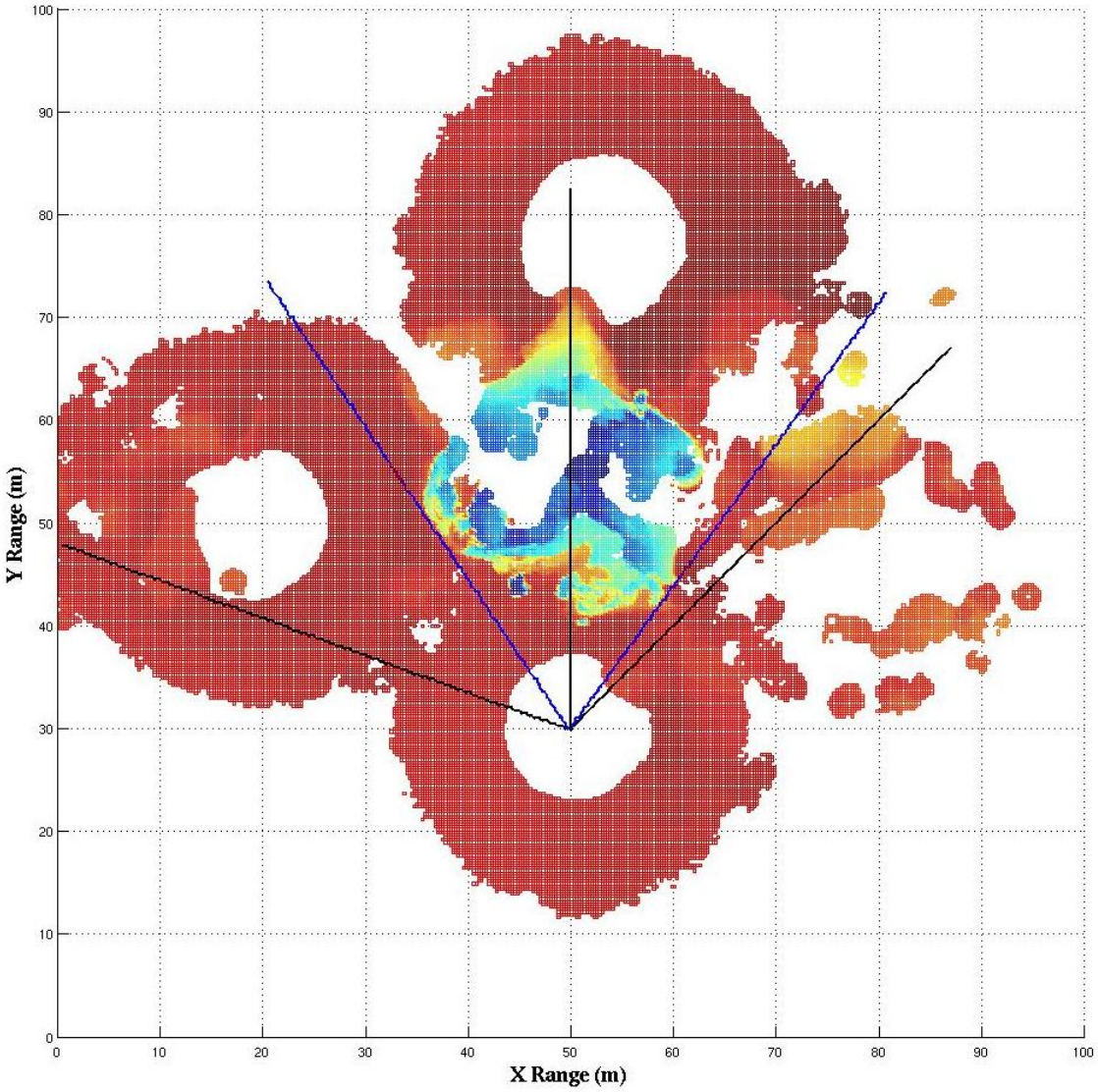

Figure 16. Overhead isotropic view of pressure ridge keel after objective analysis. Point (30, 50) is the location of turbulence mast. Two blue lines indicate the left and right edge of the keel. Three black lines indicate where cross section view of keel was taken as shown in Figure 19.

When comparing the OA sonar data, Figure 17, to the HD video, Figure 14, it is apparent that the sonar was not able to capture all the structural details of the keel, particularly after the sonar data was smoothed by the OA process. However, the details

within the keel are unlikely to be the primary contributors to turbulence generation in the intermediate / far field therefore the loss of the keel structure resolution is not a concern.

The smooth, sloping front of the keel coupled with the rough and blocky back side of the keel shown in Figure 16, strengthens the proposal of how the keel was formed, described in section III.A.1. Also illustrated in Figure 16 is that the main ice keel feature is 33 m long by 29 m across and extends 10 m into the water column.

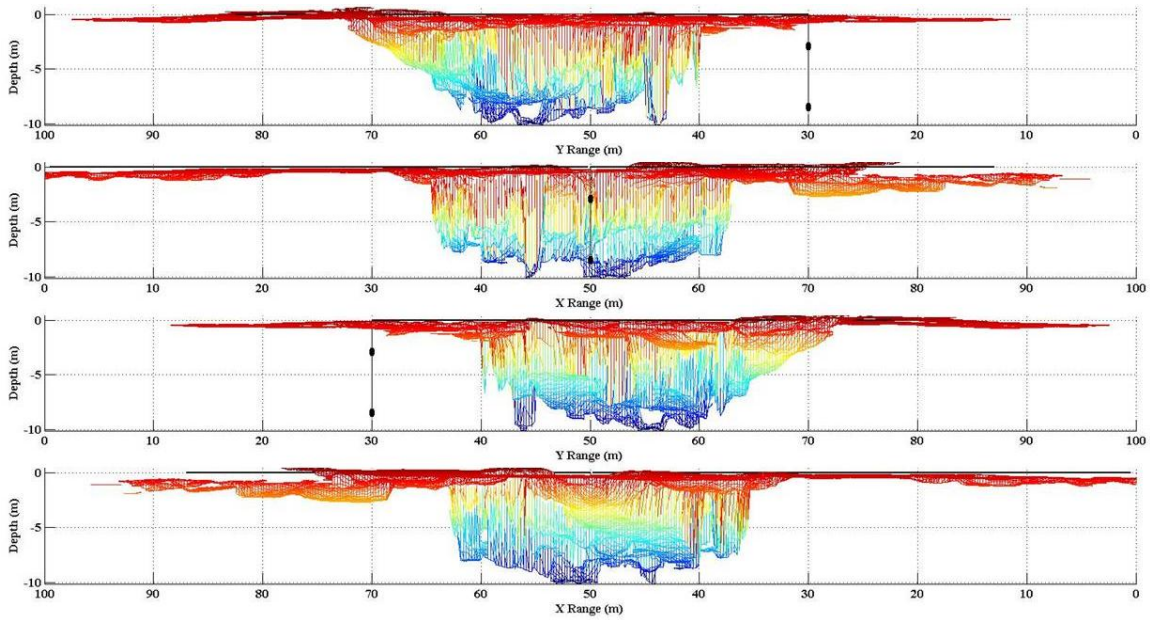

Figure 17. Isotropic view of pressure ridge keel after objective analysis. From top to bottom - left side of keel, back of keel, right side of keel, front of keel. Line with two cylinders at (30,50) indicate the turbulence mast and the two flux packages as they would be positioned during the readings collected 2 m from the ice undersurface.

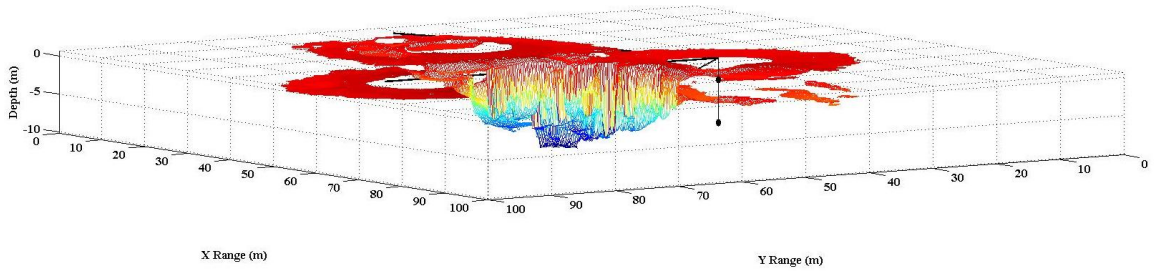

Figure 18. Isotropic bottom left view of pressure ridge keel after objective analysis. Line with two cylinders at (30,50) indicate the turbulence mast and the two flux packages as they would be positioned during the readings collected 2 m from the ice undersurface.

Cross-sections of the ice were then taken from the sonar OA data, one at 045°, 090°, and 160° on the local coordinate plane. This was done in order to analyze how the different ice roughness associated with each cross-section affected turbulence as the current flowed past the ice. Figure 19 confirms the findings from the HD video, that to the right of the keel the ice is rougher then the ice to the left of the keel.

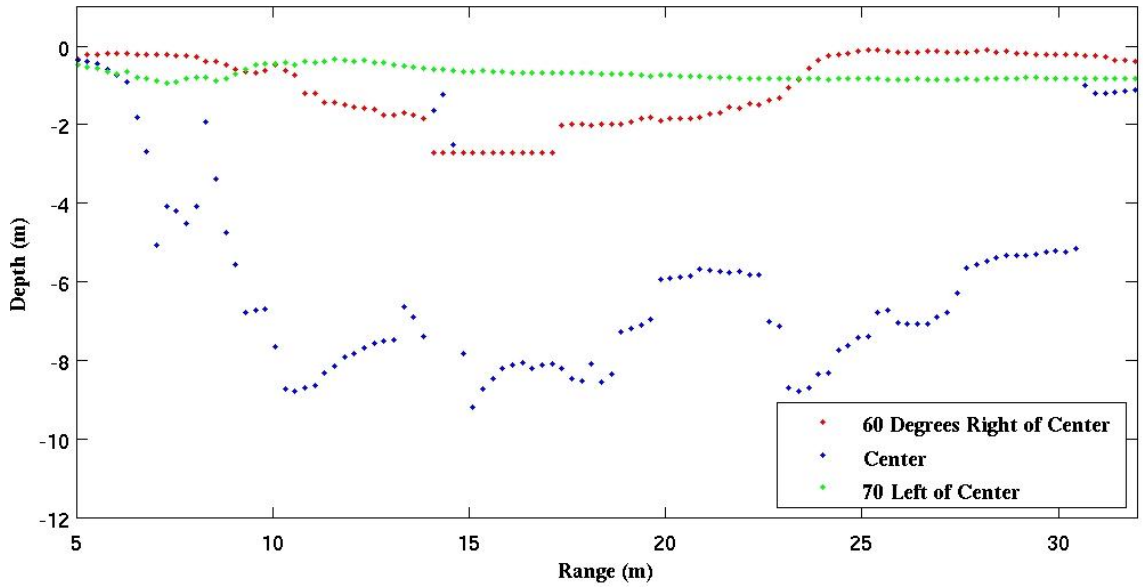

Figure 19. Ice cross-sections. Plot of ice roughness as calculated from sonar OA data.

In order to the parameterize the ice roughness for the three cases of interest, current approaching from left, center, and right of keel, the root mean square (RMS) height, Rq, was calculated (Equation 9), using cross sections of raw XYZ data (Figure 20). The smoothing of the sonar data at scales less than 2 m performed by the OA process makes the processed data unsuitable for this calculation, which is why the raw XYZ depth transect data from single sonar scans were used.

$$Rq = \sqrt{\frac{1}{n}\sum_{i=1}^{n} y_i^2} \qquad (9)$$

The results of these calculations were the cross-section of ice 70^o to the left of the center of the ice keel had an Rq of 0.0908; 60^o to the right had an Rq of 0.2596; and directly in the center had an Rq of 3.2408.

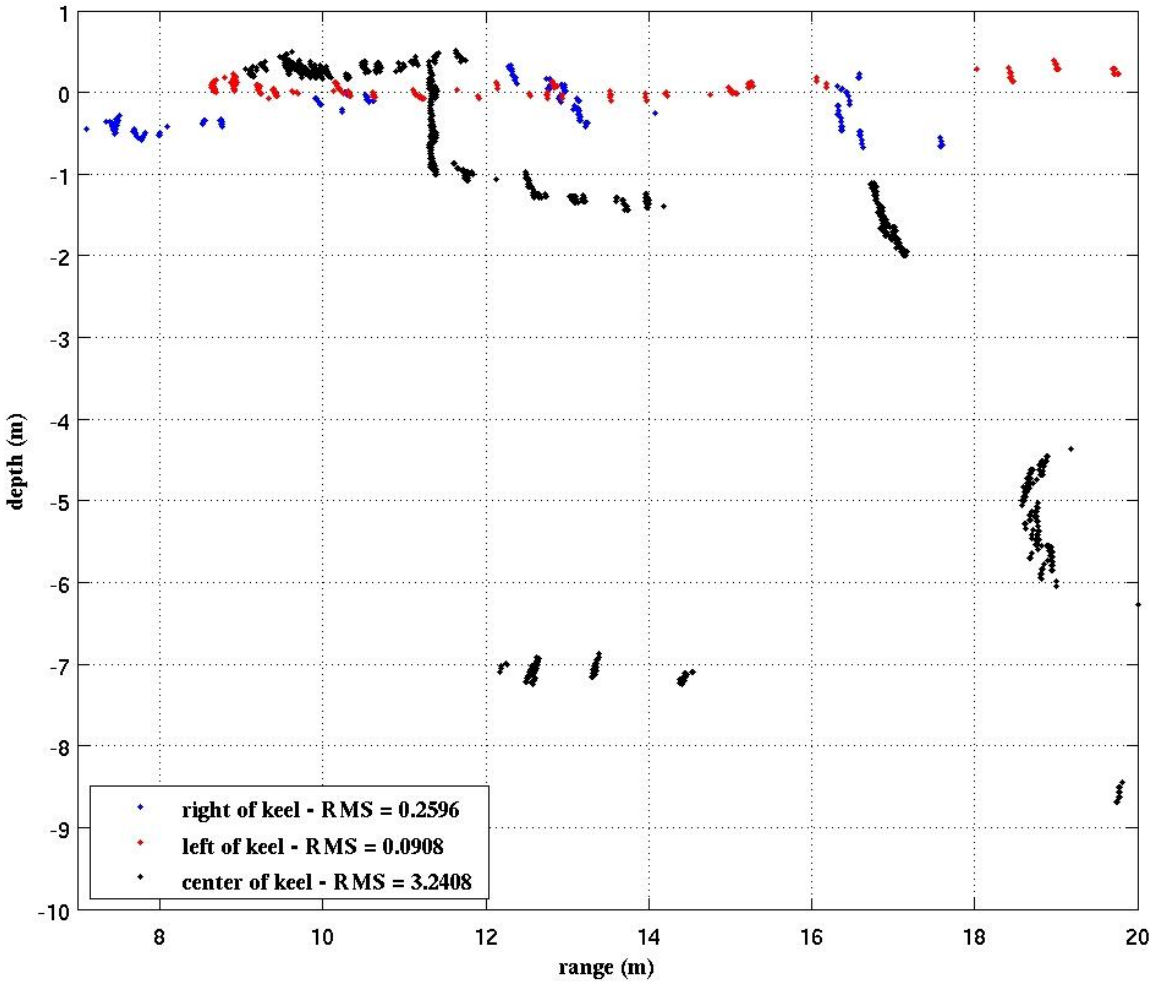

Figure 20. Cross sections of ice from raw XYZ data.

B. MEAN CURRENT PROFILE

The main sources of current relative to the ice during this study, measured by the ADCP and two flux packages, were the wind-driven movement of the ice floe and the underlying flow of the Beaufort Gyre and upper ocean mesoscale features. The movement of the ice, caused by wind forcing and measured with the GPS, created an apparent current at the sensors by moving the sensors through the water. The underlying mean flow of the Beaufort Gyre, which predominantly travels from east to west at the location of the experiment, was calculated by subtracting the ice movement from the measured current, described in Section III.B.2 below.

1. Ice Movement

Figure 21 displays the GPS track of the experiment as recorded by the instrument shed GPS. After a large course change at YD 78.6 immediately following the commencement of data collection, the site traveled primarily to the north-east, before changing course approximately 90^{o} at YD 80.0 and traveling to the north-west. At YD 82.0 the ice floe made a large course changed once again, and began traveling east.

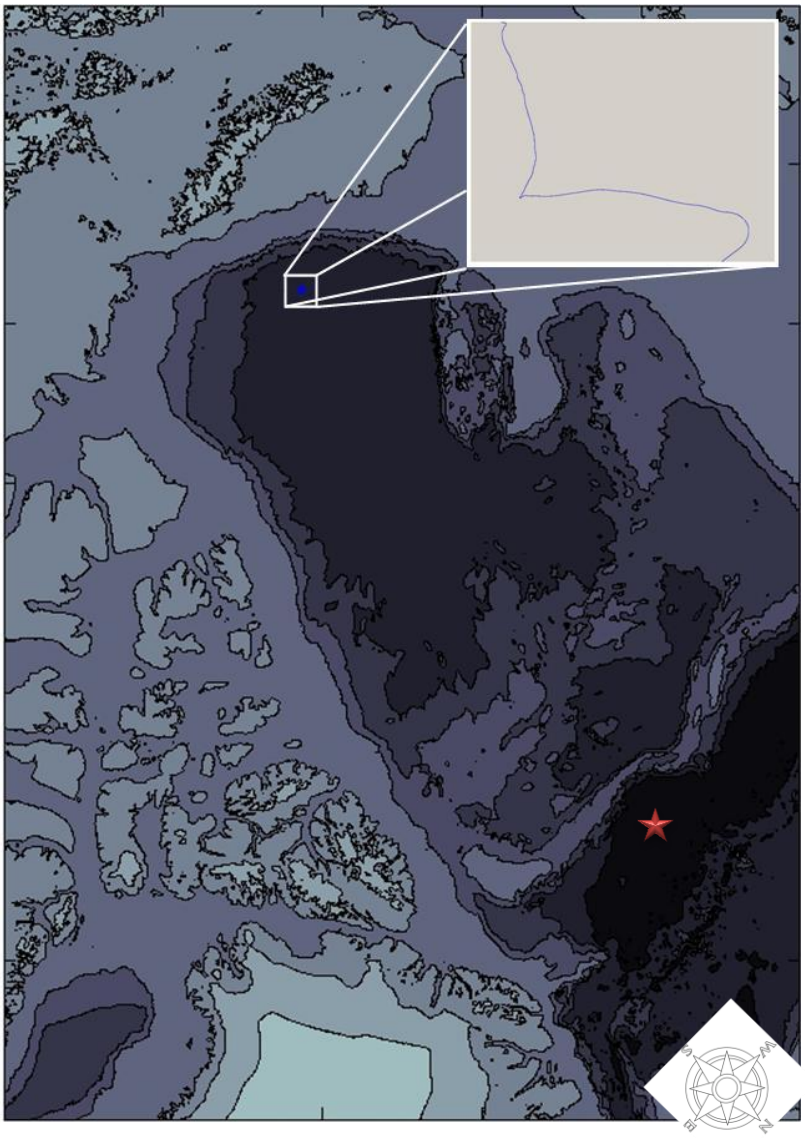

Figure 21. Bathymetry map of Arctic Ocean, and GPS track of ice camp during experiment. Star marks location of the North Pole.

These large course changes can be attributed the changes in wind direction (Figure 22 and 23). The course change at YD 78.6 corresponds to a change in wind direction 45^{o} clockwise then 45^{o} counterclockwise at YD 78.6. The course change at YD 80.0 corresponds to a change in wind direction from 060^{o} at YD 80.0 to 160^{o} at YD 81.0. The course change at YD 82.0 corresponds to a change in wind direction from 160^{o} at YD 81.7 to 040^{o} at YD 82.5. In the case of the course change at YD 80.0 inertial oscillations (Figure 26) were also a significant factor.

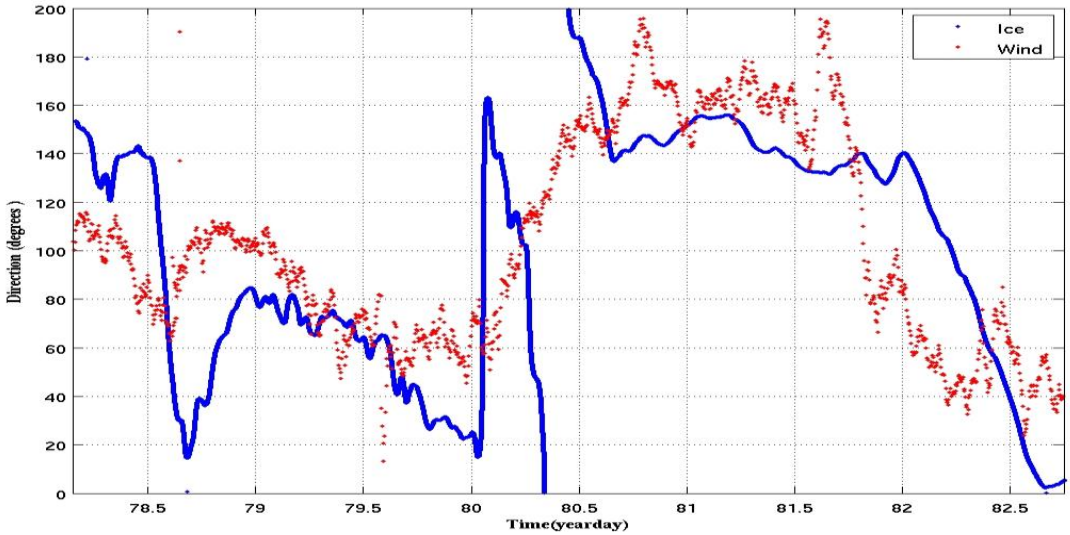

Figure 22. Time series direction of wind and direction of ice floe.

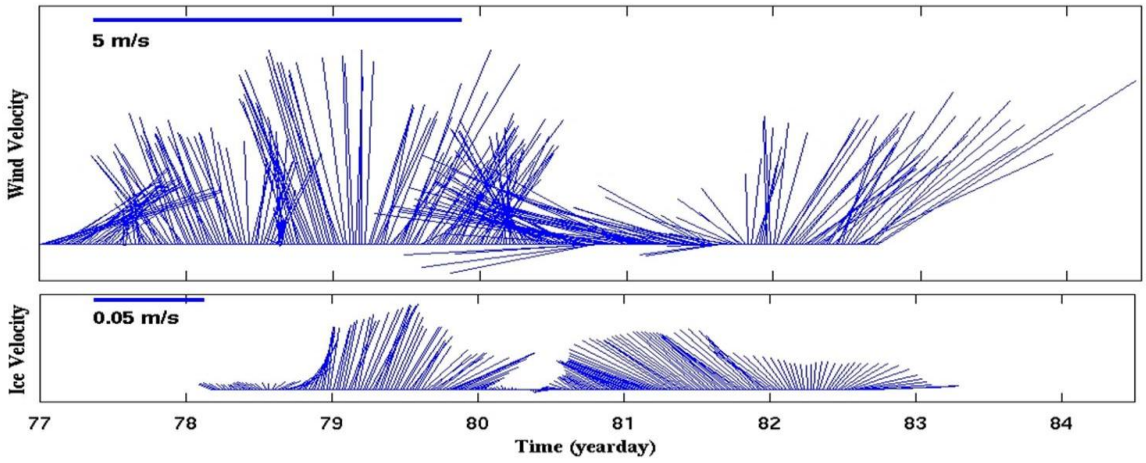

Figure 23. 30-minute average vector plot of wind and ice velocities.

The plot of wind direction and ice floe direction (Figure 22 and 23), shows that often the ice floe direction was to the right of the wind direction. This phenomenon is due to the fact that surface velocity is 45^{o} to the right of surface stress in the northern hemisphere (Ekman, 1905). The noticeable times in which the floe direction is to the left of the wind direction is immediately following a large change in wind direction which is caused by the inertia of the ice floe.

Sea ice moves in response to wind forcing because the wind transfers momentum to the ice. If the wind were to move at a constant velocity the ice would also reach a constant velocity but in a direction to the right of the wind motion. When there is a change in wind velocity (speed or direction) the ice responds slowly to these changes due to the inertia (momentum) of the ice. The ice continues in the initial direction, until the wind exerts enough force to change the ice velocity as well. This is seen in Figures 22 and 23. Following the times of large wind direction changes discussed above, the ice floe changes direction, but takes approximately 0.5 YD to catch up to the wind direction change.

Changes in the wind velocity also led to the inertial oscillations observed (Figure 26). Pollard and Millard (1970) showed that generation of inertial oscillations were a response to an initial impulse of force caused by fluctuations in the wind field under time scales less than an inertial period, approximately 11.97 hours at high latitudes. The large change in wind direction at YD 80.0 (Figure 22, 23, 25b) was sufficient to excite the inertial motion seen in the ice floe track (Figure 26).

A plot of the ice floe speed and direction (Figure 24) shows that when the ice was on a relatively steady track it displayed an increase in speed, but slowed down when it changed direction. In comparing the time series of wind speed (Figure 25a) and ice floe speed (Figure 24b) also indicates a correlation between the two. The increase in ice speed starting at YD 78.6 corresponds to an increase in wind speed during the same time. After the ice slowed in making the course change at YD 80.0, an increase in wind speed once again led to an increase in ice speed.

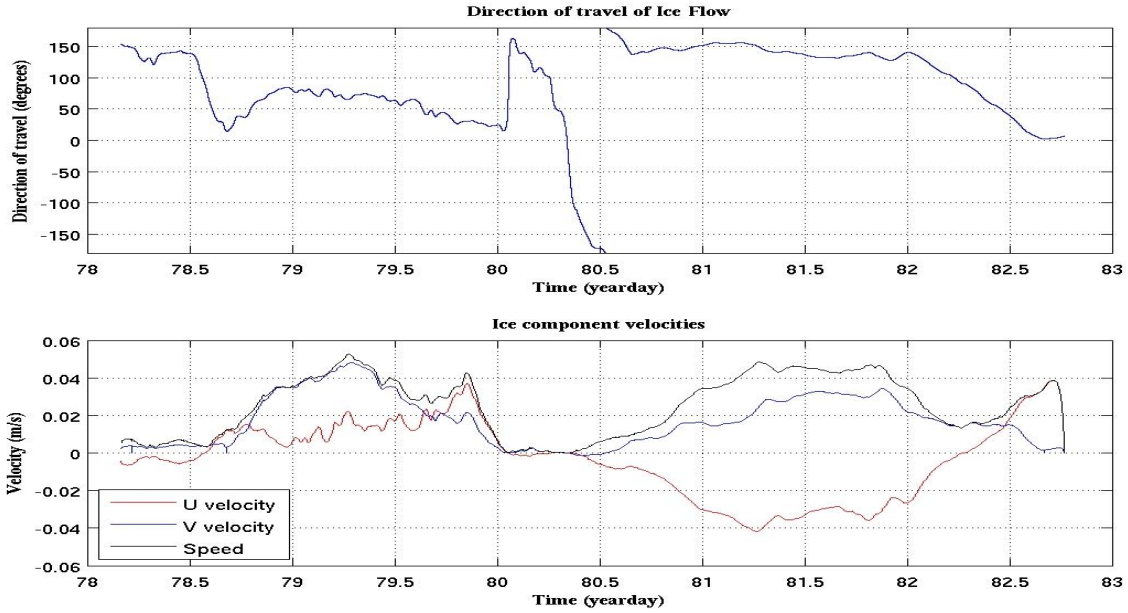

Figure 24. Direction of travel of ice floe, calculated using equation 1. Due north is at 090, east is at 000 (top). Ice component velocities and speed (bottom).

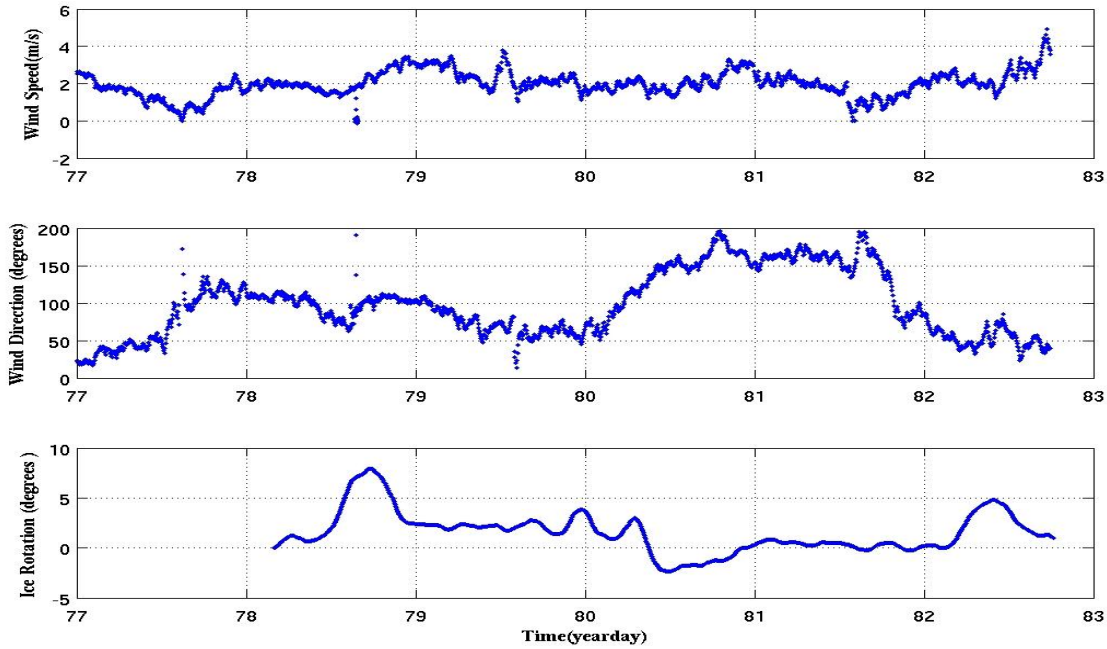

Figure 25. Time series of wind speed collected at ice station command hut (top). Time series of wind direction collected at command hut (middle). Ice rotation calculated from two GPS data sets (bottom).

Not only did changes in the wind speed and direction (Figure 25a and b) and oceanographic inertial oscillations (Figure 26) caused the ice to change direction but also caused the ice floe to rotate during the course of the experiment (Figure 25c). For this study it is important to know how the ice rotated throughout the turbulence data collection, so that the direction of the currents measured by the turbulence mast relative to the ice keel feature is precisely known. Ice floe rotation was calculated using Equation 6, as described in section II.B.1 above.

The large rotation at YD 78.8 is believed to be an effect of the decrease in wind speed at YD 77.7, which may have been associated with wind stress curls, in which the speed fell to 0 m/s (Figure 25a), coupled with 45^{o} clockwise then 45^{o} counterclockwise change in wind direction at YD 78.6 (Figure 25b). Other large ice rotation events are seen at YD 80.4 and 82.5, approximately 0.5 YDs after a large change in wind direction (Figure 25b). The smaller rotation events at YD 80.0 are believed to be due to the inertial oscillations (Figure 26) seen during that time.

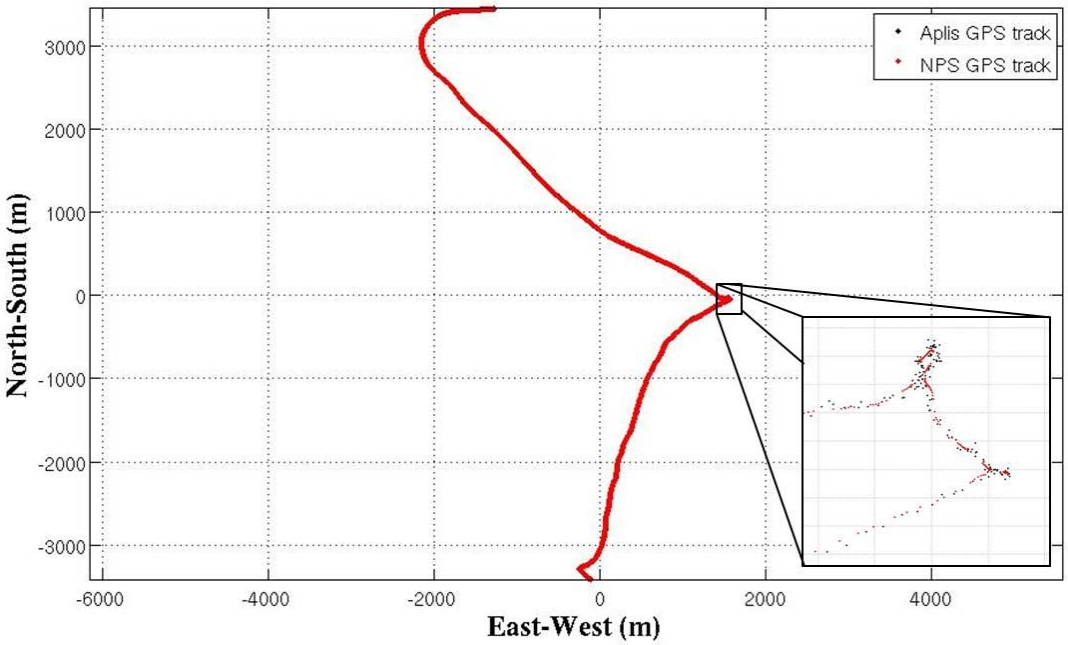

Figure 26. Plot of both GPS data sets, NPS instrument shed (red), and ice station command hut (blue), with enlarged view of an inertial oscillation.

Just as wind transfers momentum to sea ice, the ice also transfers momentum to the mixed layer directly below. If the ice were to move at a constant velocity the mixed layer would also reach a constant velocity but in a direction to the right of the ice motion. The direction of mixed layer movement would continue to rotate to the right of ice motion direction with increasing depth. This phenomenon is known as the Ekman spiral. Speed of this current generated by surface forcing would also decrease with depth.

When there is a change in ice velocity (speed or direction) the mixed layer responds slowly to these changes due to the inertia (resistance to change due to the mass of the ice). The mixed layer continues in the initial direction, until the ice provides enough momentum in order to force the mixed layer to change its velocity as well. Therefore, increases in apparent current speed relative to the ice (Figure 28b) are observed when there is an acceleration of the ice, because the ice is traveling at some new velocity while the mixed layer, due to inertia, is still traveling at a velocity in response to the previous conditions. This is what leads to the spikes in apparent current speeds (Figure 28b) at YD 78.7, 80.7, and 81.2.

2. Beaufort Gyre

The currents recorded by the ADCP and the flux packages are a sum total of currents, indiscriminant of the individual processes that generated those currents. Therefore, subtraction of the ice movement from the total recorded current provides an estimate of the current generated by processes other than ice movement. It is an estimate due to vertical shear in the water column.

The first step in this calculation is to rotate the direction of the u and v components of ice movement by 180^{o}. This is necessary because the apparent current generated by the ice movement is in the opposite direction then that of the ice movement. For example if the ice is moving due north the resulting observed current will be due south.

The following step was to combine the mean currents for each 40–60 minute interval, recorded at different sample depths, into a single vector, for individual sensors

(Figure 27 a, b). In this analysis the ADCP current was calculated to be the mean of bins 6, 7, and 8. This step assumes that the u and v current velocity components had little variation within the upper 25 m of the water column.

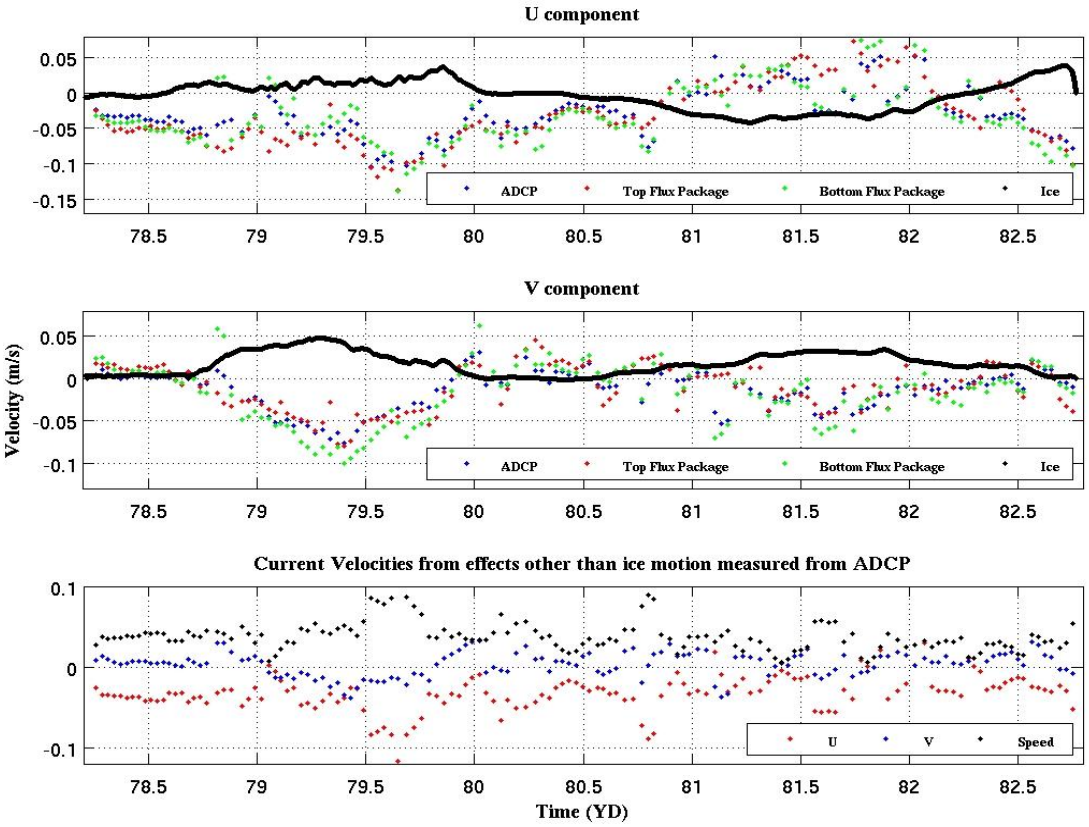

Figure 27. U and V component velocities of ice and current as measured from ADCP and flux packages. Current time series is a combination of current velocities at all sample depths (top and middle). Current produced from effects other than ice motion as calculated from ADCP recorded velocities and ice motion (bottom).

The inverse ice velocity component vectors were then subtracted from the recorded current velocity component vectors resulting in the current contributions from sources other than ice movement (Figure 27c).

The means of each current velocity component from the individual sensors were calculated, and then the mean of the three resulting velocities for each component resulted in a u velocity of –0.033 m/s with a standard deviation of 0.001 m/s and a v

velocity of 0.003 m/s with a standard deviation of 0.003 m/s averaged over the full observation interval. These velocities show a current which is primarily traveling west at approximately 0.03 m/s, corresponding to what would be expected of the Beaufort Gyre at this location (Coachman, 1969).

3. Apparent Current

While it is important to understand the origin of individual processes that contribute to the current, the current relative to the ice is the primary concern of this study, as this is the current that interacts with the ice roughness to produce turbulence within the boundary layer. By calculating the direction of the current (Figure 28a) the ice roughness features the current traveled past upstream of the sensors can be identified. By calculating the speed of the current (Figure 28b), comparisons can be made between the turbulence generated during times of high and low current.

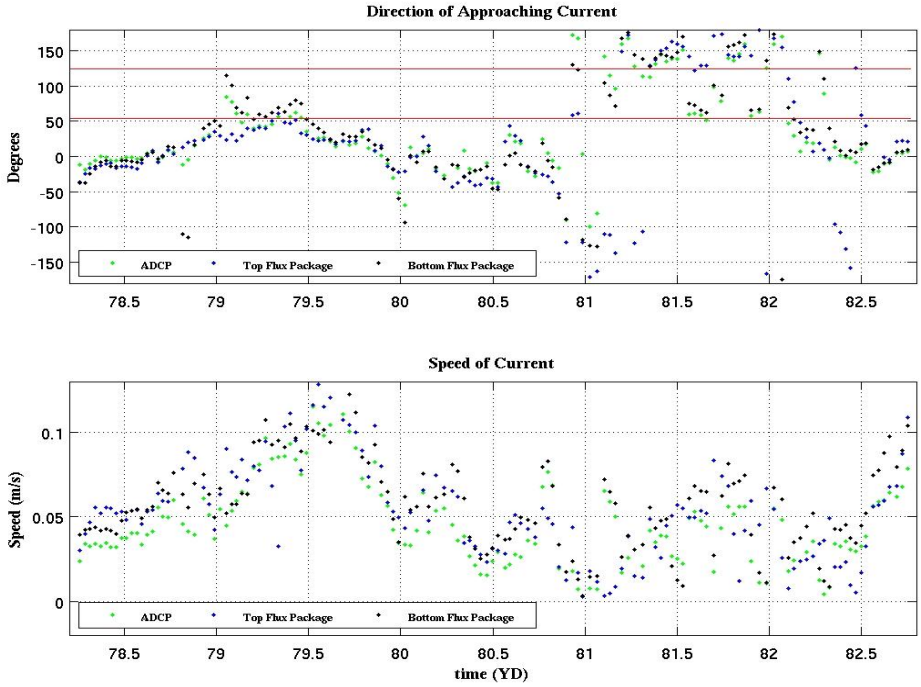

Figure 28. Direction of current travel calculated from ADCP and top and bottom flux package data. Due north is at 090, east is at 000. Area between red lines indicates when current at the turbulence mast is being affected by the keel (top). Current speed, combination of current speeds at all sample depths (bottom).

The direction in which the current is approaching the turbulence mast (Figure 28a) is calculated by substituting the mean component velocity data, u and v, for each 40–60 minute time interval into Equation 6, for the top and bottom flux packages, and using the mean component velocity data of bins 6, 7, and 8 for the ADCP data.

The red lines at 54^{o} and 124^{o} indicate the right and left boundary respectively, for which the current must travel over the ice keel in order to get to the turbulence mast.

Despite the careful consideration when choosing a site in which to deploy the turbulence mast, there are a limited number of instances when the current approached the mast from a direction downstream of the ice keel (Figure 28a). This is due to the relatively benign wind conditions during the logistically-limited data collection interval (Figure 25b). Because of the low wind speeds the background currents provided a larger contribution to the overall current then had been anticipated. Had there been stronger wind forcing, the movement of the ice would have been the primary contributor to the ice-relative current, which would likely have moved the measured current into the wake of the keel.

C. WATER COLUMN STRUCTURE

As discussed in Section II.A.2.*c* above, the CTD profiles (Figure 29) and flux package data indicated that the base of the mixed layer extended 20–25 m into the water column during the first four days of data collection. Only the data collected while the CTD was returning to the surface from depth was used in order to ensure the CTD conductivity sensor had sufficient time to reach thermal equilibrium with the approximately –1.5 ^{o}C seawater compared with the +20 ^{o}C temperature of the hut the CTD was launched from. The last four CTDs, taken during the last day of data collection, indicate that stratification extended up through the seasonal mixed layer so that the base of the mixed layer was within a few meters of the ice interface during that time. This stratification can be expected to significantly alter the turbulence characteristics of the boundary layer below the ice by limiting the penetration depth of turbulent motions.

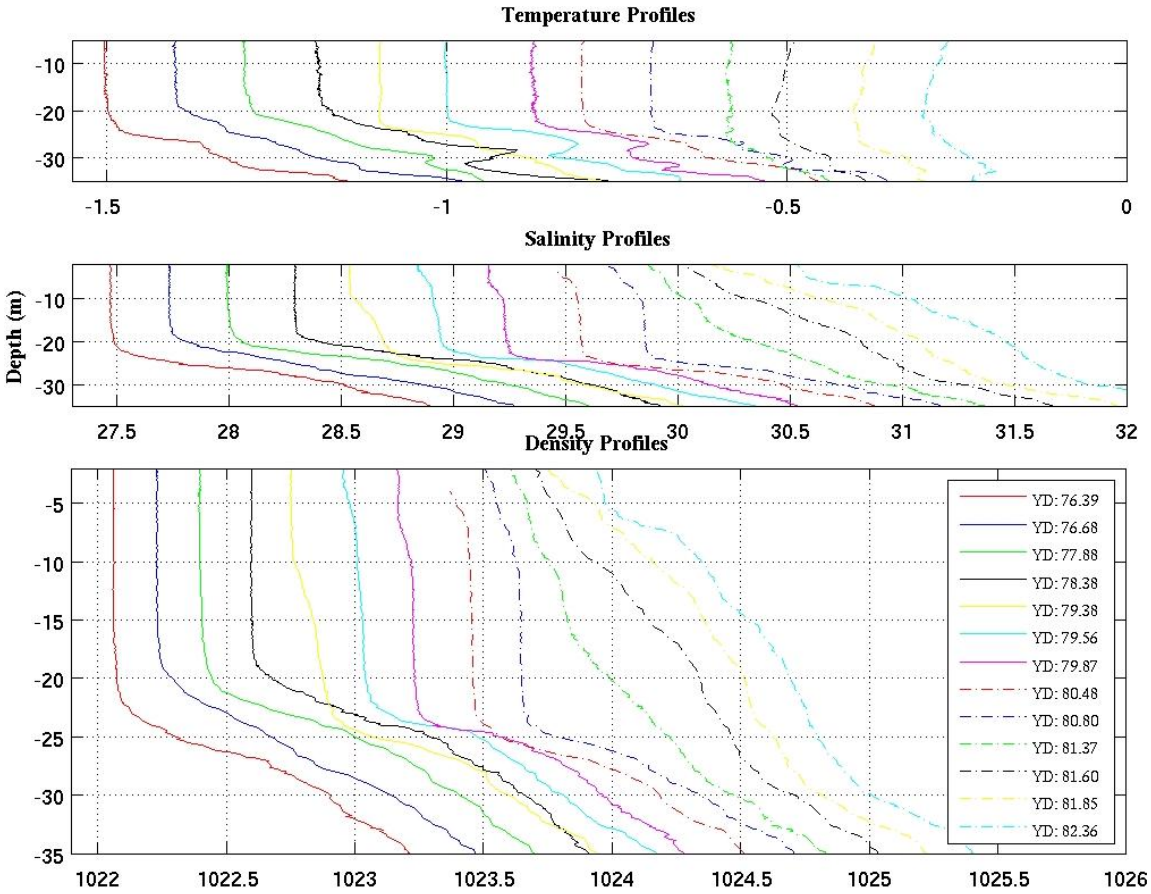

Figure 29. Seawater temperature, salinity, and density profiles attained from CTD casts. Each subsequent profile is shifted right by 0.1 ^{o}C, 0.3 psu, and 0.2 kg/m^{3}, respectively.

Examining the first four density profiles (Figure 30) in greater detail, of which the first three were taken prior to recording turbulence data, show that the mixed layer depth remained relatively constant at approximately 20 m with very little stratification within the mixed layer.

Due to the lack of stratification, turbulence created at the ice-ocean interface has the ability to extend down from the hydraulically rough ice surface to the seasonal pycnocline because the stratification is not present as a stabilizing force to work against vertical turbulent eddy motions.

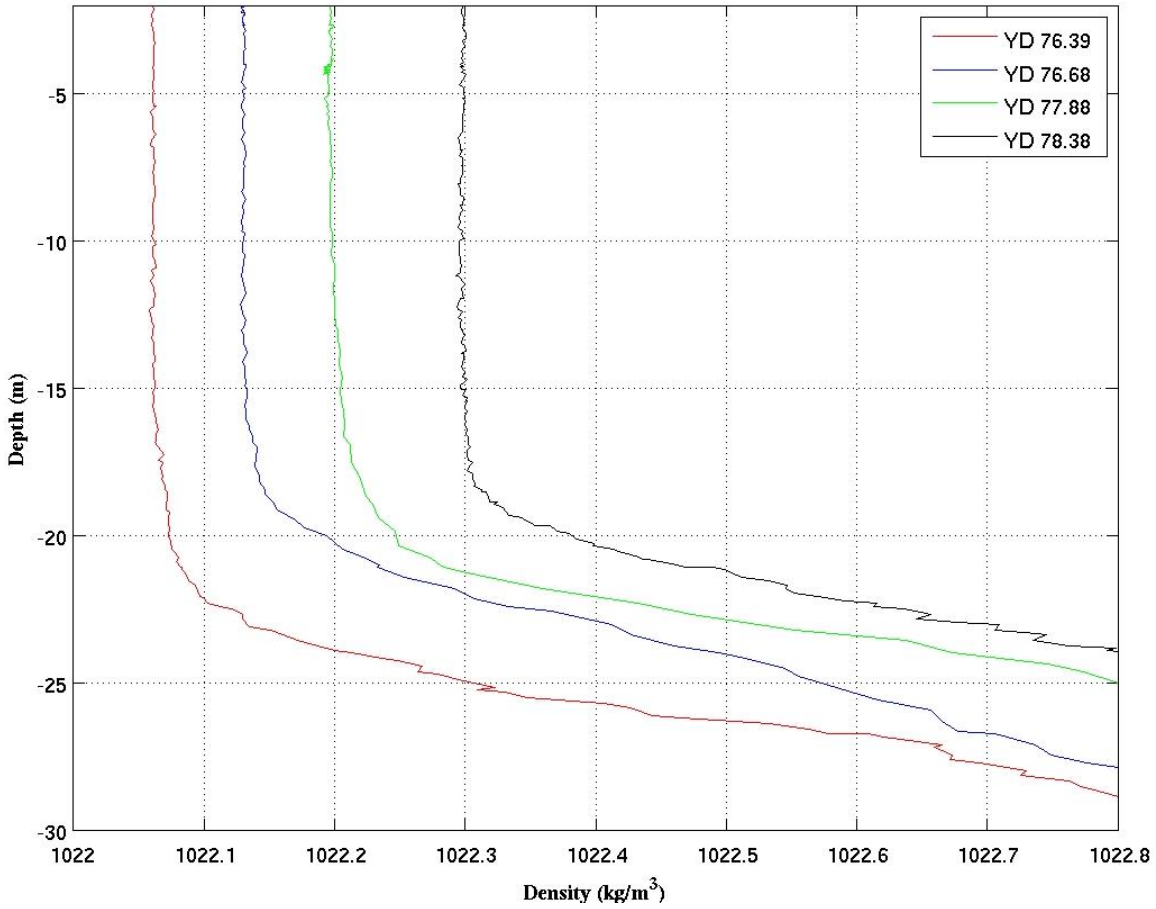

Figure 30. Seawater density profiles attained from CTD casts recorded between YD 76.39 and 78.38. Each subsequent profile is shifted right by 0.1 kg/m^3.

A detailed view of the following five CTD casts (Figure 30) show a deepening of the mixed layer to 24 m during YDs 79.38, 79.56, and 79.87. The mixed layer once again increased to 25 m during YDs 80.48 and 80.80. This mixed layer deepening is most likely the result of an increase in current speed (Figure 28) caused primarily by an increase in ice speed (Figure 24). The increased speeds created greater turbulence near the ice-ocean boundary layer, and this greater turbulence cause more mixing which led to entrainment at the base of the mixed layer, and an increase of the mixed layer depth. These casts also show that the mixed layer was slightly stratified. Even this slight stratification would serve as stabilization force to dampen the turbulence created at the ice-ocean interface.

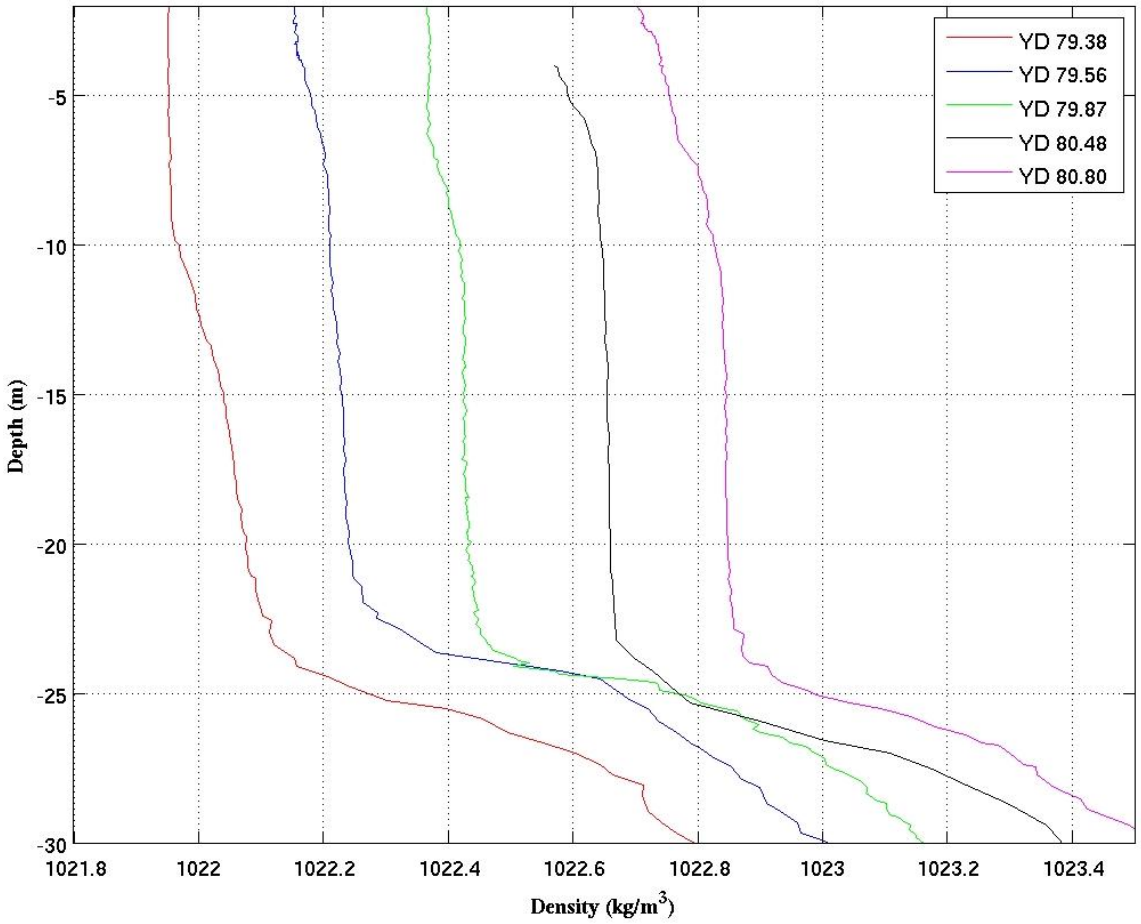

Figure 31. Seawater density profiles attained from CTD casts recorded between YD 79.38 and 80.80. Each subsequent profile is shifted right by 0.2 kg/m^3.

The last four CTD casts taken between YD 81.37 and 82.36 (Figure 32) indicate that near-surface waters stratified, effectively eliminating the surface mixed layer. The first cast that displays this shallow mixed layer, taken at YD 81.37, followed the current speed decreasing to less than 0.01 m/s at YD 81.0. Consequently, the very low current relative to the ice allowed the pycnocline to feather and diffuse up toward the ice/ocean interface, because at 1cm/s there is very little turbulence production near the interface that could mix out this stratification.

As the speed of the current (Figure 28) increased after it reached its minimum at YD 81.0, the reformation of a shallow mixing layer can be seen in the density profiles by

YD 82.36. At YD 82.36 the depth of the mixed layer base deepened to approximately 5 m, as the surface-generated turbulence mixes out to result in weak stratification down to 5m depth relative to the stronger near-surface stratification that formed during the very low earlier currents relative to the ice.

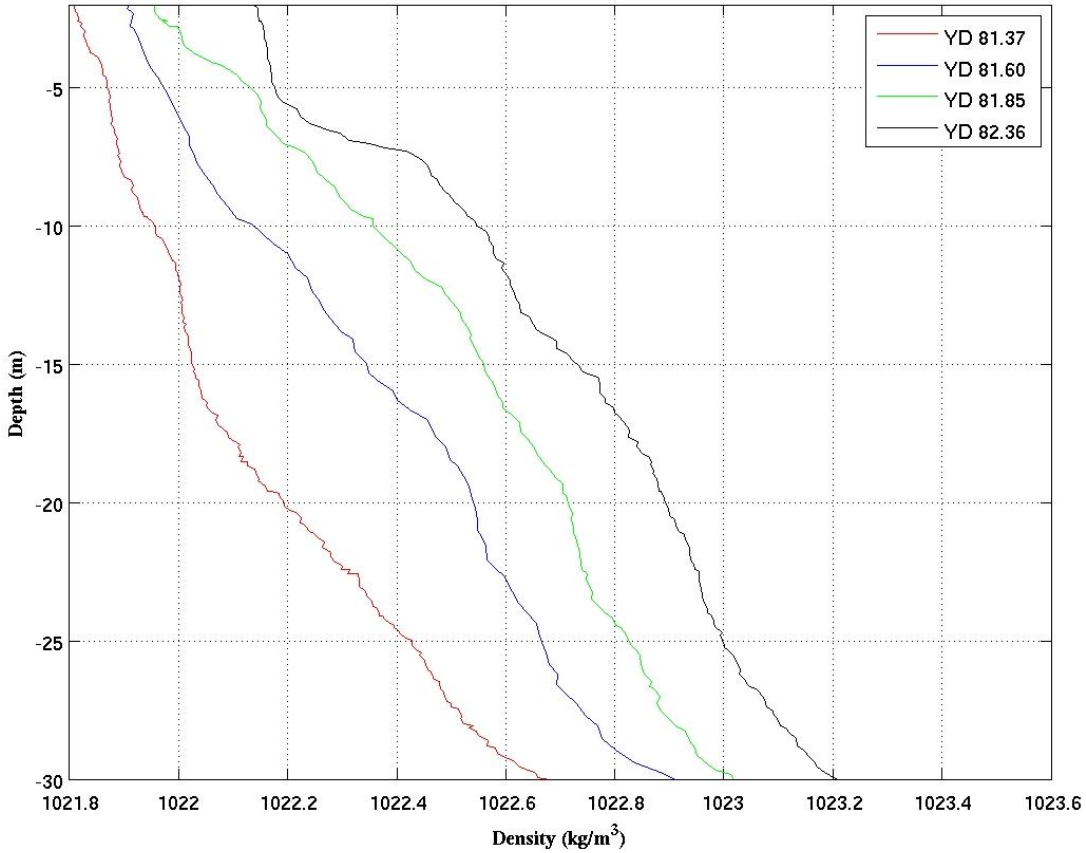

Figure 32. Seawater density profiles attained from CTD casts recorded between YD 81.37 and 82.36. Each subsequent profile is shifted right by 0.2 kg/m^3.

D. TURBULENT FLUXES

A 42-minute time series is shown in Figure 33 to illustrate the turbulent processes observed 2 m from the ice interface. The displayed time series was recorded when the mean apparent current had a speed of 0.102 m s^{-1} and was approaching 5^o to the right of the right edge of the keel. Mean heat flux of 1.396 W m^{-2} and a mean salt flux of –1.182

$x10^{-7}$ psu m s^{-1} were calculated. This indicates that over this particular Reynolds averaging period, there was an overall upward movement of heat at a rate of 1.396 W m^{-2} and an overall downward movement of salt at a rate of 1.182 $x10^{-7}$ psu m s^{-1}.

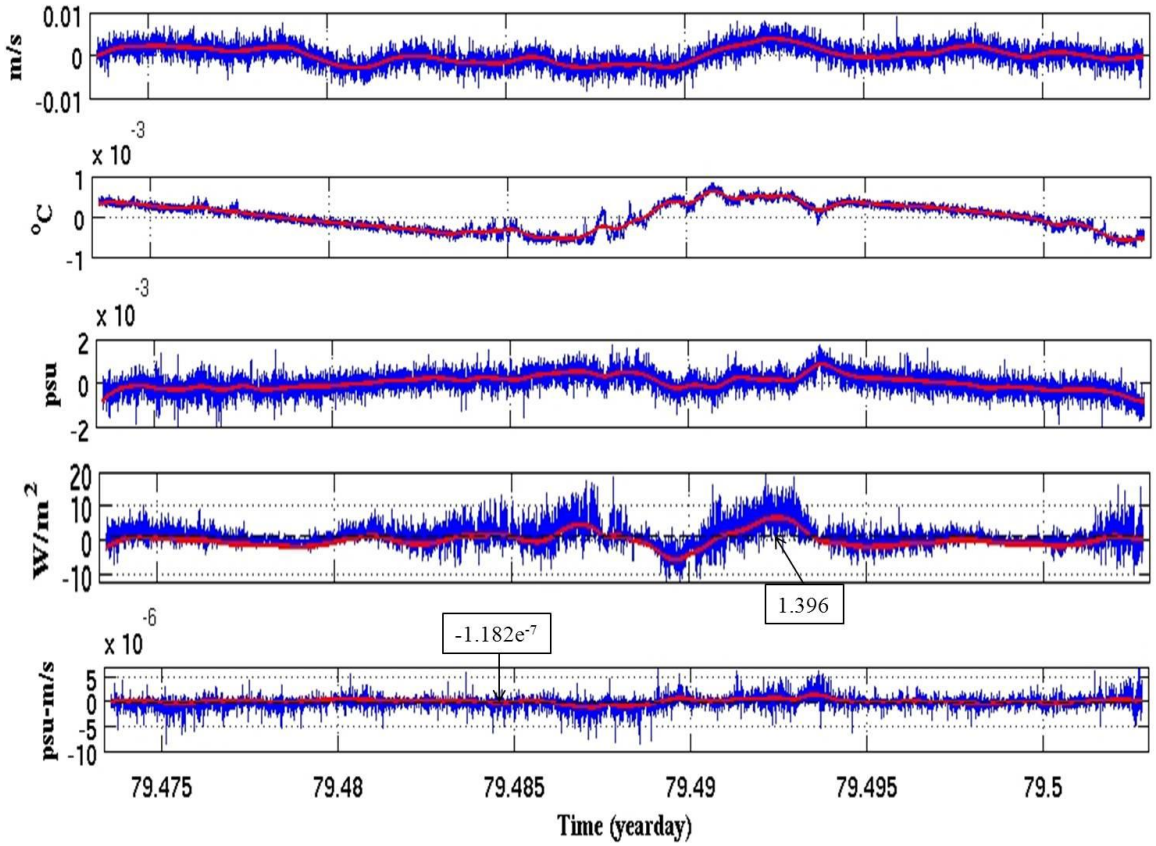

Figure 33. Forty-two minute time series of vertical velocity w, deviatory temperature T', and salinity S' (linearly detrended) for top flux package 13.9 m below ice undersurface. Also shown are instantaneous heat and salt fluxes. Average values of the fluxes are 1.396 W/m^2 and $-1.182X10^{-7}$ psu m/s. Filtered data is plotted in red. Data filtered with a 4th order lowpass filter with a 0.005 cutoff frequency.

In order to understand the eddy-correlation heat flux calculation more completely a one minute time series of scaled w'T' correlation data (Figure 34) was selected from the heat flux data shown in Figure 33. Magnified view of heat flux data (Figure 34) indicates that for every increase in flux, immediately following is a decrease in flux. This is attributed to the quasi-circular motion of eddies. As an eddy moves past a sensor the

leading edge may carry warm water up in the water column. Using the direct covariance method to calculate flux a positive deviatory temperature multiplied by a positive vertical velocity would lead to a positive flux. As the eddy continues to move past the sensor, the trailing edge of the eddy would carry the same warm water down in the water column, with a slightly reduced T' due to small scale mixing, therefore a positive deviatory temperature multiplied by a negative vertical velocity leads to a negative flux.

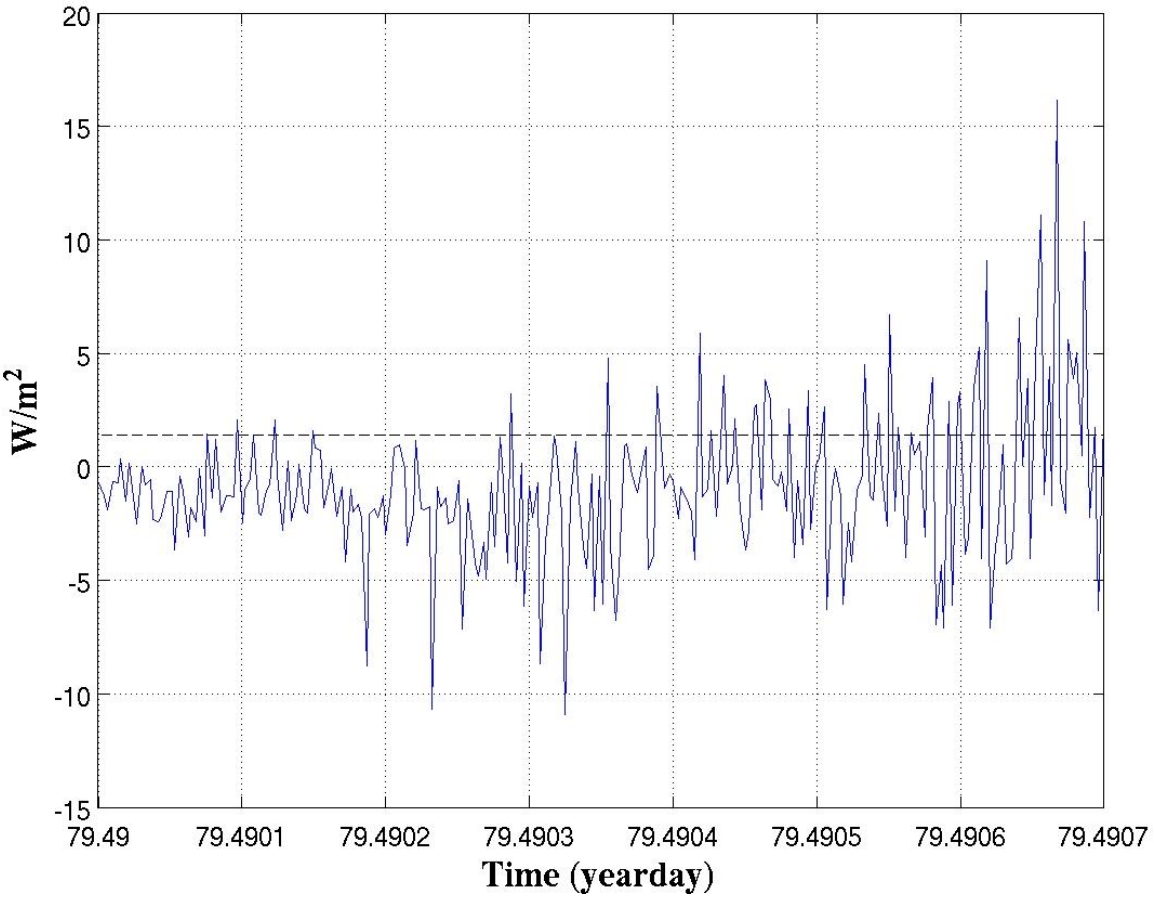

Figure 34. One minute time series of instantaneous heat flux selected from time series data shown in Figure 33.

E. ENERGY DENSITY SPECTRA

The energy density spectra of vertical velocity as a function of wavenumber, $S_{ww}(k)$ were calculated for each nominal 40 minute sampling interval throughout the

experiment. Spectra from a 42.6-minute time series with a mean collection time of YD 81.76 and is displayed in Figure 35 to illustrate the turbulent processes observed. This time series was collected from the upper turbulence sensor on the frame which was 1.9 m below the ice-ocean interface. The mean current was approaching from 20° left of the keel at a speed of 0.068 m/s.

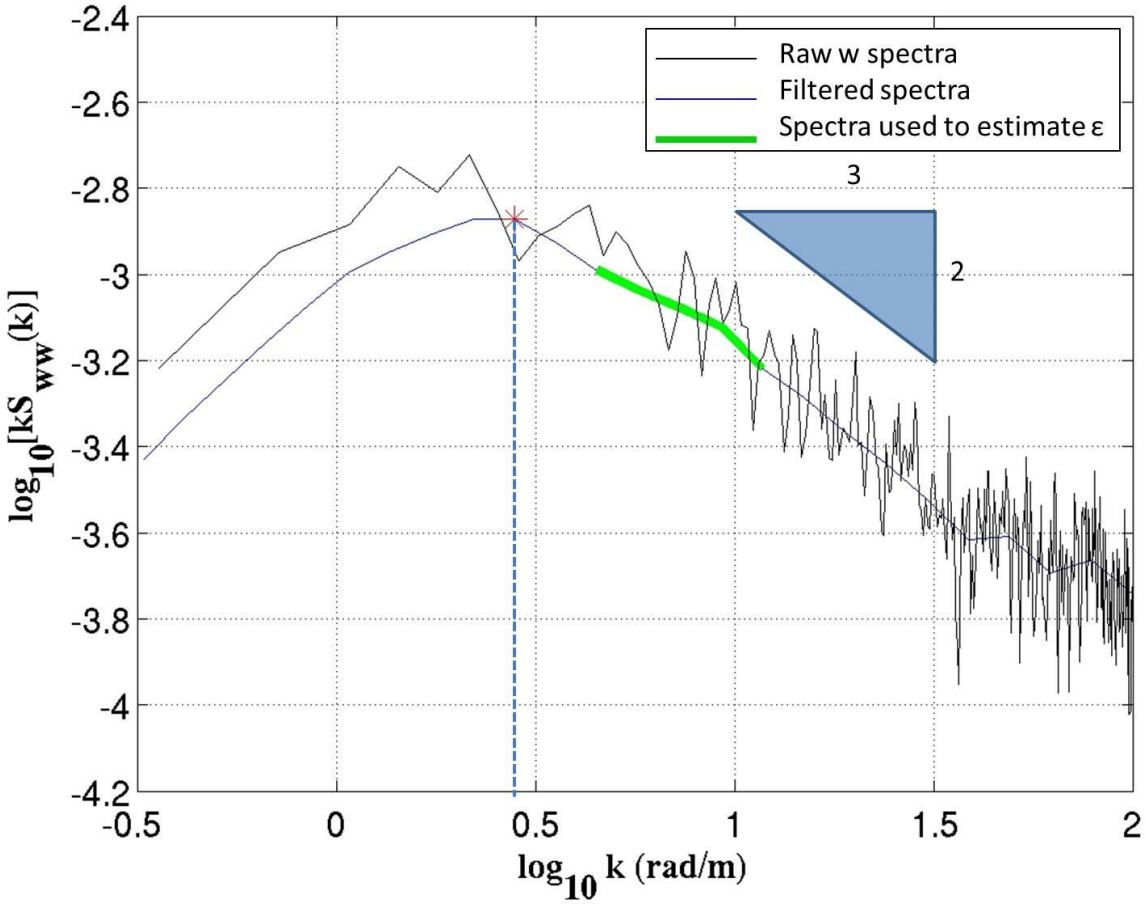

Figure 35. Plot of Sww(k) spectrum calculated from a 42.6-minute time series with a mean sample time of YD 81.76. Black line is the raw spectrum; blue line is the filtered spectrum. Red star indicates the peak in the spectra and the dashed vertical line indicates the wavenumber at the maximum from which λ is calculated. The green line indicates the section of spectra in the inertial subrange used to estimate ε.

TKE dissipation ε is obtained from the spectral density evaluated at a 3–10 cpm wavenumber range within the inertial subrange, indicated by the thick green line in Figure 35, using Equation 3. For the sample displayed the dissipation rate was estimated

to be 4.576 x 10^{-8} m^2/s^3. The wavelength of the smoothed spectral peak (vertical dashed line in Figure 35) was used with Equation 4 to estimate the mixing length λ, which for this sampling interval was estimated to be 0.303 m.

For the relatively weak mean currents encountered during the experiment, the turbulent levels were sufficiently low that instrument noise affected the vertical velocity spectra. This is illustrated in Figure 36. The instrument noise was a factor of 5 higher than the design level of 1 mm/s RMS due to a firmware processing error that was discovered after this experiment, but for the most part, the dissipation rates and spectral peaks were well resolved. In cases where the noise floor dominated, both dissipation and mixing length λ were assigned to null NaN values in the following analyses.

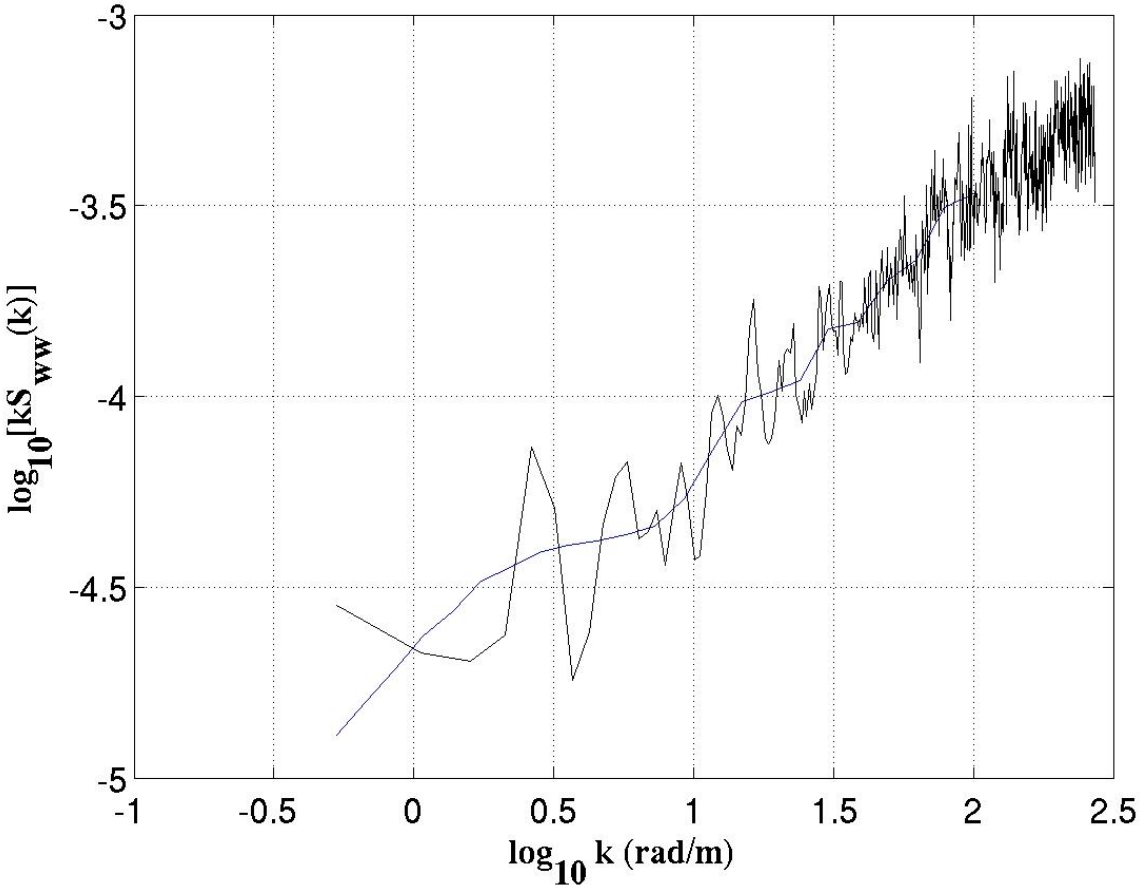

Figure 36 Plot of Sww(k) spectrum calculated from a 42-minute time series collected 20 m below ice-ocean interface with a mean sample time of YD 80.7. Black line is the raw spectrum; blue line is the filtered spectrum.

THIS PAGE INTENTIONALLY LEFT BLANK

IV. DISCUSSION AND CONCLUSIONS

During the APLIS 2011 ice camp, a 3-D sonar was used to record high resolution morphological measurements of a pressure ridge keel measuring 33 m long by 29 m across by 10 m deep (Figures 16–18 and 37).

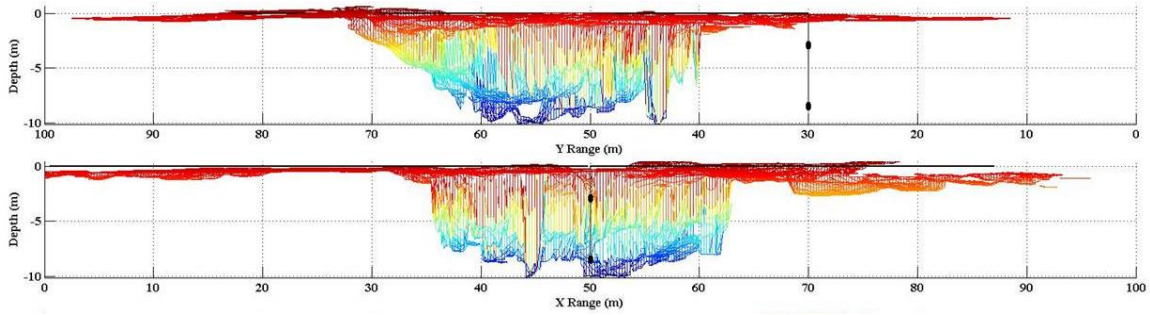

Figure 37. Isotropic view of pressure ridge keel after objective analysis. Top is left side of keel and bottom is the back of keel. Line with two cylinders at (30,50) indicate the turbulence mast and the two flux packages as they would be positioned during readings collected 2 m from the ice-ocean interface.

Sensors were deployed in the water column approximately 10 m from the keel to record salinity, temperature, and 3-D velocity time series at two depths concurrently to allow turbulent fluxes and dissipation rates to be estimated as the changing currents interacted both with the smoother multiyear ice pack and the steep ice keel feature. The small scale fluctuations in temperature, salinity and velocity were used to calculate turbulence levels, scales and resulting fluxes within the Arctic Ocean mixed layer, and gain a greater understanding of how keels effect turbulence generation.

Throughout the course of the experiment benign weather conditions (Figure 25) resulted in low ice velocities (Figure 24). The slow movement of the ice had two direct implications on the experiment. One, the turbulence mast was placed such that it would be in the wake of the keel had there been typical wind velocities for that time of year. Due to the low wind speeds the underlying geostrophic flow of the Beaufort Gyre contributed to the relative current more significantly then had been anticipated; therefore,

the turbulence sensors spent little time in or near the wake of the keel. Secondly, low surface forcing led to relatively weak turbulence levels. The weak turbulence make the data more difficult to interpret, but more importantly it led to moderately to intensely stratified conditions within the remnant mixed layer (Figure 38), which provided an opportunity to study weakly stratified flow past the ice keel.

A. STRATIFICATION EFFECTS

In an ocean surface boundary layer underneath ice, turbulence scales increase in scale with distance away from the interface out in to the planetary boundary layer where Coriolis effects limit turbulent scales (McPhee 2002). The presence of even very weak stratification (vertical density gradients) sharply limits the depth of the active turbulence. In a stratified water column turbulent eddies must work against gravity in addition to friction. Therefore, when there is even moderate stratification, eddies lose their energy more rapidly, resulting in rapid attenuation with depth into the stratified part of the water column.

CTD profiles (Figure 38) indicate that the mixed layer was close to neutral up to YD 78.38, then became moderately stratified up to YD 80.80, and then became significantly stratified for the remainder of the experiment as the relative current approached zero from YD 80–80.4. CTD casts taken at YDs 79.38, 79.56, and 82.36 (highlighted with think lines) (Figure 38), are of particular interest as they were recorded when the turbulence sensors were in the wake of the keel.

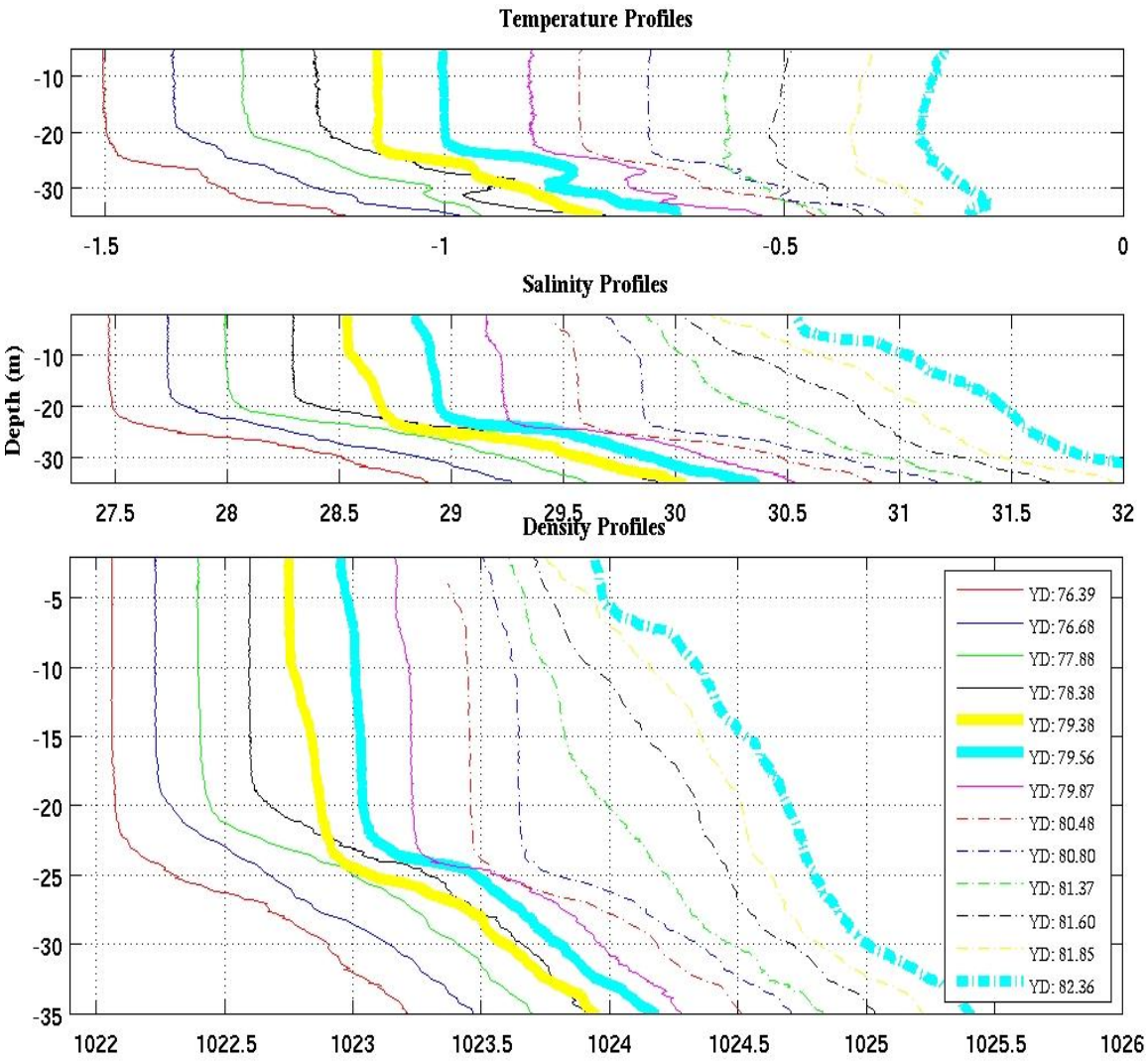

Figure 38. Seawater temperature, salinity, and density profiles attained from CTD casts. Each subsequent profile is shifted right by 0.1 ^{o}C, 0.3 psu, and 0.2 kg/m^{3}, respectively. Thick lines indicate casts taken when turbulence mast was in the wake of the keel.

B. FRICTION VELOCITY

Time series of 40–60 minute time averages of turbulent friction velocity u* (Equation 5) are displayed on Figure 39. Between YD 78.2–78.75 u* increased as current velocity increased. An increase in u* with depth from 2 m below the ice-ocean interface to 8 m is also shown. During SHEBA, McPhee (2002), noticed the same

phenomena and attributed it to a response to larger roughness elements that may be as far as 120 m upstream. In analyzing the sonar data (Figure 16) the rubble field from the collision of the two ice floes that created the selected keel appears to extend to the right of the data collection site, therefore it seems reasonable that there could be another large keel within a 120 m that would cause this flow disruption.

During the initial, weak stratification period, YD 78.2–79.3, u* reached a maximum at both 2 and 8 m when the current placed the instrument frame downstream from the keel A large increase in u* is also seen between YD 81.5–82. This large increase, particularly at 2 m below the ice-ocean interface, is attributed to increased effective roughness of the flow due to interactions with the keel. The increasing but still weak stratification reduced the stress seen at 14 m and 20 m depth during this time.

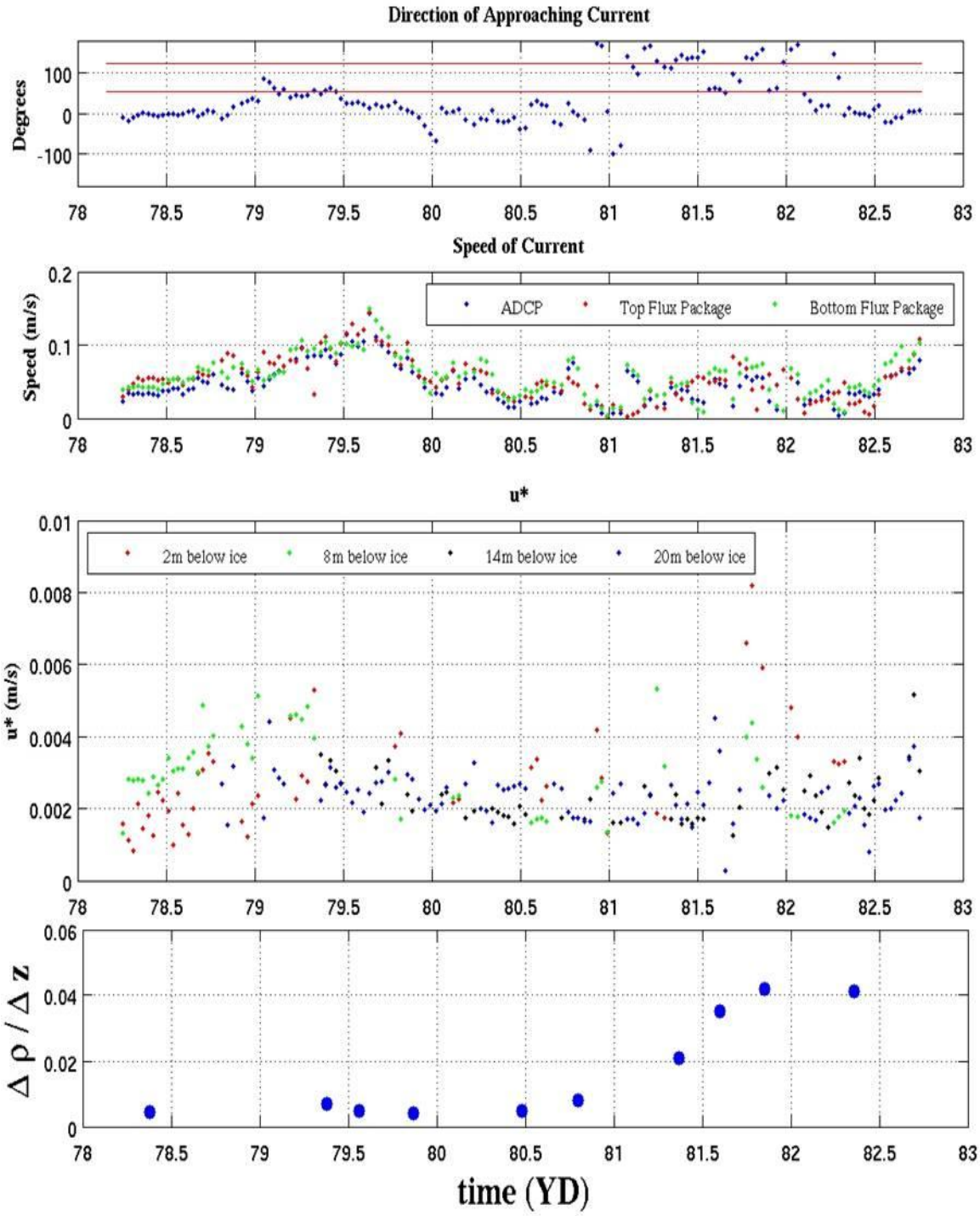

Figure 39. Time series of 40–60 minute time averaged (from top to bottom) current direction calculated from ADCP data, current speed, friction velocity u*, and water column stratification expressed in $\Delta\rho/\Delta z$. Red lines on current direction plot indicate right and left edges of the keel.

C. SPECTRAL ESTIMATES

From the vertical velocity energy density spectra Sww(k) the mixing length λ and TKE dissipation rate ε were calculated in order to evaluate their response to keel effects. Frequency spectra were also analyzed for evidence of internal buoyancy fluctuations in the weak stratification downstream from the ice keel.

1. Mixing Length (λ)

Time series of 40–60 minute time averaged values of mixing length λ (Equation 4) are displayed on Figure 40. As expected the mixing length increased with depth due to the increased distance from the ice boundary, however this increase was smaller than expected. This result is due to the stratification of the water column. The stratification worked to hold turbulent eddies tightly together decreasing their size. There also appears to be a strong correlation between the mixing length λ and current velocity. At all sample levels the mixing length increased with current speed (Figure 41). As the speed of the ice increased greater energy was supplied to eddies allowing them to increase in size. The effect of the current speed decreased at 2 m, as indicated by the smaller slope (Figure 41). This is due to the proximity to the ice surface boundary, which limited the size of turbulent eddies. Water column stratification and ice velocity appear to impact the magnitude of λ however there is no evidence that current interactions with the keel had any effect on λ.

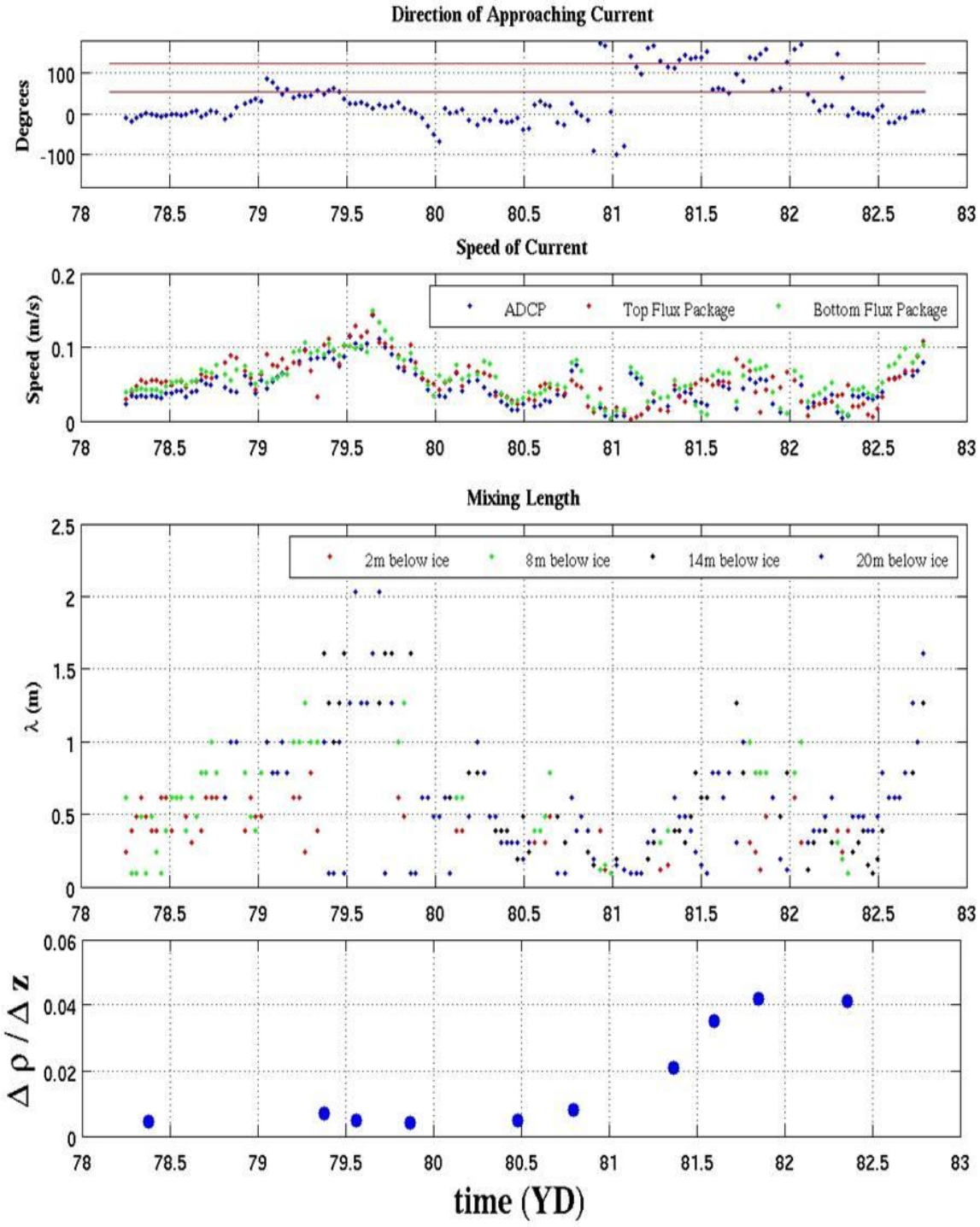

Figure 40. Time series of 40–60 minute time averaged (from top to bottom) current direction calculated from ADCP data, current speed, mixing length λ, and water column stratification expressed in $\Delta\rho/\Delta z$. Red lines on current direction plot indicate right and left edges of the keel.

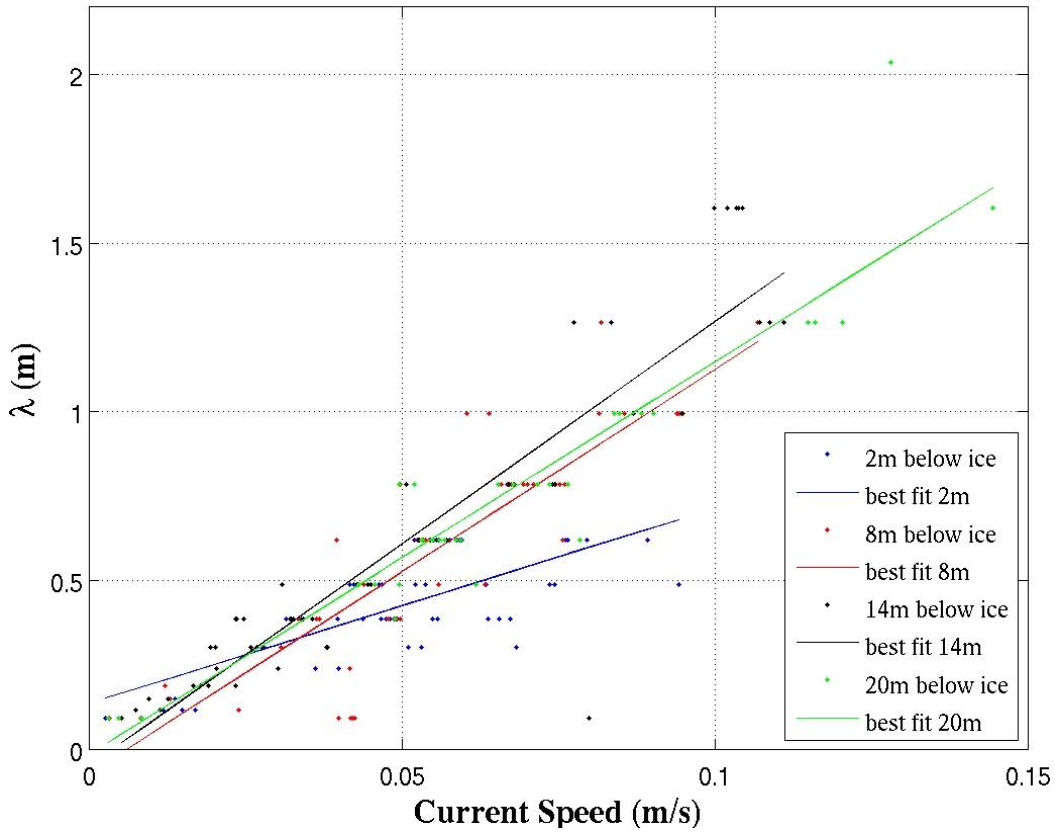

Figure 41. Plot of current speed vs. mixing length λ.

2. TKE Dissipation Rate (ε)

Time series of 40–60 minute time averaged values of TKE dissipation ε are displayed on Figure 42. Throughout the experiment the largest dissipation rates are seen at 2 m from the ice-ocean interface. This is a result of turbulent kinetic energy being produced at the boundary. Spikes in ε are seen at 2 m when the current is approaching over the keel. We also see a spike at 8 m at YD 81.3 when the current is interacting strongly with the keel. It is suspected that there is an increase during this time and not at YD 79.3 when the current is also flowing over the keel due to the increased stratification at YD 81.3. We hypothesize that the larger ε, which increases by two orders of magnitude when the current is interacting with the keel, is due to 1) enhanced turbulence from keel interactions and 2) the confinement of turbulence production and dissipation in a relatively thin layer that is set by the underlying stratification.

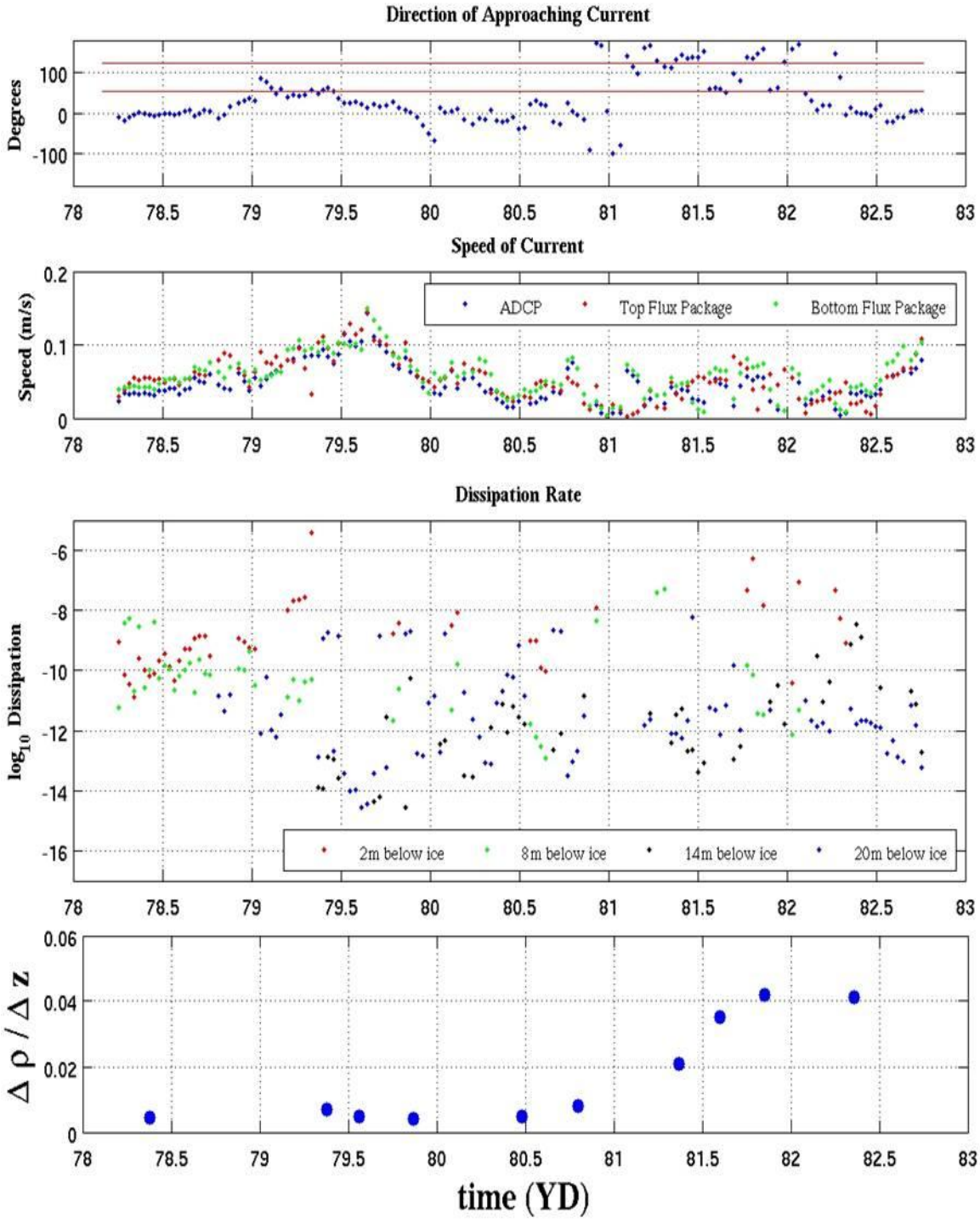

Figure 42. Time series of 40–60 minute time averaged (from top to bottom) current direction calculated from ADCP data, current speed, dissipation rate ε, and water column stratification expressed in $\Delta\rho/\Delta z$. Red lines on current direction plot indicate right and left edges of the keel.

3. Comparisons of Individual Spectra

a. Spectra of Data Taken in and Near Keel Wake at 2 and 8 m

Spectra from data recorded at 2 m (Figure 43) and 8 m (Figure 45), between YD 79.02–79.79, when the current approached the sensors from directly over the keel up to 30^{o} right of the keel, were compared and analyzed to study the changes in the turbulent structure.

In the 2 m case at YD 79.02 the current approached from 30^{o} right of the keel, at YD 79.23 10^{o} right, at YD 79.26 15^{o} right, at YD 79.30 right edge, at YD 79.33 over the keel, and at 79.79 20^{o} right of the keel. As seen in Figure 43, when the current was approaching from farthest to the right there was the least amount of vertical velocity energy recorded, while when the current was approaching from directly over the keel the vertical velocity variance increased by a factor of 10. Also of interest to note is the significant decrease in energy from 20^{o} to 30^{o} right of the keel. This suggests that even while the current is not flowing directly over the keel it is still significantly enhancing turbulence levels.

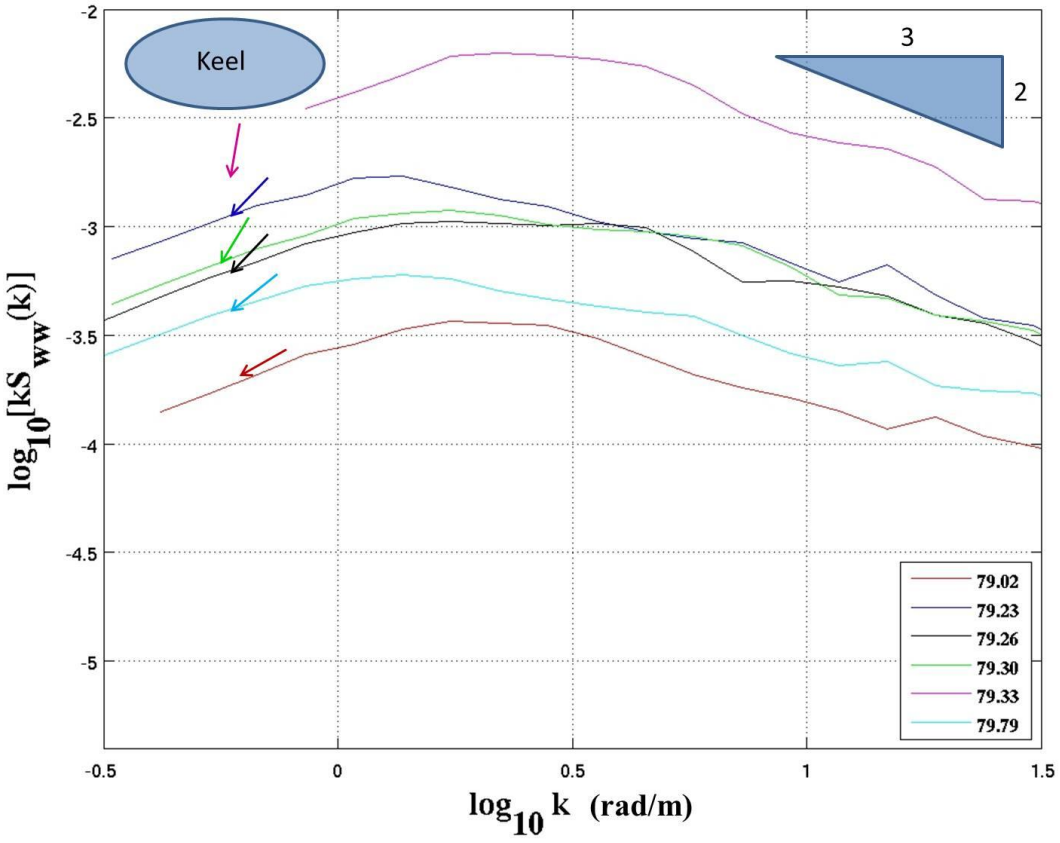

Figure 43. Plot of Sww(k) spectra collected at 2 m below the ice-ocean interface. Colored arrows indicate direction of current relative to keel and correspond to same colored spectrum.

It is also interesting that at YD 79.33, when the largest amount of vertical turbulent energy is observed, the speed of the current measured at 2 m was 0.031 m/s, a full 0.03 m/s slower than any other time observed in this comparison, and was 0.06 m/s slower than the current measured at 8 m during the same time. This suggests that the sensor was in the recirculation zone in the wake of the keel where the water is moving near the velocity of the ice, and decoupled from the deeper flow by weak stratification (Figure 38 profile YD 79.38). The time series of data for that time period is shown in Figure 44.

Vertical velocity time series (Figure 44) shows that the water trapped within the recirculation zone is slightly much more turbulent then the water below the recirculation zone.

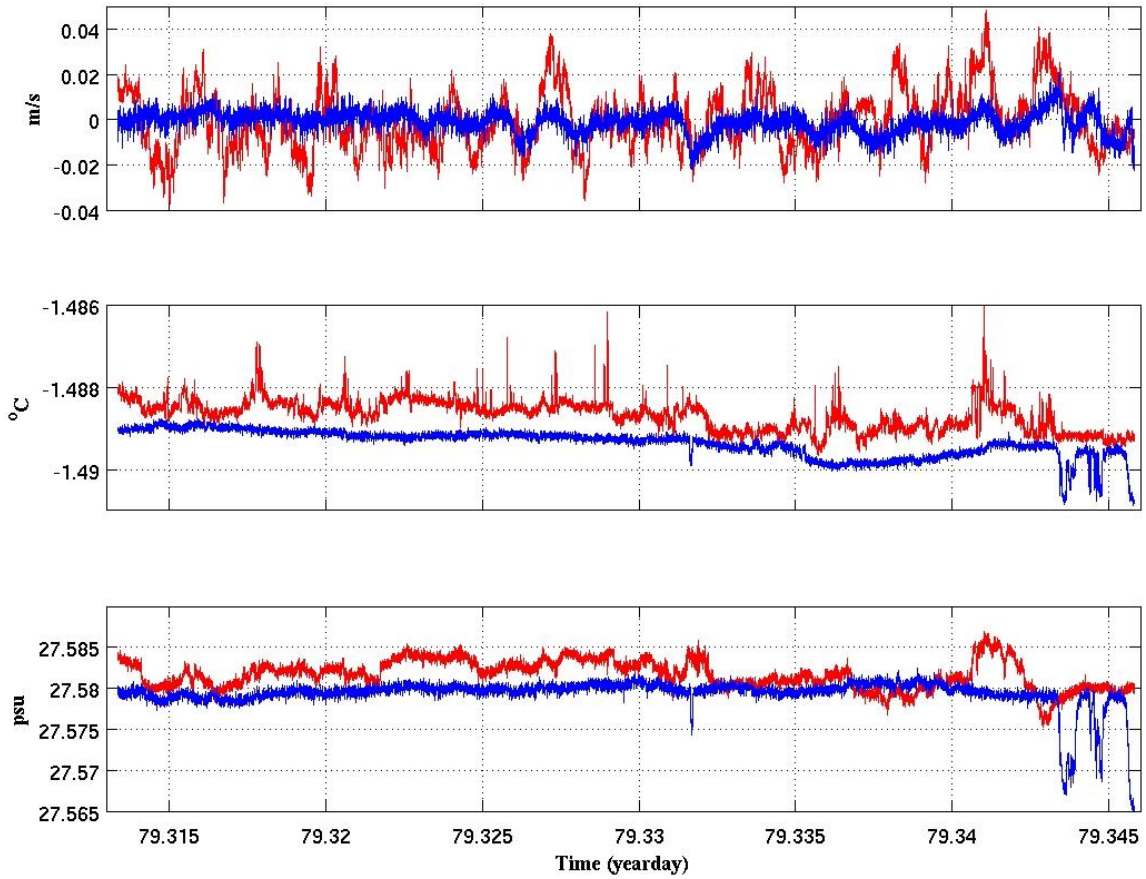

Figure 44. 46-minute time series of w', T, and S recorded at YD 79.33. Red time series was recorded at 1.7 m below the ice-ocean interface, blue time series recorded 7.2 m below the interface.

The vertical velocity spectra at 8 m below the ice for this same time period, (Figure 45), the current approached from the right edge at YD 79.02, 20^{o} right of the keel at YD 79.79, and all other times the current approached from directly over the keel. Just as in the 2 m case, when the current is approaching farthest from the keel is when there is the least amount of vertical velocity energy. It can be seen at lower

wavenumbers (k), turbulent energy increased by a factor of three when the current move from the right of the keel to directly over the keel.

Comparing the 2 m case (Figure 43) to the 8 m case (Figure 45) displays an increase in turbulent energy by a factor of five at 2 m when the current is to the right of the keel, however when the current is approaching directly over the keel there is an increase of a factor of 30 when going from 8 m to 2 m. This increase is due in large part to the stratification of the water column (Figure 38), where the stratification essentially traps the turbulence near the boundary at the surface.

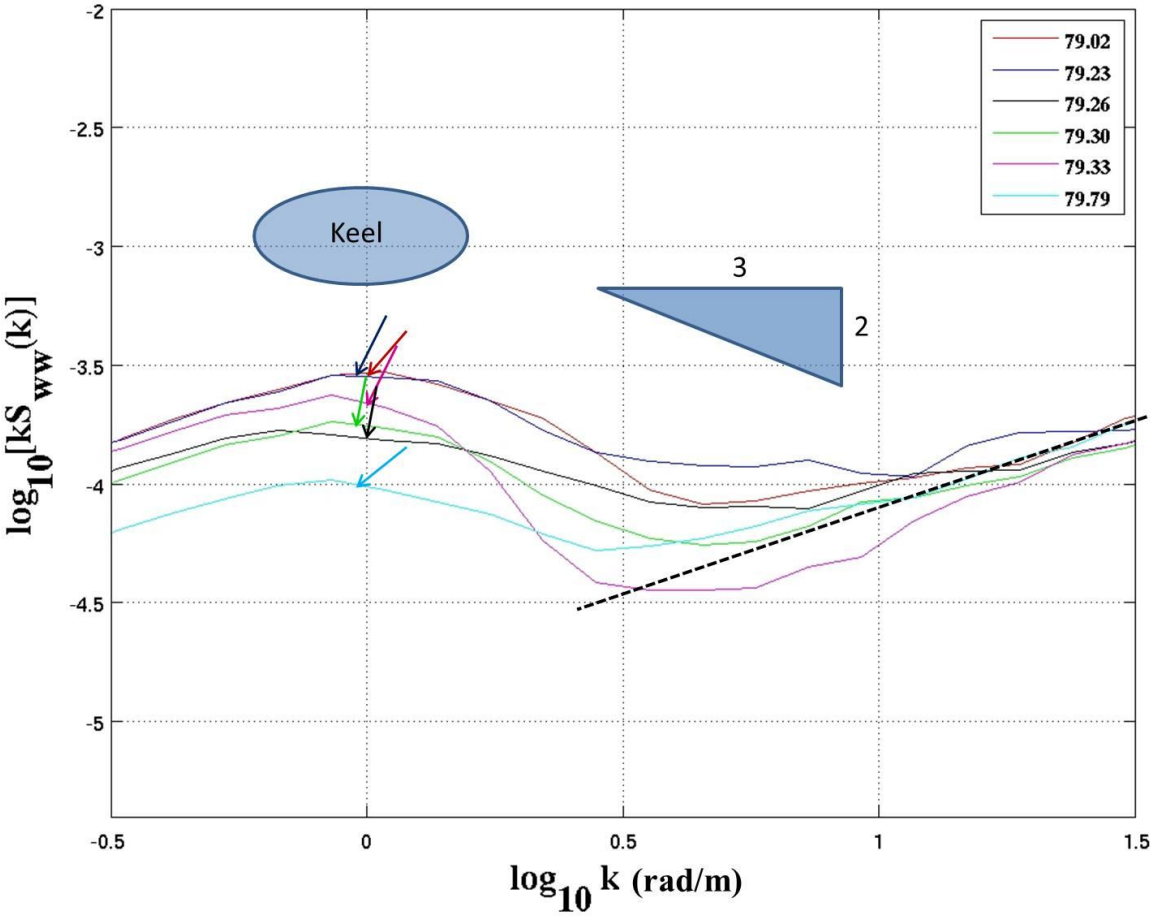

Figure 45. Plot of Sww(k) spectra collected at 8 m below the ice-ocean interface. Dashed black line indicates the noise floor of the instrument. Colored arrows indicate direction of current relative to keel and correspond to same colored spectrum.

b. Spectra of Data Taken in and Near Keel Wake at 14 and 20 m in a Weakly Stratified Mixed Layer

Spectra from data recorded at 14 m (Figure 46) and 20 m (Figure 47), between YD 79.37–79.72, when the current approached the sensors from directly over the keel up to 30^{o} right of the keel, with a mean speed that varied between 0.09–0.13 m/s were then compared.

Despite observing the maximum in current speed during this time there appears to be very little difference in turbulent energy at these depths, either when the current approached from the direction of the keel or to the right of it. This suggests that the stratification of the water column was strong enough to prevent turbulence generated at the ice-ocean boundary from penetrating that far into the water column.

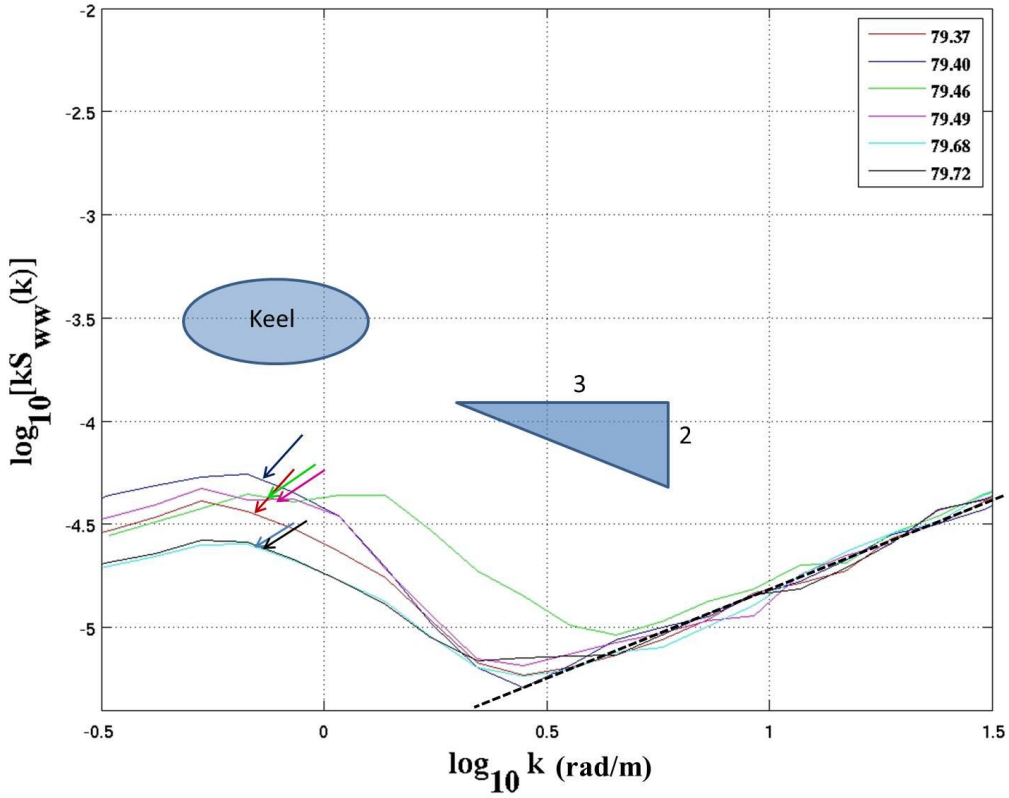

Figure 46. Plot of Sww(k) spectra collected at 14 m below the ice-ocean interface. Dashed black line indicates the noise floor of the instrument. Colored arrows indicate direction of current relative to keel and correspond to same colored spectrum.

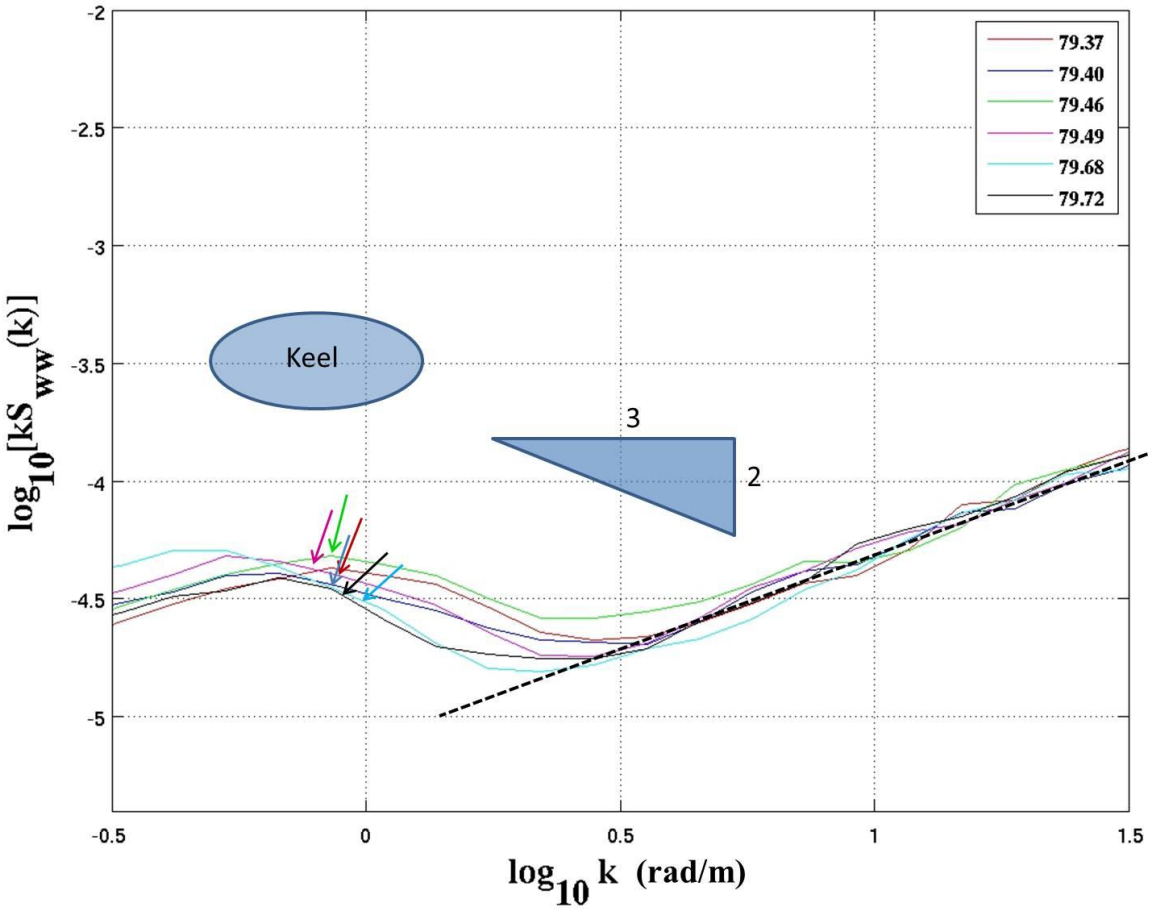

Figure 47. Plot of Sww(k) spectra collected at 20 m below the ice-ocean interface. Dashed black line indicates the noise floor of the instrument. Colored arrows indicate direction of current relative to keel and correspond to same colored spectrum.

The main difference observed in these spectra is in the k values greater than three, in which the energy spectra increase by a factor of five. It is at these k values where the noise floor, point at which noise generated by the sensing equipment is greater than the signal being measured, is displayed. Comparing these two plots (Figures 46 and 47) clearly indicates that the bottom mounted flux package generated more noise than the top mounted flux package. Updates to the flux packages firmware since this experiment has decreased the level of noise that they produce by a factor of 10 so future experiments will not experience this same level of noise.

c. Spectra of Data Taken in and Near Keel Wake at 14 and 20 m in an Intensely Stratified Mixed Layer

The third case that was analyzed was the spectra recorded at 14 m (Figure 48) and 20 m (Figure 49), between YD 82.11–82.24 when the current approached from directly over the keel, up to 50^{o} right of the keel, and the mean speed varied between 0.02–0.044 m/s. The spectrum from the data recorded at YD 82.11 at 14 m was not analyzed due to the current speed of 0.007 m/s at that time and depth. With the relative current moving that slowly Taylor's hypothesis is violated making that wavenumber spectrum invalid.

Unlike the previous case, displaying data recorded at the same depth, the third case shows increased energy levels at both 14 m and 20 m with the spectra at 14 m comparable to the energy levels seen in case one at 8 m (Figure 45). At 14 m there is also a noticeable increase in energy when the current is approaching from over the keel, YD 82.14, and when it is approaching 5^{o} to the right of the keel, YD 82.17. A smaller increase in energy is seen at 20 m when the current is approaching over the keel at YD 82.11.

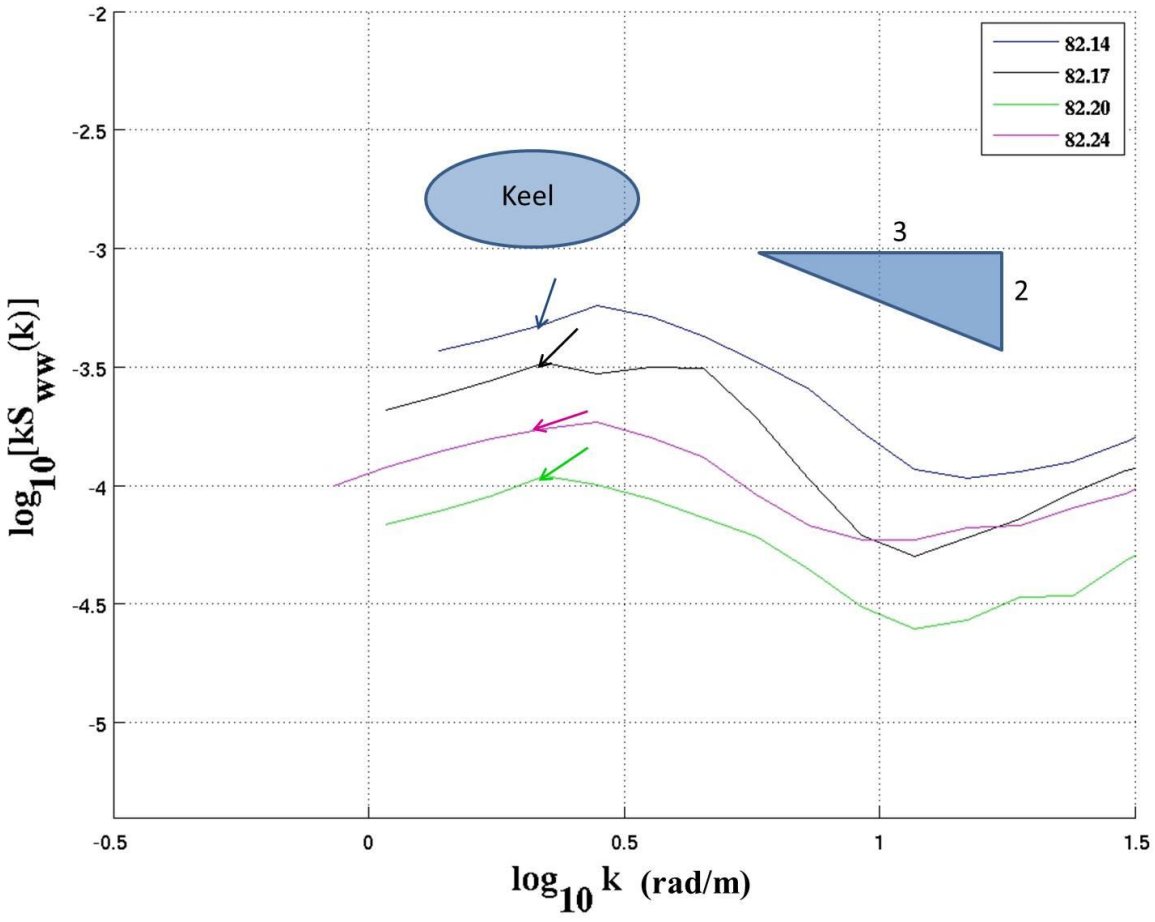

Figure 48 Plot of Sww(k) spectra collected at 14 m below the ice-ocean interface. Colored arrows indicate direction of current relative to keel and correspond to same colored spectrum.

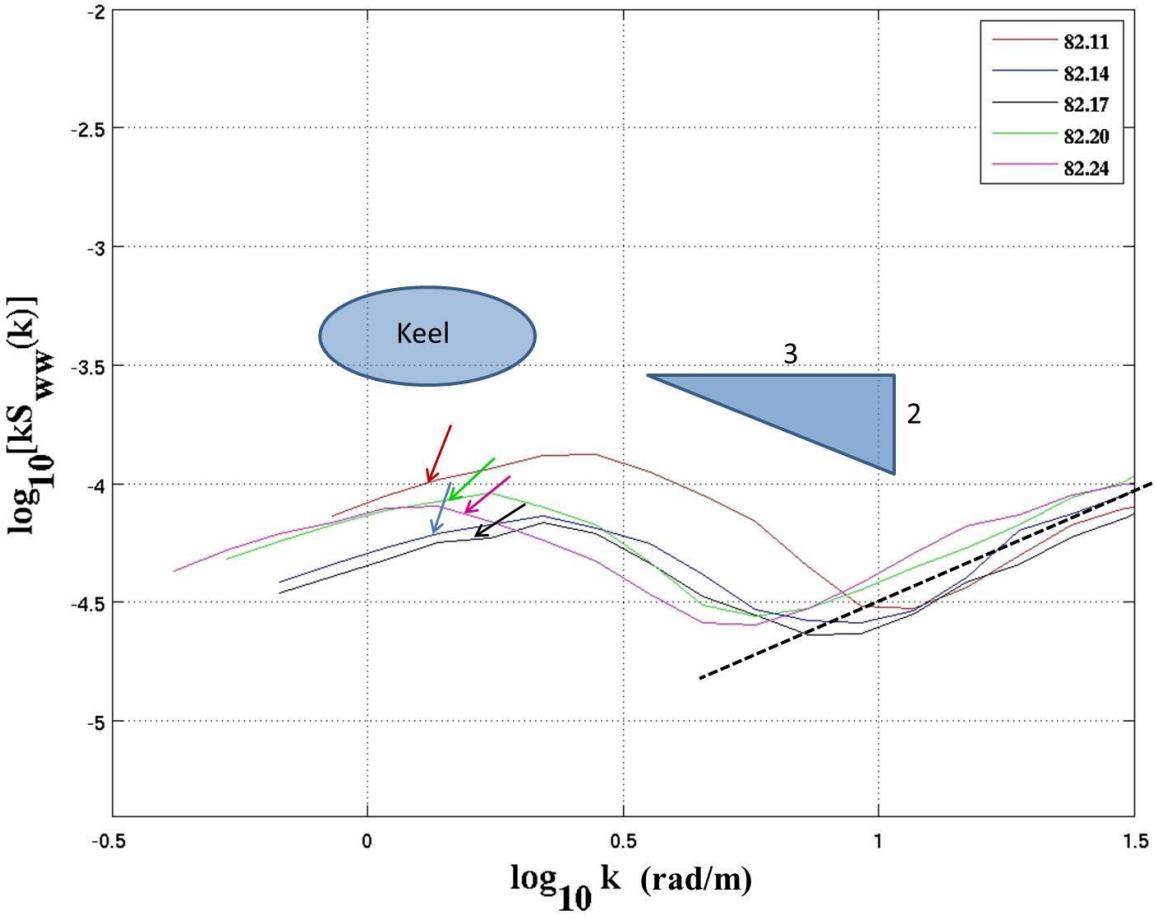

Figure 49. Plot of S(k) spectra collected at 20 m below the ice-ocean interface. Colored arrows indicate direction of current relative to keel and correspond to same colored spectrum.

The increased energy levels in the third case are a result of the stronger stratification (Figure 38) as compared to the stratification observed during the second case. The increased Δρ in case three results in a higher buoyancy frequency given in Equation 10, where g is the gravitational constant and ρ_r is the reference density.

$$N = \sqrt{\left(\frac{-g}{\rho_r}\right)\left(\frac{\partial \rho}{\partial z}\right)} \qquad (10)$$

The buoyancy frequency calculated at this time was 0.002 Hz, displayed as the vertical line in Figure 50. The higher buoyancy frequency allows for the formation of internal

waves at frequencies below N. By plotting the energy density spectra as a function of frequency (Figure 50) we can see that most of the energy is at frequencies below N, with the most energetic spectra occurring when the current is interacting with the keel, providing evidence that internal wave are being created by the keel as it moves through the water. The increase in energy at 20 m as compared to the 20 m spectra in case two suggests that the effects of these internal waves extends deep into the water column, which may contribute significantly to the increase heat fluxes (Figure 52) observed during that time, discussed below. The large spike at 0.01 Hz (Figure 50) is most likely the result of a vibration in the turbulence mast caused by the current "strumming" the mast that extended 25 m into the water column at this time.

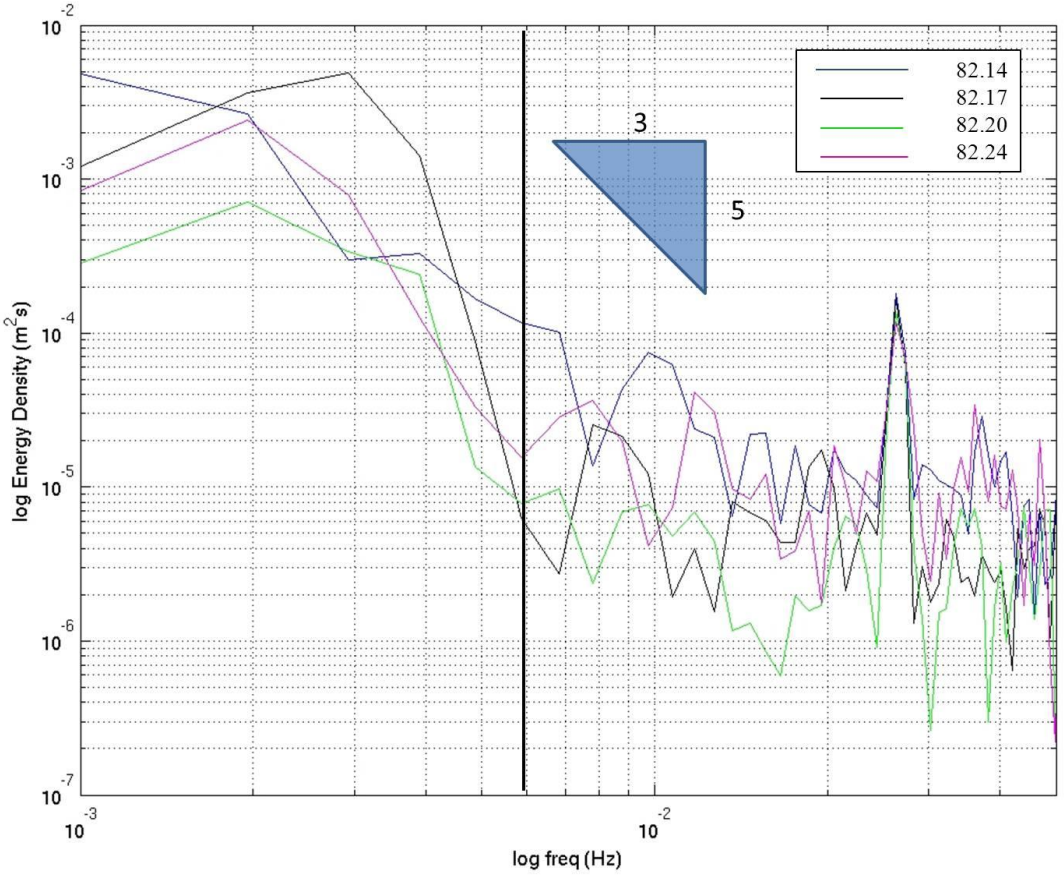

Figure 50. Energy density spectra as a function of frequency. Vertical black line indicates calculated buoyancy frequency. Same time series used in calculating Sww(k) spectra displayed in Figure 48.

D. DRAG COEFFICIENT (C_W)

Using our estimates for friction velocity u* and the magnitude of the ice velocity V relative to the ocean current 2 m below the ice-ocean interface, the under-ice quadratic drag coefficient C_w (Equation 11) can be calculated.

$$C_w = |u^*|^2 / |V|^2 \qquad (11)$$

Despite a wide range of ice undersurface roughness, most pack ice models and coupled ice/ocean models have assigned a constant value of 0.0055 to the magnitude of the complex drag coefficient C_w (McPhee 2002). The $|C_w|$ value of 0.0055 was obtained from the free-drift force balance at Arctic Ice Dynamics Joint Experiment (AIDJEX) stations (McPhee 1980). Using a constant drag coefficient does not allow numerical models account for variables in the ice/ocean boundary layer such as under-ice roughness and water column stratification. A plot of the drag coefficient (Figure 51) indicates that C_w varies greatly with changes to stratification and ice roughness.

From YD 78.2–80.8 when the water column is weakly stratified (Figure 38) C_w maintained a value of approximately 0.002 when the current was not affected by the keel, however increased by a factor of 10 to 0.02 when the current was flowing directly over the keel. After YD 80.8 when the water columns stratification increased significantly (Figure 38), C_w values increased to approximately 0.01 when the current was not affected by the keel but spiked at a value of 0.08 when the current interacted with the keel.

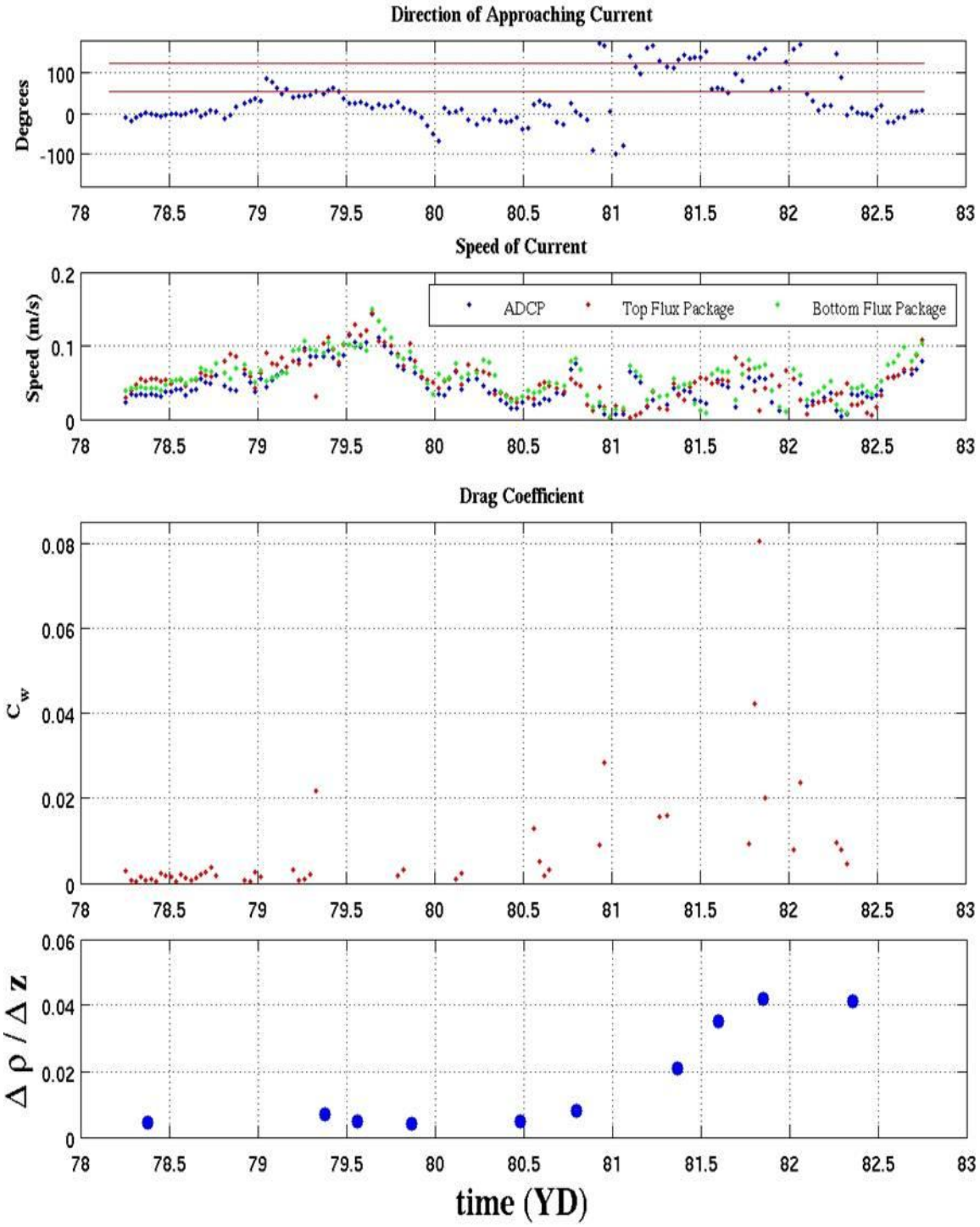

Figure 51. Time series of 40–60 minute time averaged (from top to bottom) current direction calculated from ADCP data, current speed, drag coefficient C_w calculated for data recorded at 2 m below ice-ocean interface, and water column stratification expressed in $\Delta\rho/\Delta z$. Red lines on current direction plot indicate right and left edges of the keel.

E. HEAT FLUX

Time series of 40–60 minute time averages of turbulent heat flux calculated by the eddy correlation method (Equation 1) are displayed on Figure 52. An increase in upward heat flux 2 m from the ice-ocean interface can be seen at YD 79.3 when the current approached from the right edge of the keel and is attributed to be a result of enhanced turbulence generated by the keel when the corresponding stress and dissipation increases are considered. Another slight increase at 20 m can be seen at YD 79.7 when the current is at its maximum. The large increases in heat flux seen at 8 m and 14 m during the last half of YD 81 are most likely caused by effects of the keel coupled with increased stratification. When the water column became increasingly stratified, warmer water trapped by the salinity-dominated stratification in the pycnocline is mixed upward leading to increased upward heat fluxes. The increased negative heat fluxes during the same time for the 2m below ice flux package are attributed to the positive temperature gradient near the surface (Figure 38). The large increase in positive and negative heat fluxes during the last half of YD 82.5 are consistent with increased stratification and positive surface temperature gradient discussed above interacting with the ice keel upstream of the sensors, along with the relatively rapid acceleration of the current that begins at YD 82.5 (Figure 39).

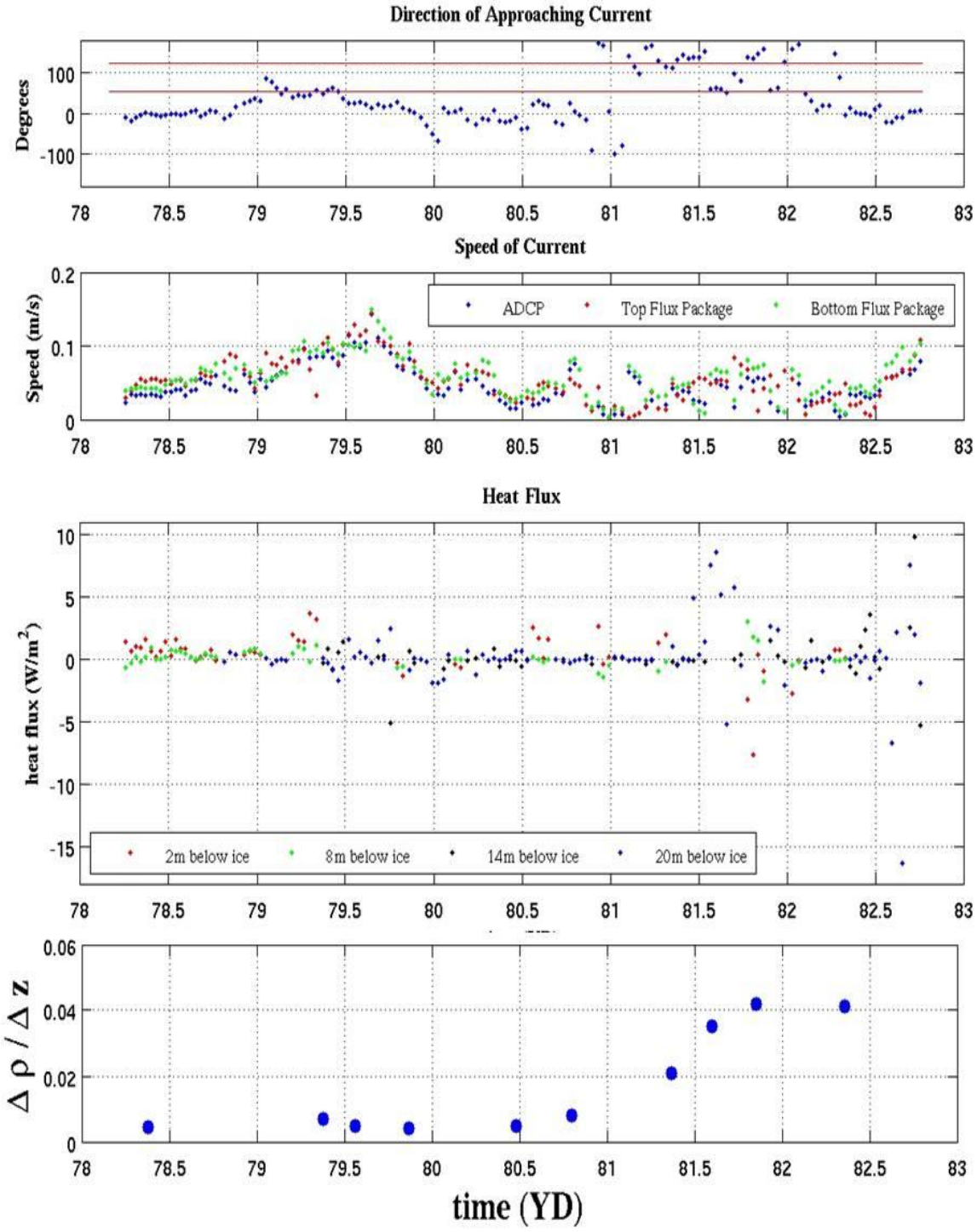

Figure 52. Time series of 40–60 minute time averaged (from top to bottom) current direction calculated from ADCP data, current speed, heat flux, and water column stratification expressed in $\Delta\rho/\Delta z$. Red lines on current direction plot indicate right and left edges of the keel.

Skyllingstad et al. (2003) simulation of data collected during SHEBA in an LES model found that the effects of a 10 m deep keel increased the heat flux from background values of 5 W m^{-2} to fluxes averaging 25 W m^{-2}. These much larger heat fluxes can be attributed to the 1.5 ^{o}C ΔT between 20–35 m depth in their model. The average ΔT between the same depths recorded during this experiment was 0.25 ^{o}C. Scaling down Skyllingstad's results by a factor of six, consistent with the difference in temperature gradients, the results from this experiment appear to agree reasonably well with Skyllingstad's ice keel / mixed layer simulation.

F. CONCLUSIONS

Even during benign weather conditions, in which there is little ice movement, ice keels generate significant turbulent mixing in the upper ocean. As stratification increased the generation of internal waves were observed as the ice keel dragged through the stratified part of the water column. This turbulence and mixing leads to entrainment of warmer water from the pycnocline up through the mixed layer and into contact with the ice, that could be a large contributor to ice melting.

Large variations in the ice-ocean drag coefficient C_w were produced from changes in under-ice roughness and water column stratification, with values as high as 0.08 in the stratified wake of 10 m deep ice keel, to values as low as 0.001 when the current was out of the wake of the keel and the water column was weakly stratified. Implementing variable $|C_w|$ values coupled with ice keel surveys such as the ones mentioned above (Bourke and McLaren 1992; Davis and Wadhams 1995) is a necessary step in order to improve modeling accuracy.

Enhanced turbulent and interval wave-induced mixing generated by ice keel movement and variations to the quadratic drag coefficient resulting from changes in water column structure and under-ice roughness should be studied further and parameterized for inclusion in coupled ice-ocean models in order to more precisely predict future Arctic conditions.

G. FURTHER STUDIES

In order to increase the understanding of the keel problem it would be useful to conduct the experiment again with a couple modifications. Utilizing a rotation motor for the 3-D BlueView sonar would further increase the resolution of the keel and would also shorten the time required to record data at each site. This would allow more sites to be scanned and a greater area around the keel could be mapped. A longer time series of data would be useful in order to increase the opportunity to observe a wider range of wind forcing and ice motion conditions. Occupying several sites around the keel with turbulence masts that contained sensors at fixed depths of 2, 8, 14, and 20 m would allow for a more consistent and robust time series. Study of the effects of different keel sizes is also necessary for a complete understanding of the keel problem.

It is also recommended that drag coefficients calculated for this analysis are implemented into an LES model to help better understand the implications of different C_w on ice floe movement. Attempts to scale the resulting C_w values obtained in this experiment through modeling a wide range of ice keel could then be made.

THIS PAGE INTENTIONALLY LEFT BLANK

LIST OF REFERENCES

Batchelor, G. K., 1967: *The theory of homogeneous turbulence*. Cambridge University Press, 197 pp.

BlueView Technologies, Inc., 2010: *BlueView BV5000 User Handbook*. BlueView Technologies Corp, 52 pp.

Bourke, R. H, and A. S. McLaren, 1992: Contour Mapping of Arctic Basin Ice Draft and Roughness Parameters. *J. Geophys. Res.*, **97**, C11, 17715–17728.

Coachman, L. K., 1969: Physical Oceanography in the Arctic Ocean, *Arctic*, **22**(3), 211–224.

Davis, N. R. and P. Wadhams, 1995: A statistical analysis of Arctic pressure ridge morphology, *J. Geophys. Res.*, **100**, C6, 10915–10925.

Ekman, V. W., 1905: On the influence of the earth's rotation on ocean currents. *Ark. Mat. Astr. Fys.*, **2**, 1–52.

McPhee, M. G., 1980: An analysis of pack ice drift in summer, *Proc. of the Arctic Ice Dynamics Joint Experiment International Commission on Snow and Ice Symposium*, Seattle, WA, 62–75.

McPhee, M. G., 1994: On the turbulent mixing length in the oceanic boundary layer, *J. Phys. Oceanogr.*, **24**, 2014–2031.

McPhee, M. G., 2002: Turbulent stress at the ice/ocean interface and bottom surface hydraulic roughness during SHEBA drift, *J. Geophys. Res.*, **107**, C10, 8037, doi:10.1029/2000JC000633.

McPhee, M. G., T. Kikuchi, J. H. Morison, and T. P. Stanton, 2003: Ocean-to-ice heat flux at the North Pole environmental observatory, *Geophys. Res. Lett.*, **30** (24), 2274, doi:10.1029/2003GL018580.

McPhee, M. G., 2004: A spectral Technique for Estimating Turbulent Stress, Scalar Flux Magnitude, and Eddy Viscosity in the Ocean Boundary Layer under Pack Ice, *J. Phys. Oceanogr.*, **34**, 2180–2188.

McPhee, M. G., 2008: *Air-Ice-Ocean Interaction: Turbulent Ocean Boundary Layer Exchange Process*. Springer, 215 pp.

Perovich, D. K., T. C. Grenfell, B. Light, and P. V. Hobbs, 2002: Seasonal evolution of the albedo of multiyear Arctic sea ice. *J.Geophys. Res.*, **107**, C10, 8044.

Pollard, R. T., and R. C. Millard, 1970: Comparison between observed and simulated wind-generated inertial oscillations. *Deep Sea Res.*, **17**, 813–821.

RD Instruments Acoustic Doppler Current Profilers, 1998: *Workhorse Technical Manual*, RD Instruments, 7–3 pp.

Shaw, W. J., T. P. Stanton, M. G. McPhee, J. H. Morison, and D. G. Martinson, 2009: Role of the upper ocean in the energy budget of Arctic sea ice during SHEBA, *J. Geophys. Res.*, **114**, C06012, doi:10.1029/2008JC004991.

Shimada, K., E. C. Carmack, K. Hatakeyama, and T. Takizawa, 2001: Varieties of shallow temperature maximum waters in the Western Canadian Basin of the Arctic Ocean, *Geophys. Res. Lett.*, **28** (18), 3441–3444.

Skyllingstad, E. D., C. A. Paulson, W. S. Pegau, M. G. McPhee, and T. P. Stanton, 2003: Effects of keels on ice bottom turbulence exchange. *J. Geophys. Res.*, **108**, C12, 3372, doi:10.1029/2002JC001488.

Steele, M., J. Morison, W. Ermold, I. Rigor, M. Ortmeyer, and K. Shimada, 2004: Circulation of summer Pacific halocline water in the Arctic Ocean, *J. Geophys. Res.*, **109**, C02027, doi:10.1029/2003JC002009.

Stroeve, J., M. M. Holland, W. Meier, T. Scambos, and M. Serreze, 2007: Arctic sea ice decline: Faster than forecast. *Geophys. Res. Lett.*, **34**, L09501, doi:10.1029/2007GL029703.

INITIAL DISTRIBUTION LIST

1. Defense Technical Information Center
   Ft. Belvoir, Virginia

2. Dudley Knox Library
   Naval Postgraduate School
   Monterey, California

3. Dr. Timothy Stanton
   Naval Postgraduate School
   Monterey, California

4. Dr. William Shaw
   Naval Postgraduate School
   Monterey, California

5. Lieutenant Brandon Schmidt
   Naval Undersea Warfare Center, Keyport Division
   Keyport, Washington